

# Testing the Quantum-Classical Boundary and Dimensionality of Quantum Systems



**Poh Hou Shun**

Centre for Quantum Technologies  
National University of Singapore

This dissertation is submitted for the degree of  
*Doctor of Philosophy*

September 2015



## Declaration

I hereby declare that this thesis is my original work and it has been written by me in its entirety. I have duly acknowledged all the sources of information which have been used in the thesis. This thesis has also not been submitted for any degree in any university previously.



Poh Hou Shun

June 2015



## Acknowledgements

No journey of scientific discovery is ever truly taken alone. Every step along the way, we encounter people who are a great source of encouragement, guidance, inspiration, joy, and support to us. The journey I have embarked upon during the course of this project is no exception.

I would like to extend my gratitude to my project partner on many occasion during the past 5 years, Ng Tien Tjeun. His humorous take on various matters ensures that there is never a dull moment in any late night lab work. A resounding shout-out to the ‘elite’ members of 0205 (our office), Tan Peng Kian, Shi Yicheng, and Victor Javier Huarcaya Azanon for their numerous discourses into everything under the sun, some which are possibly work related. Thank for tolerating my borderline hoarding behavior and the frequently malfunctioning door? I would like to thank Alessandro Ceré for his invaluable inputs on the many pesky problems that I had with data processing. Thanks for introducing me to world of Python programming. Now there is something better than Matlab? A big thanks also goes out to all of my other fellow researchers and colleagues both in the Quantum Optics group and in CQT. They are a source of great inspiration, support, and joy during my time in the group. Special thanks to my supervisor, Christian Kurtsiefer for his constant guidance on and off the project over the years.

I would like to thank my friends and family for their kind and constant words of encouragement and for tolerating my near complete incommunicado tenancies when I am in the zone.

Lastly and most importantly, I would like express my immeasurable thanks and gratitude to MM whose strength of character and sheer brilliance completely and singlehandedly changed my world view. You are most important person in my life.



## Abstract

Quantum theory introduces a cut between the observer and the observed system [1], but does not provide a definition of what is an observer [2]. Based on an informational definition of the observer, Grinbaum has recently [3] predicted an upper bound on bipartite correlations in the Clauser-Horne-Shimony-Holt (CHSH) Bell scenario equal to 2.82537, which is slightly smaller than the Tsirelson bound [4] of standard quantum theory, but is consistent with all the available experimental results [5–17]. Not being able to exceed Grinbaum’s limit would support that quantum theory is only an effective description of a more fundamental theory and would have a deep impact in physics and quantum information processing. In this thesis, we present a test of the CHSH inequality on photon pairs in maximally entangled states of polarization in which a value  $2.8276 \pm 0.00082$  is observed, violating Grinbaum’s bound by 2.72 standard deviations and providing the smallest distance with respect to Tsirelson’s bound ever reported, namely,  $0.0008 \pm 0.00082$ . This sets a new lower experimental bound for Tsirelson’s bound, strengthening the value of principles that predict Tsirelson’s bound [18–20] as possible explanations of all natural limits of correlations, and has important consequences for cryptographic security [21], randomness certification [22], characterization of physical properties in device-independent scenarios [23, 24] and certification of quantum computation [25].

The thesis also reports on our efforts in experimentally demonstrating that it is impossible to simulate quantum bipartite correlations with a deterministic universal Turing machine. Our approach is based on the *Normalized Information Distance* (NID) [26] that allows the comparison of two pieces of data without detailed knowledge about their origin. Using NID, we derived a completely new Bell type inequality for output of two local deterministic universal Turing machines with correlated inputs that is independent of any statistical considerations usually associated with other Bell’s inequalities. As a proof of concept, this inequality is violated by 6.5 standard deviations from its classical limits with a value of  $0.0494 \pm 0.0076$  by correlations generated by a maximally entangled polarization state of two photons. The violation is shown using a freely available lossless compression program. The presented technique may also complement the common statistical interpretation of quantum physics by an algorithmic one.

Similar to entanglement, the dimensionality of the Hilbert space describing a quantum system is an important quantum resource for various quantum information processing tasks. Previous attempts at experimentally witnessing large Hilbert space dimension have the limitation of not being able to distinguish between classical and quantum dimensions [27–29] or requiring a priori knowledge of the state under test to make a full assessment [30–33]. What is needed here is a way to device independently assess the minimal dimension of Hilbert space that is necessary to describe the system. Generalizing the work of Brunner [34], we report in this thesis an experimental implementation of a dimension witness based on the Collins-Gisin-Liden-Massar-Popescu (CGLMP) inequality [35] to test the dimensionality of an energy-time and polarization hyperentangled state. However, due to persistent stability issues in the generation of the hyperentangled state, we were not yet able to achieve a result with a small enough error bound to support a conclusion. Unfortunately, shortly before the conclusion of the writing of this thesis, it was also realized that the inequality can be violated with entangled states of a lower dimensionality purely by the classical feed-forward of an earlier measurement result onto the choice of settings for a later measurement, making our dimensions witness susceptible to the same limitations mentioned earlier. Whether this is a limitation of the specific form of the CGLMP inequality we were working with or indeed any other dimensional witnesses are subjects of ongoing work here.

# List of Publications

Some of the results of this thesis have been listed on arXiv preprint:

1. Hou Shun Poh, Siddarth K. Joshi, Alessandro Ceré, Adán Cabello, and Christian Kurtsiefer. **Approaching Tsirelson's bound in a photon pair experiment.** *arXiv preprint arXiv:quant-ph/1506.01865*
2. Hou Shun Poh, Marcin Markiewicz, Pawel Kurzynski, Alessandro Ceré, Dagomir Kaszlikowski, and Christian Kurtsiefer. **Probing quantum-classical boundary with compression software.** *arXiv preprint arXiv:quant-ph/1504.03126*

Some of the other results in this thesis have been presented in conferences and are reported in the following proceedings:

1. Hou Shun Poh, Marcin Markiewicz, Pawel Kurzynski, Alessandro Ceré, Dagomir Kaszlikowski, and Christian Kurtsiefer. **Probing quantum-classical boundary with compression software.** CLEO/Europe-EQEC 2015, Munich, Germany, 2015
2. Hou Shun Poh, Marcin Markiewicz, Pawel Kurzynski, Alessandro Ceré, Dagomir Kaszlikowski, and Christian Kurtsiefer. **Probing quantum-classical boundary with compression software.** *IPS Meeting 2015, Singapore, 2015*
3. Hou Shun Poh, Yu Cai, Valerio Scarani, and Christian Kurtsiefer. **Experimental Estimation of the Dimension Witness of Quantum Systems.** *IPS Meeting 2014, Singapore, 2014*

# Table of contents

<b>List of figures</b>	<b>xi</b>
<b>1 From Quantum Mechanics to Quantum Information and Computation</b>	<b>1</b>
1.1 Qubit, The Quantum Mechanical Bit . . . . .	3
1.1.1 Non-cloneability . . . . .	4
1.1.2 Superposition . . . . .	5
1.1.3 Entanglement . . . . .	6
1.2 Thesis Outline . . . . .	10
<b>2 Generation of Polarization-Entangled Photons and Their Characterization</b>	<b>13</b>
2.1 Second-order Non-linear Optical Phenomena . . . . .	16
2.2 Spontaneous Parametric Down-conversion (SPDC) . . . . .	17
2.3 Generation of Polarization-Entangled Photon Pairs . . . . .	18
2.3.1 Compensation of Longitudinal and Transverse Walk-Off . . . . .	20
2.4 Joint Detection Probability for Two-Photon Polarization-Entangled States .	23
2.5 Characterization of Polarization-Entangled Photon Pairs . . . . .	24
<b>3 Approaching Tsirelson’s Bound in a Photon Pair Experiment</b>	<b>29</b>
3.1 Implications of Approaching the Tsirelson’s Bound . . . . .	32
3.2 Prior Work . . . . .	33
3.3 Experimental Implementation . . . . .	35
3.4 Conclusions . . . . .	40
<b>4 Probing the Quantum-Classical Boundary with Compression Software</b>	<b>41</b>
4.1 Kolmogorov Complexity . . . . .	42
4.2 Simulation by Deterministic Universal Turing Machines . . . . .	42
4.2.1 Normalized Information Distance . . . . .	43
4.2.2 Information Inequality . . . . .	44
4.3 Estimation of Kolmogorov Complexity . . . . .	45

4.3.1	Statistical Approach . . . . .	45
4.3.2	Algorithmic approach . . . . .	47
4.4	Choice of Compressor . . . . .	48
4.5	Experiment Implementation . . . . .	51
4.6	Symmetrization of detector efficiencies . . . . .	53
4.7	Results . . . . .	54
4.8	Conclusion . . . . .	55
<b>5</b>	<b>Generation of Energy-Time Entangled Photons and Higher Dimensional States</b>	<b>57</b>
5.1	Generation of Energy-Time Entanglement . . . . .	59
5.2	Characterization of Energy-Time Entangled Photon Pairs . . . . .	63
5.3	Generation of Higher Dimensional States and Hyperentanglement . . . . .	65
<b>6</b>	<b>Experimental Estimation of the Dimension Witness Quantum Systems</b>	<b>69</b>
6.1	CGLMP Inequality . . . . .	70
6.1.1	Derivation of the 4-Dimensional CGLMP Inequality . . . . .	75
6.2	Implementation of 4-Dimensional Entangled Photons . . . . .	78
6.2.1	Setting the Electronic Delays . . . . .	81
6.2.2	Optimizing the Quality of the Interferometers . . . . .	81
6.2.3	Phase Setting and Stabilization of the Interferometers . . . . .	83
6.2.4	Stabilization of the Calibration and Pump Laser . . . . .	84
6.2.5	Characterization of the Hyperentangled State . . . . .	86
6.3	Measurement Settings . . . . .	86
6.4	Results and Conclusions . . . . .	92
<b>7</b>	<b>Conclusions</b>	<b>95</b>
	<b>References</b>	<b>99</b>

# List of figures

- 1.1 Stern-Gerlach experiment. A beam of neutral silver atom is collimated and directed through an inhomogeneous magnetic field. After passing through the inhomogeneous magnetic field, the beam splits into two. Since the silver atoms in the beam are neutral, any deflection of the silver beam can only be attributed to the intrinsic angular momentum of the unpaired electron in the silver atoms. Thus this experiment shows that the spin angular momentum of an electron along the direction defined by the magnetic field can only take one of two possible value,  $+\frac{\hbar}{2}$  (spin-up) or  $-\frac{\hbar}{2}$  (spin-down). . . . . 4
- 1.2 The Einstein-Podolsky-Rosen (EPR) thought experiment. A two-particle system is prepared in a state with a well-defined relative position  $x_1 - x_2$  and total momentum  $p_1 + p_2$  at time  $t = 0$ . The particles are then permitted to interact from time  $t = 0$  to  $t = T$ . After a certain amount of time  $t > T$  when the particles are sufficiently separated such that they are no longer interacting, the position particle 1 is measured. From the measurement result, it is possible to assign a definite value to the position of particle 2 without changing the state. The same case can be repeated for the measurement of momentum. This contradiction with the prediction quantum mechanics came to be known as the EPR paradox. . . . . 6
- 1.3 The Einstein-Podolsky-Rosen-Bohm (EPR-Bohm) thought experiment. An alternative version of the EPR experiment proposed by David Bohm in 1951 [36]. In the experiment, the decay of a neutral  $\pi$  meson acts as a source of electrons and positrons which are entangled in their spins. Spin measurement of either the electron or positron in any arbitrary direction  $\vec{a}$ ,  $\vec{b}$ , or  $\vec{c}$  will have an equal probability of yielding spin-up and spin-down. However, when comparing the results of the spin measurement of both particle measured in the same direction, they show perfect anti-correlation. . . . . 8

- 
- 1.4 The experimental setup used by Alain Aspect *et al.* in the early 1980s to violate the Bell's inequality. The polarization-entangled photons are generated via radiative atomic cascade of calcium. The photons then pass through the polarizers (Pol), consisting of glass plates stacked at Brewster angle, and are detected by photomultiplier tubes (PM). A combination of a time-to-amplitude converter (T.A.C.) and a coincidence circuit detects photons arriving within 19 ns of each other. With the setup, they observed a violation of the Bell's inequality by up to 9 standard deviations. (Figure adapted from [6]) . . . . . 9
- 2.1 The experimental setup used by Kocher *et al.* in 1967 to generate polarization-correlated photon pairs. Ultraviolet light from a H<sub>2</sub> arc lamp excited a beam of Ca atoms. Polarization-correlated photon pairs were generated when the excited Ca atoms decayed back to the ground state via an intermediate level (Fig. 2.2). These photon pairs then passed through linear polarizers followed by narrowband interference filters to be detected by photomultiplier tubes. (Figure adapted from [37].) . . . . . 14
- 2.2 The atomic cascade of Ca. Each Ca atom de-excites from the excited 4p<sup>2</sup> 1S<sub>0</sub> level via the 4p4s <sup>1</sup>P<sub>1</sub> level back to the ground state producing a 551.3 nm and 422.7 nm photon. The emitted photon pairs carry no net angular momentum as  $J = 0$  for both the initial and final states of the cascade. Coupled with the fact that both levels have the same even parity, the photons in each pair will exhibit polarization correlation. . . . . 14
- 2.3 The first photon pair source based on the process of SPDC was implemented by Burnham *et al.* in 1970. An ammonium dihydrogen phosphate (ADP) crystal is pumped by a 325 nm beam from a He-Cd laser. The ADP crystal is cut in such a way that the optical axis makes an angle of 52.4° with the normal of the faces to satisfy the condition of phase-matching. The down-converted photons then pass through a combination of spatial (iris) and spectral filtering (spike filter consisting of a monochromator) to be detected with the photomultiplier (PM) tubes. (Figure adapted from [38].) . . . . . 15

- 2.4 Type-II phase matched down-conversion. In type-II phase matching, an  $e$ -polarized pump photon gets down-converted into a pair of  $o$  and  $e$ -polarized photons of lower energy. The  $o$  and  $e$ -polarized photons are emitted from the down-conversion crystal in two respective cones which are non-concentric with either the pump beam or each other. In our setup, the down-conversion crystal is oriented in such a way that the extraordinary axis coincides with the vertical ( $V$ ) polarization, while the ordinary axis coincides with the horizontal ( $H$ ) polarization. These two cases are denoted as  $V_e$  and  $H_o$ , respectively. . . . . 19
- 2.5 Compensation of temporal walkoff. The photons first pass through a half wave plate ( $\lambda/2$ ) which rotates their polarization by  $90^\circ$ . This is followed by compensation crystals (CC) which are identical to the crystal used for down-conversion except with half the thickness. The optical axis (OA) of both CC are aligned in the same direction as that of the down-conversion crystal. In the first extreme case (a), the CC will halve the relative delay between the photons in the pair. In the second extreme case (b), the CC will induce a relative delay equal to that in the previous case between the photons in the pair. Thus, the photons pairs from these two cases are indistinguishable in the temporal degree of freedom, resulting in a pure polarization-entangled state. This is also true for all complementary creation sites in the crystal symmetric about the center of the crystal. For photon pairs created right in the center of the down-conversion crystal, the relative delay is just eliminated by the CC. . . . . 21
- 2.6 Compensation of transverse walkoff. At each of the intersection of the emission cones, there is an elongated spread of the  $o$ -polarized photons as compared to the  $e$ -polarized photons. After passing through the  $\lambda/2$ , the polarization of the photons are rotated by  $90^\circ$ . The CC, which are orientated such that their OA are parallel to that of the down-conversion crystal, then cause a shift in the path of the down-converted light such that the center for the distribution of the  $o$  and  $e$ -polarized photons coincide. This provide better overlap between the two distributions and thus results in a better spatial mode for collection into single mode optical fibers. . . . . 22
- 3.1 Selected experimental tests of the CHSH Bell inequality with results close to the Tsirelson (T) and Grinbaum (G) bounds in photonic systems (circles), atoms and ions (diamonds), Josephson junctions (square), and nitrogen-vacancy centers in diamond (triangle). Numbers represent the references. . . 34

3.2	Schematic of the experimental set-up. Polarization correlations of entangled-photon pairs are measured by film polarizers (POL) placed in front of the collection optics. All photons are detected by silicon avalanche photodetectors $D_A$ and $D_B$ , and registered in a coincidence unit (CU). . . . .	35
3.3	A series of values for the error $\Delta S$ are evaluated from a cumulative sum of the number detected events for the 312 measurements by propagating the error from Poissonian counting statistics. These errors are compared with those expected from a model of a maximally violation of $ \Psi^-\rangle$ state for the same total counts. From the figure, it can be seen that the experimentally obtained error is in close agreement with model, giving us good confidence that the state is stable throughout the measurement. . . . .	38
3.4	To ascertain the effect of wedge errors of the polarizers on the final value of $S$ obtained, we first normalized the singles counts at Alice and Bob individually to their sum at every settings to eliminate any effects on the singles due to power fluctuations in the pump beam. The singles for settings $a'_0, a'_1$ , and $b'_0, b'_1$ and their orthogonal settings respectively are plotted here against the number of measurement. The jumps in the plots are due to minute difference in the pump wavelength each time the laser goes out of lock with the wavemeter and is relocked. These are ascertain to have negligible impact on the spread of $\Delta S$ . From the mean of the 8 traces we are able to calculate correction factor for each of settings. After applying the correction, we get a value of $S = 2.8281 \pm 0.0031$ . . . . .	39
4.1	Measurement: $N$ particles enter a measuring device, characterized by two possible polarizer settings $a_0$ and $a_1$ , which generates a bit string of $N$ measurement outcomes. Simulation: a universal Turing machine is fed with a program elements $\Lambda_i$ and information about the chosen setting $a_0$ or $a_1$ . It delivers an output string of length $N$ . . . . .	43
4.2	Local classical machines simulating the generation of strings $x$ and $y$ by correlation measurements on an entangled state. . . . .	44
4.3	Comparison of the compression overhead $Q$ obtained using four different compression algorithms on pseudo-random strings of varying lengths. The expected value for an ideal compressor is 0. From this characterization we can exclude <i>lzw</i> as a useful compressor for our application. . . . .	49
4.4	Compression overhead $Q$ for the string $xy$ as a function of the probability of pairwise correlation $p$ between the bits of the generating strings $x$ and $y$ for three different compressors: <i>bzip</i> , <i>gzip</i> , and <i>lzma</i> . . . . .	50

- 4.5 Schematic of the experimental set-up. Polarization correlations of entangled-photon pairs are measured by the polarization analyzers  $M_A$  and  $M_B$ , each consisting of a half wave plate ( $\lambda/2$ ) followed by a polarization beam splitter (PBS). All photons are detected by Avalanche photodetectors  $D_H$  and  $D_V$ , and registered in a coincidence unit (CU). . . . . 51
- 4.6 Plots of  $S$  versus angle of separation  $\theta$ . (a) Result obtained from Eq. (4.7) (b) result obtained from using the LZMA compressor on a simulated data ensemble, (c) measurement of  $S$  in the experiment shown in Fig. 4.5, and (d) longer measurement at the optimal angle  $\theta = 8.6^\circ$ . . . . . 54
- 5.1 Schematic of experiment proposed by Franson in 1989. Wavelength-correlated photons,  $\gamma_1$  and  $\gamma_2$ , generated by spontaneous decay from the excited state of a three-level atomic system passes through an unbalanced Mach-Zehnder interferometers on each path. Photon coincidence measurements of the interference between the amplitudes along the shorter paths,  $S_1$  and  $S_2$ , and the longer paths,  $L_1$  and  $L_2$  for various phase setting of  $\phi_1$  and  $\phi_2$  were taken (Figure adapted from [39]). . . . . 59
- 5.2 a) Experimental setup for the preparation of energy-time entangled photon pairs. A pump photon with coherence time  $\tau_p$  is down-converted into correlated photon pairs with coherence time  $\tau_{dc}$ . The photon pairs are sent into Mach-Zehnder interferometers which introduces a time delay  $\Delta T$  due to the unbalanced arm lengths (short path  $|s\rangle$  and long path  $|l\rangle$ ). The condition  $\Delta T < \tau_2$  guarantees the coherent superposition of the photon pairs which take the short path  $|s\rangle$  or long path  $|l\rangle$  in the interferometers. The Franson interference [39] or second order correlation between the photon pairs are measured by silicon avalanche photodiodes (APD), with a time delay  $t_A - t_B$  between  $D_A$  and  $D_B$ . b) For the generation of time-bin entanglement, the pump is operated in a pulsed regime, with an inclusion of an unbalanced Mach-Zehnder interferometer in in the path of the pump. . . . . 61
- 5.3 Four possible amplitudes of the photon pairs in the time delay basis. The two coherent states  $|s\rangle_A|s\rangle_B$  and  $|l\rangle_A|l\rangle_B$  overlap up to the coherence length of the down-converted photon pairs and there is no single photon interference under the condition where the coherence length of the down-converted photons are less than that introduced by the unbalanced Mach-Zehnder interferometer,  $l_{C_{dc}} < \Delta L$ . . . . . 62

- 
- 5.4 Energy-time bipartite states with a dimensionality,  $d > 2$ , can be implemented by cascading two or more interferometers in each arm of both  $A$  and  $B$  [40–42]. The difference between the long path of each of the interferometers must be greater than the coherence length of the down-converted photons to avoid single photon interference and  $\Delta T$  must be greater than coincidence window  $\tau_C$  such that the various energy-time combinations are distinguishable. Given the constraint, the natural choice of the length of the long paths for a cascade of  $n$  interferometer is  $\Delta L, 2\Delta L, 3\Delta L, \dots$ , and  $n\Delta L$ . . . . . 66
- 6.1 A  $d$ -dimensional quantum system with two measurement settings  $A_1$  and  $A_2$  or  $B_1$  and  $B_2$ , and  $d$  outcomes on each side. The four different combinations of settings give in total of  $4d^2$  possible outcome of coincidence patterns which can be used for calculating the CGLMP inequality. . . . . 71
- 6.2 Implementation and analysis of the polarization and energy-time hyperentangled state with a dimensionality of  $d = 4$ . a) Entangled photon pairs are generated by a typical spontaneous parametric down-conversion (SPDC) setup in a crossed-ring configuration. b) The polarization degree of freedom of the down-converted photons is first analyzed on an optical bench consisting of a quarter-wave ( $\lambda/4$ ), half-wave plate ( $\lambda/2$ ), and a polarization beam splitter (PBS). This is followed by an unbalanced Michelson interferometer where the energy-time degree of freedom is analyzed. The photons are detected by silicon avalanche photodetectors (APD) and the signals registered on a coincidence unit (CU). . . . . 79
- 6.3 In order to zero the delay between the two output signals of the APDs at the CU, an electronic delay stage is fitted to each of the two signal lines leading to the CU. To ascertain the correct delay settings, we monitor the coincidence counts between the two APDs and while keeping  $A$ 's delay fixed, we scan the electronic delay on the signal from  $B$ 's detector over a range of a few ns. . . . . 82
- 6.4 By cascading the two interferometers one after the other and scanning the MM of the  $B$  interferometer, interference between the  $|s\rangle_A|l\rangle_B$  and  $|l\rangle_A|s\rangle_B$  path can observed using broadband light from an infrared LED. The position of the center of the interference envelope corresponds to the case of a zero path-length difference between the  $|s\rangle_A|l\rangle_B$  and  $|l\rangle_A|s\rangle_B$ , indicating that the individual path-length difference of each interferometer,  $\Delta L$  are identical. . . . . 83

- 
- 6.5 In order to characterize the accuracy at which we can set the phases in the interferometers, multiple cycles of the counts versus the phase setting  $\phi$  ranging from 0 to  $2\pi$  were measured. Fits to a sinusoidally varying function were performed to determine their minimum positions which is expected at  $\phi = \pi$ . The fitted minimum positions show a spread of the expected minimum position  $\pi$  by  $\pm 0.1$  rad, giving us the uncertainty of the phase setting with this procedure. . . . . 85
- 6.6 Polarization correlations (upper) in the H/V and  $+45^\circ/-45^\circ$  bases. We observed direct visibilities of  $V_{HV} = 100 \pm 1\%$  and  $V_{45} = 99.1 \pm 0.9\%$ . The energy-time visibility (lower) for coincidences between the signals at output of both interferometers is  $V = 100 \pm 9\%$ . The large error bound for  $V$  can be attributed to the low signal counts collected within the short integration time. . . . . 87



# Chapter 1

## From Quantum Mechanics to Quantum Information and Computation

The three-age system often referred to in archaeology and anthropology compartmentalizes early human history, based on the prevailing tool-making technologies of the era, into three consecutive time periods: the Stone Age, Bronze Age, and Iron Age. The transitions between these epochs corresponded to times of great advancements in every facade of human society.

As we stepped barely two decades into the 21st century, we have already found ourselves in the midst of the fourth age, the Information Age (Digital Age). Evidences of this are clearly visible: almost all of our daily activities, ranging from the way we communicate and interact to the way knowledge is being taught in schools, rely on information. Suffice to say digital information as intangible as it may be has an even greater impact on our lives than any tangible tools that followed previously.

This technological turn of events was of course spawned by the first quantum revolution which brought us the transistor. The first solid state transistor, invented at Bell Laboratories on December 16, 1947 by William Shockley, John Bardeen, and Walter Brattain, started life as a study into the flow of electrons over the surface of a semiconductor. The smaller and more energy efficient transistor ultimately replaced the vacuum tube. Since then, increasing level of miniaturization enabled more transistors to fit onto a single silicon chip, resulting in more powerful and energy efficient processors for computers.

Paralleling these technological advancements were the significant progresses made in the field of experimental physics over the past few decades. We are becoming increasingly proficient in the fabrication and manipulation of physical systems which demonstrate quantum effects. With this next quantum revolution, experiments have started to exploit the various degrees of freedom available in a number of quantum systems to encode bits of

quantum information or qubits. Some of these first experiments [6, 38] used the polarization degree of a photon to encode the qubit. These photonic qubits have the advantage of being easy to generate and are relatively resistant to decoherence. Thus they remain very much relevant and widely used in experiments [7, 43–46] till today.

These qubits exhibit features of non-cloneability, superposition, and can be entangled in multi-qubit states, all of which are purely quantum mechanical effects. When photonic qubits are entangled in a multi-qubit state, they can be used for various quantum communication protocols [47, 48] and fundamental tests of quantum physics in higher-dimensional Hilbert spaces [35, 49, 50]. Multi-qubit states also allow certain classes of computational tasks [51, 52] which are either inefficient or impractical on classical information processing systems to be carried out.

Just barely a few decades into the Information Age, are we seeing the first telltale signs that we are on the verge of the Quantum Information Age? Quantum key distribution (QKD) systems, initially the exclusive domain of research laboratories of universities are making their first commercial appearances<sup>1</sup>. Large organizations like Google, Lockheed Martin, and NASA are using D-Wave computers which are touted as the world’s first commercial quantum computers<sup>2</sup>.

However, despite the technological advances and progresses in our understanding of how to manipulate and experiment on these quantum systems, there are still significant gaps in our understanding of the fundamental issues surrounding quantum mechanics. Questions regarding whether quantum theory is a fundamental theory or an effective version of a more general theory and whether the currently predominant statistical interpretation of quantum mechanics is the only one available to us remain unanswered.

On the application side of quantum mechanics, there is also a lack of comprehensive ways to certify cryptographic security [21], randomness [22], and quantum computation [25]. Methods to characterize physical properties in these quantum system in device-independent scenarios [23, 24] are also needed: e.g. methods to device independently assess the dimensionality of quantum information processing systems which determines the capacity of these system to perform quantum information processing [33, 53].

The above mentioned issues serve as the main motivations for the work presented in this thesis. In this thesis, we report our attempt at setting up a source of high quality polarization-entangled photon pairs and their use in violating the CHSH inequality both maximally

---

<sup>1</sup>Currently there are four companies, idQuantique, MagiQ Technologies, QuintessenceLabs, and SeQureNet offering commercial QKD devices.

<sup>2</sup>Due to the secrecy surrounding the structures and performances of these D-Waves computers, the scientific community at large have yet to reach a consensus on whether these D-Wave computers, while unitizing certain quantum phenomena in their operations, qualify as quantum computers.

and with the smallest error bar currently recorded in literature to closely approaching the Tsirelson's bound<sup>3</sup>, This thesis also reports our work in deriving a completely new Bell type inequality based solely on the concept of Kolmogorov complexity and normalized information distance (NID) [26], independent of any statistical considerations usually associated with other Bell's inequalities. We also document in detail our procedures in coming up with an estimate to the Kolmogorov complexity by appealing to the concept of compressibility, obtainable in actual implementation using freely available compression softwares. This inequality was then violated in experiment as a proof of concept. Lastly we report the setting up of a energy-time and polarization hyperentangled source and its use in the experimental implementation of a dimension witness based on the Collins-Gisin-Liden-Massar-Popescu (CGLMP) inequality, a family of Bell's inequalities for bipartite quantum systems of arbitrarily high dimensionality.

## 1.1 Qubit, The Quantum Mechanical Bit

The bit is the most fundamental unit of classical information. It is a representation of a binary digit, taking a logical value of either "1" or "0". Due to the binary nature of the classical bit, digital information can be encoded in any physical system which has two stable states such as the direction of a magnetic domain on magnetic media, the pits and bumps on the reflective layer on an optical disk, or voltage levels in a digital circuit.

Over the past few decades, we have seen experiments that allow us to study and manipulate physical systems which exhibit quantum behaviors being devised and implemented. In this quantum regime, the quantum bit of information or qubit can be encoded in state of a spin- $\frac{1}{2}$  (two-level) system. The reason why a spin- $\frac{1}{2}$  system is also called a two-level system stemmed from an experiment performed by Otto Stern and Walther Gerlach in 1922 [54, 55] to study the intrinsic angular momentum of an electron. In what later came to be known as the Stern-Gerlach experiment (Fig. 1.1), they showed that the spin angular momentum of an electron along any direction can only take one of two possible value,  $+\frac{\hbar}{2}$  (spin-up) or  $-\frac{\hbar}{2}$  (spin-down). In the quantum state vector representation, spin-up and spin down can be written as  $|\uparrow\rangle$  and  $|\downarrow\rangle$ , respectively. It is possible to manipulate the direction of the electron spins and by associating "1" to  $|\uparrow\rangle$  and "0" to  $|\downarrow\rangle$ , this degree of freedom can be used essentially to encode qubits.

---

<sup>3</sup>The Tsirelson's bound is a fundamental limit predicted by quantum mechanics for the amount of correlation that can exist between quantum systems. Saturation of this limit in experiment would imply that no modification of the standard quantum theory is required.

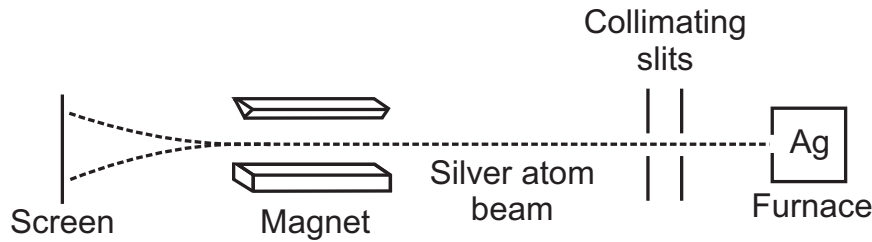


Fig. 1.1 Stern-Gerlach experiment. A beam of neutral silver atom is collimated and directed through an inhomogeneous magnetic field. After passing through the inhomogeneous magnetic field, the beam splits into two. Since the silver atoms in the beam are neutral, any deflection of the silver beam can only be attributed to the intrinsic angular momentum of the unpaired electron in the silver atoms. Thus this experiment shows that the spin angular momentum of an electron along the direction defined by the magnetic field can only take one of two possible values,  $+\frac{\hbar}{2}$  (spin-up) or  $-\frac{\hbar}{2}$  (spin-down).

Apart from the spin of an electron, various degrees of freedom of other quantum systems can also be used to encode the qubit. A few examples are the magnetic flux, charge or phase of superconducting circuits [56] and the energy levels [57] or nuclear spins [58] in atoms. By far the most commonly used physical carrier of the qubit in experiments is the photon. The photon has a number of degrees of freedom that can be used to encode a qubit: photon number (the number of photons in a specific mode) [59], energy-time (arrival times of photons in an interferometric-type setup [60, 61]), or the polarization [7, 62, 63]. Out of the three, the polarization of a photon is most often used to encode a qubit as it is easy to generate, manipulate, and relatively resistant to decoherence. These qubits exhibit the features of non-cloneability, superposition, and can be entangled in multi-qubit states. All these characteristics are purely quantum mechanical in nature and they form the backbone for quantum information and quantum computation.

### 1.1.1 Non-cloneability

It is trivial to copy a file on the computer. The copy of the file is essentially a perfect clone of the original. However, in quantum mechanics this is not generally true. This phenomenon is outlined in the non-cloning theorem [64, 65]. The theorem forbids the creation of identical copies of an arbitrary unknown quantum state. If a quantum cloning device is able to clone a state  $|\psi\rangle$  with perfect fidelity, it is at most only able to do so for the orthogonal state  $|\psi\rangle^\perp$ . For the special case of a spin- $\frac{1}{2}$  system, even under optimal conditions, the maximum fidelity of cloning of an arbitrary unknown quantum state is shown only to be 0.83 (ranging from 0

to 1 denoting increasing levels of fidelity from the case of being completely non-identical to being identical in state) [66].

The no-cloning theorem has significant implications especially for the field of quantum key distribution (QKD). It prevents an eavesdropper from making perfect multiple copies of the qubits being distributed in the quantum channel, which in principle could be used, in conjunction with other resources, to gain full knowledge of the distributed key.

### 1.1.2 Superposition

A classical bit of information can take the logical value of either "0" or "1", but not both simultaneously. However, in the quantum regime, it is possible to prepare a quantum system such that it is in a state  $c_0|0\rangle + c_1|1\rangle$ , where  $c_0$  and  $c_1$  are the probability amplitudes and are in general both complex numbers. When we measure this qubit in the  $|0\rangle$  and  $|1\rangle$  basis state, the probability of the outcome is  $|c_0|^2$  and  $|c_1|^2$ , respectively. As the absolute squares of the amplitudes equate to probabilities, it follows that  $c_0$  and  $c_1$  must be constrained by the equation  $|c_0|^2 + |c_1|^2 = 1$ , which implies that one will measure either one of the states. Such a two-level quantum system is said to be in a linear superposition of the  $|0\rangle$  and  $|1\rangle$  basis state and does not exist definitely in either states.

The advantage of a superposition of states really comes in when we start dealing with system containing several qubits. Such a collection of  $N$  qubits is called a quantum register of size  $N$  and can hold  $2^N$  numbers. This is in contrast with a classical register of the same size which can only hold a single number. For example in the case of a two-qubit system register, a state consisting of a superposition of the four combination is possible. The state of such a two-qubit system can be written as:

$$|\Psi\rangle = c_{00}|0\rangle_A|0\rangle_B + c_{01}|0\rangle_A|1\rangle_B + c_{10}|1\rangle_A|0\rangle_B + c_{11}|1\rangle_A|1\rangle_B, \quad (1.1)$$

where  $c_{ij}$  is the probability amplitude of  $|i\rangle_A|j\rangle_B$  and the notation  $|i\rangle_A|j\rangle_B$  means that qubit in mode 1 and 2 are in state  $A$  and  $B$ , respectively.

Quantum algorithms make full use of this fact by being able to accept all the possible inputs pertaining to a certain computation task as a linear superposition of basis states like in Eq. 1.1 and evaluate them in parallel. The required output from the evaluation is then obtained by suitable measurements performed on the resulting state. It is this parallelism that gives quantum systems the edge over their classical counterparts in certain computational tasks<sup>4</sup>.

<sup>4</sup>A brief discussion on the classes of computation problems which benefit from quantum parallelism is available in [67].

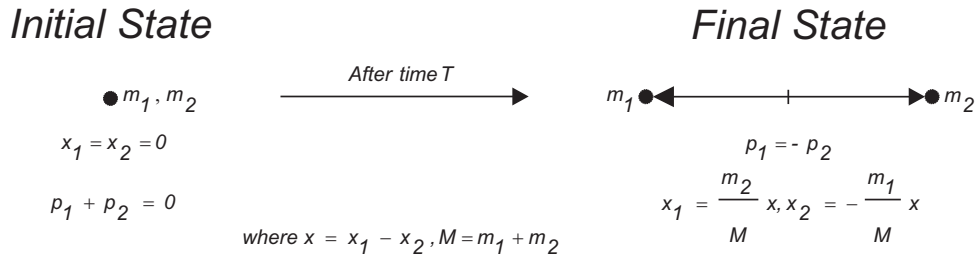


Fig. 1.2 The Einstein-Podolsky-Rosen (EPR) thought experiment. A two-particle system is prepared in a state with a well-defined relative position  $x_1 - x_2$  and total momentum  $p_1 + p_2$  at time  $t = 0$ . The particles are then permitted to interact from time  $t = 0$  to  $t = T$ . After a certain amount of time  $t > T$  when the particles are sufficiently separated such that they are no longer interacting, the position of particle 1 is measured. From the measurement result, it is possible to assign a definite value to the position of particle 2 without changing the state. The same case can be repeated for the measurement of momentum. This contradiction with the prediction of quantum mechanics came to be known as the EPR paradox.

### 1.1.3 Entanglement

Quantum entanglement is a peculiar feature that is observed in some composite quantum systems. Essentially, the quantum mechanical state of certain systems consisting of two or more entities can no longer be adequately described by considering each of the component entities in isolation. A full description of such a composite quantum system is only possible by considering the system as a whole. This results in a kind of connection between the components that is quantum mechanical in nature and cannot be explained by classical correlations alone. These non-classical connections between entangled qubits are the essential requirements for various quantum computation and communication protocols.

The very idea of quantum entanglement originated from a paper published by Albert Einstein, Boris Podolsky, and Nathan Rosen in 1935 [68] regarding their discussion on the completeness of the quantum mechanical description of reality. In their discussion, they considered a two-particle system (Fig. 1.2) prepared in a state with a well-defined relative position  $x_1 - x_2$  and total momentum  $p_1 + p_2$  at time  $t = 0$ . The particles are then permitted to interact from time  $t = 0$  to  $t = T$ . After a certain amount of time  $t > T$  when the particles are sufficiently separated such that they are no longer interacting, the position of particle 1 is measured. From the measurement result, it is possible to assign a definite value to the position of particle 2. The same case can be repeated for the measurement of momentum.

As the measurement of position or momentum of particle 1 will yield definite values for both particles, these quantities are, according to their definition, elements of reality. Since the two particles no longer interact with each other, the state of particle 2 is left unchanged

by the measurement performed on particle 1. This is contrary to the prediction of quantum mechanics where the two operators of position and momentum do not commute. Measurement of the position of a particle will inadvertently change the state of the particle in such a way that it destroys all knowledge of the momentum and vice versa. This contradiction, which came to be known as the Einstein-Podolsky-Rosen (EPR) paradox, forced them to conclude that the quantum mechanical description of physical reality given by wave functions is not complete.

For a complete description, they hypothesized that there are variables that correspond to all the elements of reality, giving rise to the phenomenon of non-commuting quantum observables and the seemingly nonlocal effect that the measurement on one particle has on the state of the other. Such a theory is called a local hidden variables (LHVs) theory. It is only until later in the same year that Erwin Schrödinger used the term ‘entanglement’ to describe this kind of non-classical connection between the particles (an English translation of the original 1935 paper in German can be found in [68]).

In 1951 David Bohm came up with an alternative version of the EPR thought experiment [36] based on electron spins. This came to be known as the EPR-Bohm (EPRB) experiment. In the thought experiment (Fig. 1.3), he considered a source of electrons and positrons from the decay of a neutral  $\pi$  meson:

$$\pi^0 \rightarrow e^- + e^+.$$

As the pion has zero spin, by conservation of angular momentum, the electron and positron are in a singlet configuration described by:

$$|\psi^-\rangle = \frac{1}{\sqrt{2}}(|\uparrow_{e^-}\rangle_A |\downarrow_{e^+}\rangle_B - |\downarrow_{e^-}\rangle_A |\uparrow_{e^+}\rangle_B). \quad (1.2)$$

Spin measurement of either the electron or positron in any arbitrary direction  $\vec{a}$ ,  $\vec{b}$ , or  $\vec{c}$  will have an equal probability of yielding spin-up or spin-down. However, when comparing the results of the spin of both particles measured in the same direction, they showed perfect anti-correlation. Such a two-particle system is said to be in an entangled state. The state of such a system as described by Eq. 1.2 can no longer be factorized into the product of two individual states. Based on the Bohm experiment, John S. Bell came up with the Bell’s inequality [69] in 1964, which allows the prediction of quantum mechanics and LHV theories to be distinguished. It is derived based on arguments about measurement probabilities that result from classical correlations alone and imposes an upper limit for it. Quantum mechanics which can lead to stronger correlations will violate this limit. The original form of the

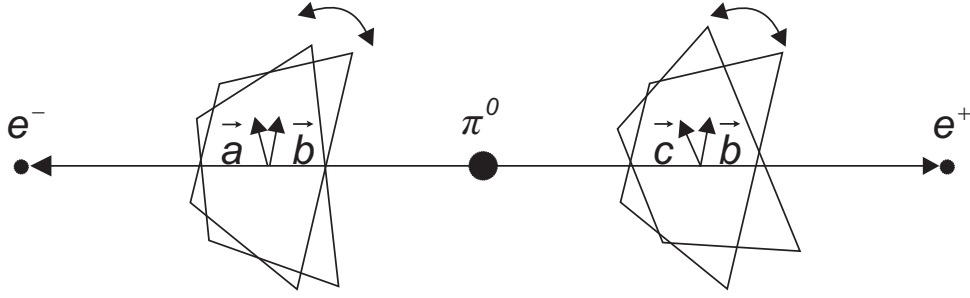


Fig. 1.3 The Einstein-Podolsky-Rosen-Bohm (EPR-Bohm) thought experiment. An alternative version of the EPR experiment proposed by David Bohm in 1951 [36]. In the experiment, the decay of a neutral  $\pi$  meson acts as a source of electrons and positrons which are entangled in their spins. Spin measurement of either the electron or positron in any arbitrary direction  $\vec{a}$ ,  $\vec{b}$ , or  $\vec{c}$  will have an equal probability of yielding spin-up and spin-down. However, when comparing the results of the spin measurement of both particles measured in the same direction, they show perfect anti-correlation.

Bell's inequality is written as:

$$|P(\vec{a}, \vec{b}) - P(\vec{a}, \vec{c})| \leq 1 + P(\vec{b}, \vec{b}) \quad (1.3)$$

where  $\vec{a}$ ,  $\vec{b}$ , or  $\vec{c}$  are the direction of the spin measurements shown in Fig. 1.3.  $P(\vec{a}, \vec{b})$  is the average value product of the spins measured in direction  $\vec{a}$  and  $\vec{b}$ , respectively. The measurement results will violate the Bell's inequality only for certain systems when there is quantum entanglement between the particles. In 1969 John F. Clauser, Micheal A. Horne, Abner Shimony, and Richard A. Holt rederived Bell's inequality in a form that is no longer restricted to experiments where the measurement results only have two possible outcomes. This inequality later came to be known as the CHSH inequality [70]. It includes an experimentally determinable parameter  $S$  which is defined by

$$S = E(a_0, b_0) - E(a_0, b_1) + E(a_1, b_0) + E(a_1, b_1). \quad (1.4)$$

The correlation function  $E(a_0, b_0)$  for measurements with only two possible outcomes as in the case of Fig. 1.3 is given by:

$$E(a_0, b_0) = P(\uparrow\uparrow | a_0, b_0) - P(\uparrow\downarrow | a_0, b_0) - P(\downarrow\uparrow | a_0, b_0) + P(\downarrow\downarrow | a_0, b_0), \quad (1.5)$$

where  $P(\uparrow\uparrow | a_0, b_0)$  is the probability of obtaining spin-up for both particles with detectors orientated at angle  $a_0$  and  $b_0$ , respectively.

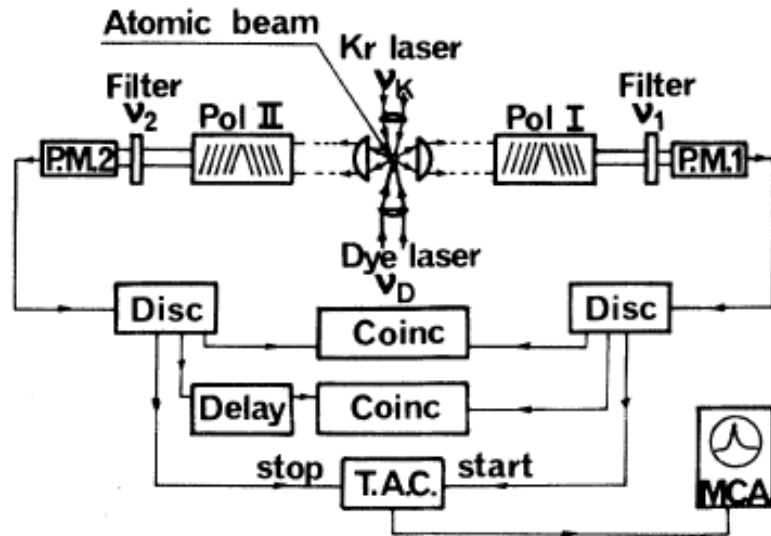


Fig. 1.4 The experimental setup used by Alain Aspect *et al.* in the early 1980s to violate the Bell's inequality. The polarization-entangled photons are generated via radiative atomic cascade of calcium. The photons then pass through the polarizers (Pol), consisting of glass plates stacked at Brewster angle, and are detected by photomultiplier tubes (PM). A combination of a time-to-amplitude converter (T.A.C.) and a coincidence circuit detects photons arriving within 19 ns of each other. With the setup, they observed a violation of the Bell's inequality by up to 9 standard deviations. (Figure adapted from [6])

For classical correlation, the parameter  $S$  will take values  $|S| \leq 2$ . The stronger quantum correlation will result in the violation of this inequality. Thus the parameter  $S$  can be used to quantify whether there is entanglement in a system above the limit expected from classical correlations alone.

It should be noted that due to the model on which the CHSH inequality is based, it is only applicable to bipartite systems containing even numbers of particles, i.e. the particles are distributed evenly between two modes. A description of a special case of a Bell's inequality for three particles can be found in [71]. In the early 1980s, Alain Aspect *et al.* conducted a series of experiments [6, 72, 73] aimed at violating the Bell's inequality. In their experimental setup (Fig. 1.4), the polarization-entangled photons are generated via radiative atomic cascade of calcium. The photons then pass through the polarizers (Pol), consisting of glass plates stacked at Brewster angle, and are detected by photomultiplier tubes (PM). A combination of a time-to-amplitude converter (T.A.C.) and a coincidence circuit detect photons arriving within 19 ns of each other. With this setup, they observed a violation of the Bell's inequality by up to 9 standard deviations.

From that point on, there have been numerous realizations of the Bohm-type experiment using various entangled quantum systems. Currently, the polarization degree of freedom of the photon is by far the most commonly used physical property to encode the qubit. In the Aspect experiments, these polarization-entangled photons are generated by the atomic cascade of calcium. This has been replaced by the process of spontaneous parametric down-conversion (SPDC) in non-linear optical media (detail about the process can be found in Chapter 2) for the generation of entangled photons in modern experiments.

## 1.2 Thesis Outline

We begin this thesis in Chapter 2 by briefly explaining the theory behind SPDC and its experimental application in sources of polarization-entangled photon pairs. We will also cover the derivation of some of the mathematical models used to predict and interpret the results of projective measurement [67] done on these entangled photon pair source. We then use these models to predict expected results from characterization of these sources with various noise contributions.

This is followed by a report of our experimental attempt to closely approach Tsirelson's bound [4], specifically the theoretical maximum violation of the CHSH inequality [70] with  $S = 2\sqrt{2}$ , in Chapter 3. We will briefly discuss the motivation, both from a fundamental and practical standpoint, for the experiment and recount some of the experimental considerations and procedures required to setup a high quality polarization-entangled photon pair source to violate the CHSH inequality maximally. We then highlight some of the possible implications of the result obtained.

In Chapter 4, we will examine an idea first proposed by Turing and von Neumann [74] that physical processes can be considered as computations performed on some universal machine and that the complexity of observed phenomena is closely related to the complexity of computational resources needed to simulate them [75]. We will highlight the concept of Kolmogorov complexity and its use in the *Normalized Information Distance* (NID) [26] that allows for the comparison of two data sets without detailed knowledge of their origin. We then show how an approximation to NID can be obtained by appealing to the compressibility of the data sets obtained using freely available compression softwares. We will go in-depth about our choice of the compression software that we use and the experimental implementation of an Bell type measurement based solely on complexity considerations.

We cover in Chapter 5, details regarding the generation of energy-time entangled states and give an overview of how a bipartite quantum system consisting of either the energy-time or polarization degree of freedom can be expanded for the generation of higher dimensional

states in an experimental implementation. Specifics on the hyperentanglement [76–78] of the energy-time and polarization degrees of freedom are also discussed.

Building on what we have learnt in the previous chapter regarding the generation of higher dimensional quantum states, we examine an experimental estimation of the dimension witness quantum systems based on the CGLMP inequality [35] in Chapter 6. Prior to that we will derive the CGLMP inequality for a bipartite system with four outcomes and recount the various experimental procedures needed for the implementation of a hyperentangled state in this experiment.

Lastly, we will wrap up all our findings in this thesis with some concluding remarks in Chapter 7.



## Chapter 2

# Generation of Polarization-Entangled Photons and Their Characterization

Entanglement, one of the essential features exhibited by some composite quantum systems, sets quantum mechanics apart from classical physics. It is the connection that exists between the components of these composite quantum systems and renders them describable only as collective entities rather than a consolidation of descriptions of individual components. Since there is no such equivalence in classical physics, it comes as no surprise that many experiments designed to gain insights into quantum mechanics involved the generation of entangled states encoded in these composite quantum systems and fundamental tests being conducted on them.

The first of such experiments paving the way for the generation of entangled states (Fig. 2.1), implemented by Kocher *et al.* in 1967 [37], was photonic-based. It utilized the process of atomic cascade in Ca (Fig. 2.2) to generate polarization-correlated photon pairs. Ultraviolet light from a H<sub>2</sub> arc lamp was used to excite a beam of Ca atoms from the ground state  $4s^2\ ^1S_0$  to the excited state  $3d4p\ ^1P_1$ . The Ca atoms then decay to the desired  $4p^2\ ^1S_0$  level through spontaneous decay. Further de-excitation of the Ca atoms via the  $4p4s\ ^1P_1$  level back to the ground state produces a 551.3 nm and 422.7 nm photon in the process.

As there was no net change both in the total angular momentum  $J$  and the parity of the initial and final state of the atom, the emitted photons in each pair exhibited polarization correlations. This was shown to be the case by comparing the number of photon pairs detected (coincidence counts) within a certain time interval (coincidence time window), after a pair of parallel and crossed polarizers. In the early 1980s, using similar techniques, Aspect *et al.* [6, 72, 73] successfully implemented a source of polarization-entangled photon pairs that violated Bell's inequality [69, 70, 79] by up to 9 standard deviations.

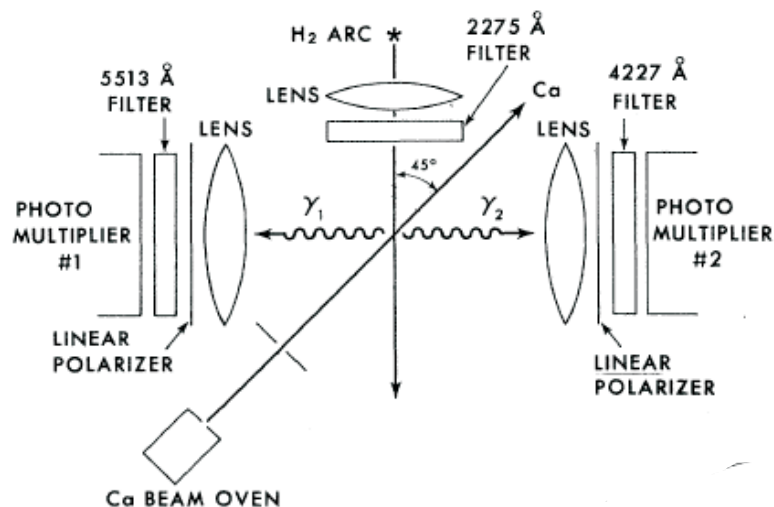


Fig. 2.1 The experimental setup used by Kocher *et al.* in 1967 to generate polarization-correlated photon pairs. Ultraviolet light from a  $H_2$  arc lamp excited a beam of Ca atoms. Polarization-correlated photon pairs were generated when the excited Ca atoms decayed back to the ground state via an intermediate level (Fig. 2.2). These photon pairs then passed through linear polarizers followed by narrowband interference filters to be detected by photomultiplier tubes. (Figure adapted from [37].)

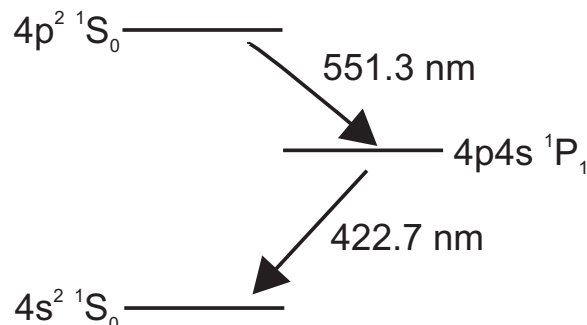


Fig. 2.2 The atomic cascade of Ca. Each Ca atom de-excites from the excited  $4p^2 \ ^1S_0$  level via the  $4p4s \ ^1P_1$  level back to the ground state producing a 551.3 nm and 422.7 nm photon. The emitted photon pairs carry no net angular momentum as  $J = 0$  for both the initial and final states of the cascade. Coupled with the fact that both levels have the same even parity, the photons in each pair will exhibit polarization correlation.

Parallel developments also saw major progress being made in the field of non-linear optics which resulted in the first experimental implementation of a photon pair source (Fig. 2.3) based on the non-linear optical effect of spontaneous parametric down-conversion (SPDC) by Burnham *et al.* [38] in 1970. With SPDC, photon pairs entangled in various degrees of

freedom [60, 62, 80] can be implemented. These sources find applications in areas like quantum key distribution [81] and fundamental tests of quantum physics (e.g. tests of Leggett models [46, 82]). SPDC remains to date a routinely used technique in experiments involving the generation of correlated and entangled photon pairs.

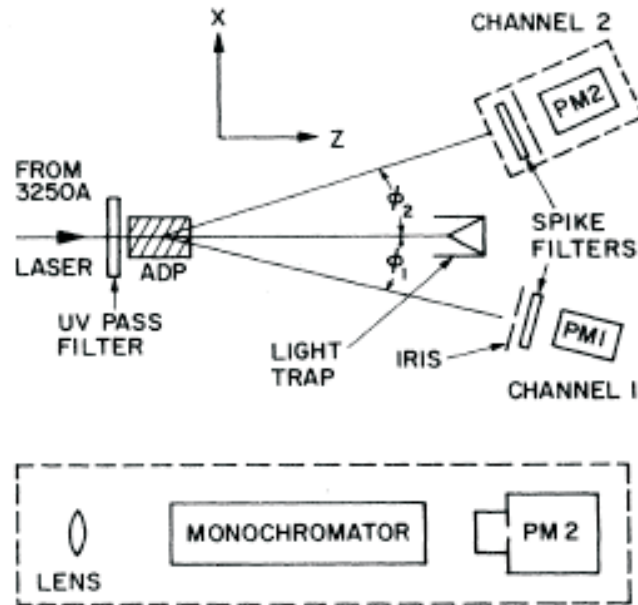


Fig. 2.3 The first photon pair source based on the process of SPDC was implemented by Burnham *et al.* in 1970. An ammonium dihydrogen phosphate (ADP) crystal is pumped by a 325 nm beam from a He-Cd laser. The ADP crystal is cut in such a way that the optical axis makes an angle of  $52.4^\circ$  with the normal of the faces to satisfy the condition of phase-matching. The down-converted photons then pass through a combination of spatial (iris) and spectral filtering (spike filter consisting of a monochromator) to be detected with the photomultiplier (PM) tubes. (Figure adapted from [38].)

In this Chapter, we will begin by briefly describing, in Section 2.1, the theory behind second-order non-linear optical phenomena which gives rise to the process of SPDC. This is followed by an in-depth discussion on the process of SPDC in Section 2.2 and how it is used to generate polarization-entangled photon pairs in Section 2.3. A derivation of the expected result for various polarization measurements based on a maximally-entangled theoretical model for the generated entangled state is provided in Section 2.4. Lastly, we will cover the various factors affecting quality polarization entanglement and how these factors can be easily characterized by probing the polarization correlation in various bases in Section 2.5.

## 2.1 Second-order Non-linear Optical Phenomena

The process of SPDC is suited for use in the generation of entangled photons. These photonic qubits can be easily encoded in one or any combinations of several degrees of freedom, namely polarization [62], energy-time [60] (time-bin), and orbital angular momentum [80]. They are relatively resistant against decoherence, allowing them to travel long distances without suffering degradation from their initial state. They can be manipulated and detected with relative ease as the techniques involved have been studied in great detail [83, 84].

To understand the process of SPDC, a second-order non-linear optical phenomenon, we need to appeal to the behavior of the electrons and positively charged nuclei of the atoms in a dielectric material when subjected to an electric field. Upon application of an external electric field  $\mathbf{E}$  on the dielectric material, the electrons and the positively charged nucleus in each atom redistributes themselves polarizing the atom. The atoms then acquire a small dipole moment that is aligned to the direction of the applied electric field. In the regime where the applied electric field is weak, the response of the dielectric material is linear with the applied electric field. This behavior can be written as:

$$\mathbf{P} \approx \epsilon_0 \chi \mathbf{E}, \quad (2.1)$$

where  $\mathbf{P}$  is the electric polarization (dipole moment per unit volume) induced in the dielectric material,  $\epsilon_0$  is the electric permittivity of free space,  $\chi$  is the linear electric susceptibility, and  $\mathbf{E}$  is the applied electric field. The susceptibility  $\chi$  is related to the refractive index of the dielectric material. For an isotropic medium, the susceptibility  $\chi$  only has one value which describes the refraction or dispersion characteristics of the electric field in the dielectric medium. For a crystalline material, the susceptibility  $\chi$  is a tensor quantity related to the symmetry of the crystal structure.

When large electric field amplitudes are applied, e.g. situation found in the light waves from the output of some lasers, higher-order contributions become significant. The linear behavior described by Eq. 2.1 needs to be modified with additional terms. In component form, the modifications are given by:

$$P_i = \epsilon_0 \chi_{ij}^{(1)} E_j + \epsilon_0 \chi_{ijk}^{(2)} E_j E_k + \dots + \epsilon_0 \chi_{ijk\dots l}^{(n)} E_j E_k \dots E_l, \quad (2.2)$$

where  $E$  is the applied electric field,  $i, j, \dots, k \in (1, 2, 3)$ , and  $\chi^{(n)}$  is the  $n$ th-order susceptibility. Of particular interest to us is the second-order susceptibility  $\chi^{(2)}$  as it allows us to setup a relation between three electric fields in the material. This underlying mechanism is

ultimately responsible for various three-wave mixing processes<sup>1</sup>, e.g. in SPDC this is seen as a pump light electric field giving rise to a signal and idler light<sup>2</sup> electric field.

## 2.2 Spontaneous Parametric Down-conversion (SPDC)

The theory of SPDC was established by Klyshko [87] in 1970 while the modern quantum mechanical description was provided by Hong *et al.* [88] in 1985. In SPDC, a pump photon of frequency  $\omega_p$  gets annihilated producing a signal and idler photon with frequency  $\omega_s$  and  $\omega_i$ , respectively. The term parametric in SPDC refers to the fact that the down-conversion medium is left unchanged by the process. Thus, this necessitates a series of conservation laws [89] that must be satisfied by the pump, signal, and idler photons. The conservation laws, in the limit of an infinite medium, are given by:

$$\omega_p = \omega_s + \omega_i, \quad (2.3a)$$

$$\vec{k}_p = \vec{k}_s + \vec{k}_i, \quad (2.3b)$$

where Eq. 2.3a and Eq. 2.3b are statements of energy and momentum conservation, respectively. In the field of non-linear optics, these statements are also known respectively as the frequency-matching and phase-matching conditions. The dispersion relation of the wavevectors in Eq. 2.3b is given by:

$$\vec{k}_j = \frac{n_j(\omega_j)\omega_j}{c}\hat{s}_j,$$

where  $n_j(\omega_j)$  is a dispersive refractive index of a material dependent on frequency  $\omega_j$ ,  $\hat{s}_j$  is the unit vector pointing in the  $\vec{k}_j$  direction, and  $c$  is the speed of light, allowing us to rewrite Eq. 2.3b into:

$$n_p(\omega_p)\omega_p\hat{s}_p = n_s(\omega_s)\omega_s\hat{s}_s + n_i(\omega_i)\omega_i\hat{s}_i. \quad (2.4)$$

For the special case of an isotropic medium, i.e.  $n_p = n_s = n_i = n$ , and degenerate down-conversion, i.e.  $\omega_s = \omega_i = \frac{\omega_p}{2}$ , the minimum magnitude of  $|\vec{k}_s| + |\vec{k}_i|$  that can still satisfy the condition of momentum conservation (Eq. 2.3b) occurs when the down-converted light is collinear with that of the pump. The expression in Eq. 2.4 then reduces to:

$$n(\omega_p) = n\left(\frac{\omega_p}{2}\right).$$

<sup>1</sup>A brief introduction of the various three-wave mixing processes can be found in [85]

<sup>2</sup>This naming convention has its origin in early research on optical parametric amplifiers [86] where only one of the two output modes (signal) is useful. The unused mode is called the idler.

Since the refractive index  $n$  for most dielectric materials increases with increasing frequency [86], both frequency and phase-matching conditions cannot be simultaneously satisfied in an isotropic medium. To overcome this, there needs to be two channels into which the down-conversion can occur. This can be achieved in a birefringent medium,  $\beta$ -Barium-Borate (BBO) crystal in our case, where there are two different refractive indices  $n_o$  and  $n_e$  for the ordinarily ( $o$ ) and extraordinarily ( $e$ ) polarized light<sup>3</sup>, respectively. The phase matching condition (Eq. 2.4) assuming an  $e$ -polarized pump can now be written in terms of  $n_o$  and  $n_e$ , most commonly as the following:

$$n_e(\omega_p)\omega_p\hat{s}_p = n_o(\omega_s)\omega_s\hat{s}_o + n_o(\omega_i)\omega_i\hat{s}_o, \quad (2.5a)$$

$$n_e(\omega_p)\omega_p\hat{s}_p = n_e(\omega_s)\omega_s\hat{s}_e + n_o(\omega_i)\omega_i\hat{s}_o. \quad (2.5b)$$

In Eq. 2.5a, also called type-I phase-matching, both the signal and idler have the same polarization. This is in contrast to type-II phase-matching in Eq. 2.5b, where the signal and idler have the orthogonal polarization. For the purpose of this thesis, I will only focus the discussion on type-II phase-matching.

## 2.3 Generation of Polarization-Entangled Photon Pairs

In type-II phase-matched SPDC, the wavelength degenerate<sup>4</sup>  $o$  and  $e$ -polarized photons are emitted from the down-conversion crystal in two distinct respective cones (Fig. 2.4) which are non-concentric with the pump beam and each other. Due to Eq. 2.3b, the emission directions of the two photons in each pair are always symmetric about the pump direction. Since we orientate the down-conversion crystal such that the extraordinary axis coincides with the vertical ( $V$ ) polarization, while the ordinary axis coincides with the horizontal ( $H$ ) polarization in the experimental setup reported in the later chapters, and we give the down-converted photons the labels of  $H_o$  and  $V_e$ , respectively.

It is noteworthy to mention that as we are operating in the regime of a continuous wave (CW) narrowband pump, the differences in the spectral bandwidth of the down-converted light due to dispersion induced by the propagation of the  $o$  and  $e$ -polarized photons through the birefringent crystal is negligible<sup>5</sup>, thus rendering the  $H$  and  $V$  photon indistinguishable in the spectral degree of freedom. However, as we still need to contend with the distin-

<sup>3</sup>The term "ordinary" and "extraordinary" refers to the slow and fast axis of a birefringent crystal, respectively.

<sup>4</sup>This is chosen such that the down-converted photos in each pair are only distinguishable in the polarization degree of freedom.

<sup>5</sup>This is in contrast to the case where a pulsed broadband pump is used [90].

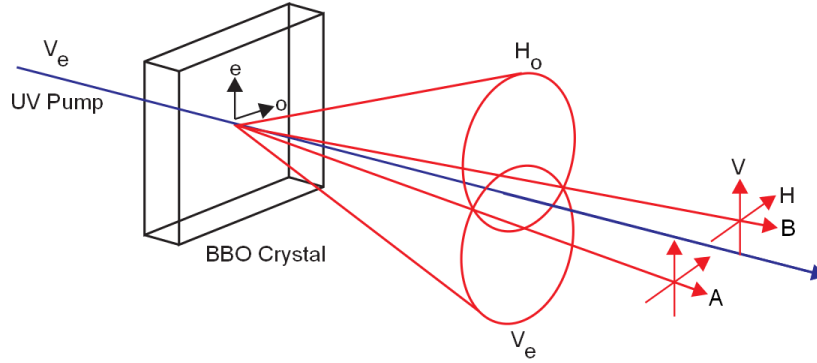


Fig. 2.4 Type-II phase matched down-conversion. In type-II phase matching, an  $e$ -polarized pump photon gets down-converted into a pair of  $o$  and  $e$ -polarized photons of lower energy. The  $o$  and  $e$ -polarized photons are emitted from the down-conversion crystal in two respective cones which are non-concentric with either the pump beam or each other. In our setup, the down-conversion crystal is oriented in such a way that the extraordinary axis coincides with the vertical ( $V$ ) polarization, while the ordinary axis coincides with the horizontal ( $H$ ) polarization. These two cases are denoted as  $V_e$  and  $H_o$ , respectively.

guishability in the temporal degree of freedom, the label of  $o$  and  $e$  polarization will be retained for the moment. The reason for the distinguishability in this degree of freedom will be highlighted in Section 2.3.1.

For the generation of polarization-entangled photon pairs, we need two possible decay paths given by the polarization combinations  $|H_o\rangle|V_e\rangle$  and  $|V_e\rangle|H_o\rangle$ . This situation can only be found at the two intersections of the  $H_o$  and  $V_e$  emission cones, which also define two spatial modes  $A$  and  $B$ , denoting Alice and Bob, respectively. This is called a "crossed-ring" configuration<sup>6</sup> [7, 63, 93].

The things that we have covered so far are still limited to the domain of classical wave theory and thus are not able to explain the spontaneous pair emission when signal and idler are initially in a vacuum state. SPDC can only be understood in the "quantum description" of three-wave mixing where the process is stimulated by random vacuum fluctuations. The quantum mechanical creation operator for the two-photon polarization state describing such a situation can be written as<sup>7</sup>:

$$|\psi\rangle = C \left( a_{H_o}^\dagger b_{V_e}^\dagger + e^{i\phi} a_{V_e}^\dagger b_{H_o}^\dagger \right) |0\rangle,$$

<sup>6</sup>Down-conversion setups can also be implemented in the "beamlike" [91] and collinear [92] configuration.

<sup>7</sup>This is the lowest order approximation of the squeezing operator and does not account for the higher order emissions of SPDC (i.e. multipair emission), which may be important in fully describing certain systems using SPDC.

where  $C$  is the normalization constant,  $a_i^\dagger$  and  $b_i^\dagger$  are the creation operators of a photon with polarization state  $i$  in spatial mode  $A$  and  $B$ , respectively<sup>8</sup>. After normalization, the following polarization-entangled two-photon state:

$$|\psi\rangle = \frac{1}{\sqrt{2}} \left( |H_o\rangle_A |V_e\rangle_B + e^{i\phi} |V_e\rangle_A |H_o\rangle_B \right), \quad (2.6)$$

is obtained.

### 2.3.1 Compensation of Longitudinal and Transverse Walk-Off

In actuality, the photon pairs found at the intersection of the  $o$  and  $e$  emission cone (Fig. 2.4) are not in a pure polarization-entangled state (Eq. 2.6). The differences in refractive index  $n_o$  and  $n_e$  of the birefringent crystal result in a difference in the propagation velocity of the  $o$  and  $e$ -polarized photons through the crystal. This gives rise to a relative delay between the arrival time of the photon in each pair that is dependent on the site in the crystal where they are created.

In one extreme case (Fig 2.5a), the photon pairs are created at the face of the crystal incident to the pump beam. This give rise to the maximum time difference between the arrival time of the  $o$  and  $e$ -polarized photon at the detectors. At the other extreme (Fig. 2.5b), the photon pairs are created at the face where the pump exits the crystal. Thus, there is no relative delay between the  $o$  and  $e$ -polarized photons. Only the photon pair combinations  $|H_o\rangle_A |V_e\rangle_B$  and  $|V_e\rangle_A |H_o\rangle_B$  created here are truly indistinguishable and exist in a pure polarization state. However, when the photon pairs from all the creation sites are included, a mixed state is produced which in turn lowers the polarization entanglement quality.

It should be noted that this problem of temporal distinguishability between the photon pairs cannot be eliminated simply by having a coincidence time window to be greater than the maximum relative delay expected. This is due to the fact that entanglement in the state  $|\psi^-\rangle$  (Eq. 2.6) is a process involving two-photon interference between the two Feynman alternatives creating the  $|H_o\rangle_A |V_e\rangle_B$  and  $|V_e\rangle_A |H_o\rangle_B$  combination. Thus, any distinguishability of the two decay paths in degrees of freedom that are not resolved will still manifest itself in the result of certain measurement.

A common way to eliminate this problem [7] involves the use of a combination of half-wave plates ( $\lambda/2$ ) and compensation crystals (CC) (Fig. 2.5). The photons in each spatial mode first pass through a  $\lambda/2$  with its fast axis aligned such that it rotates their polarization by  $90^\circ$ . This is followed by the CC which are identical to the crystal used

<sup>8</sup>Such a representation of the number of photons with a specific polarization in each spatial mode is called a Fock state. The creation operator  $a^\dagger$  obeys the relation,  $a^\dagger|n\rangle = \sqrt{n+1}|n+1\rangle$

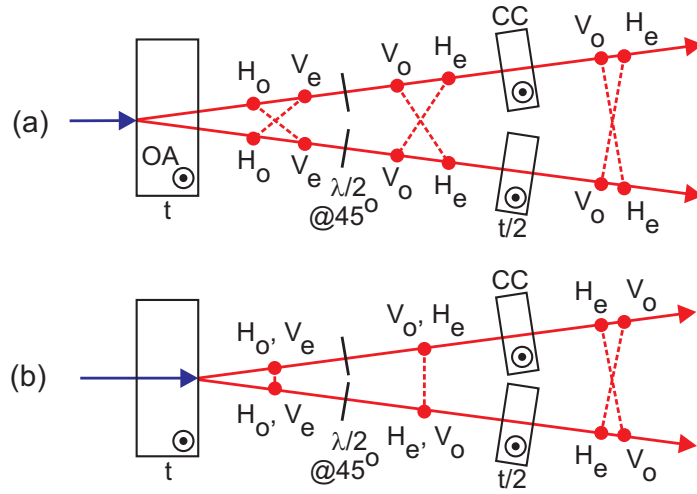


Fig. 2.5 Compensation of temporal walkoff. The photons first pass through a half wave plate ( $\lambda/2$ ) which rotates their polarization by  $90^\circ$ . This is followed by compensation crystals (CC) which are identical to the crystal used for down-conversion except with half the thickness. The optical axis (OA) of both CC are aligned in the same direction as that of the down-conversion crystal. In the first extreme case (a), the CC will halve the relative delay between the photons in the pair. In the second extreme case (b), the CC will induce a relative delay equal to that in the previous case between the photons in the pair. Thus, the photons pairs from these two cases are indistinguishable in the temporal degree of freedom, resulting in a pure polarization-entangled state. This is also true for all complementary creation sites in the crystal symmetric about the center of the crystal. For photon pairs created right in the center of the down-conversion crystal, the relative delay is just eliminated by the CC.

for down-conversion except with half the thickness. The optical axis (OA) of both CC are aligned in the same direction as that of the down-conversion crystal. In the first extreme case (Fig. 2.5a), the CC will halve the relative delay between the photons in the pair. In the second extreme case (Fig. 2.5b), the CC will induce a relative delay equal to that in the previous case between the photons in the pair. Thus, the photons pairs from these two cases are indistinguishable in the temporal degree of freedom, resulting in a pure polarization-entangled state. This is also true for all complementary creation sites in the crystal symmetric about the center of the crystal. For photon pairs created right in the center of the down-conversion crystal, the relative delay is just eliminated by the CC. Since photons in each pair are now indistinguishable apart from their polarization  $H$  and  $V$ , the  $o$  and  $e$  label can be dropped from Eq. 2.6, giving us:

$$|\psi\rangle = \frac{1}{\sqrt{2}} \left( |H\rangle_A |V\rangle_B + e^{i\phi} |V\rangle_A |H\rangle_B \right). \quad (2.7)$$

Apart from eliminating the problem of temporal distinguishability, the CC are also used to compensate for the transverse walkoff (Fig. 2.6) between the down-converted  $o$  and  $e$ -polarized light. To satisfy the phase-matching condition in Eq. 2.3b, the axis perpendicular to both the fast and slow axis of the down-conversion crystal is usually tilted at an vertical angle to the pump beam. This results in a slightly different profile for the  $o$  and  $e$  emission cones. At each of the intersection of the emission cones, this will appear as an elongated spread of the  $o$ -polarized photon distribution as compared to that of the  $e$ -polarized photons. After passing through the  $\lambda/2$ , the polarization of the photons are rotated by  $90^\circ$ . The CC, which are orientated such that their OA are parallel to that of the down-conversion crystal, then cause a shift in the path of the down-converted light, coinciding the center for the distribution of the  $o$  and  $e$ -polarized photons. In conjunction with the matching of the waist of the pump beam and collection modes [63], this provides a better collection efficiency into single mode optical fibers.

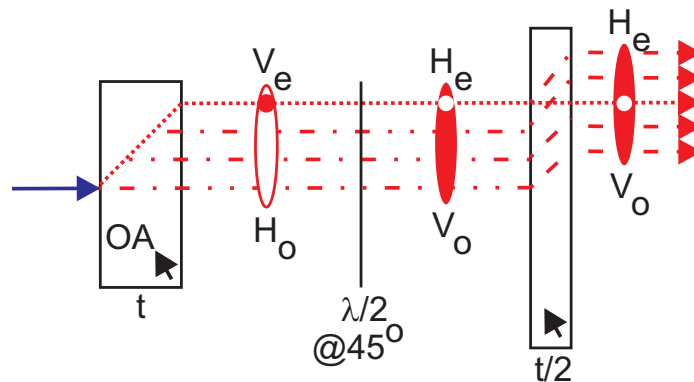


Fig. 2.6 Compensation of transverse walkoff. At each of the intersection of the emission cones, there is an elongated spread of the  $o$ -polarized photons as compared to the  $e$ -polarized photons. After passing through the  $\lambda/2$ , the polarization of the photons are rotated by  $90^\circ$ . The CC, which are orientated such that their OA are parallel to that of the down-conversion crystal, then cause a shift in the path of the down-converted light such that the center for the distribution of the  $o$  and  $e$ -polarized photons coincide. This provide better overlap between the two distributions and thus results in a better spatial mode for collection into single mode optical fibers.

The vertical angle between the fast axis of the CC and the down-converted light beam can be adjusted by tilting the CC. This changes the relative phase between the  $H$  and  $V$  photons in each of the spatial mode and thus the free phase  $\phi$  in Eq. 2.7. This adjustment of the free phase  $\phi$  in combination with local rotation of the polarization of the down-converted photons in each spatial mode then allows us to generate any of the four maximally-entangled

Bell states:

$$\begin{aligned}
|\psi^-\rangle &= \frac{1}{\sqrt{2}}(|H\rangle_A|V\rangle_B - |V\rangle_A|H\rangle_B), \\
|\psi^+\rangle &= \frac{1}{\sqrt{2}}(|H\rangle_A|V\rangle_B + |V\rangle_A|H\rangle_B), \\
|\phi^-\rangle &= \frac{1}{\sqrt{2}}(|H\rangle_A|H\rangle_B - |V\rangle_A|V\rangle_B), \\
|\phi^+\rangle &= \frac{1}{\sqrt{2}}(|H\rangle_A|H\rangle_B + |V\rangle_A|V\rangle_B).
\end{aligned} \tag{2.8}$$

## 2.4 Joint Detection Probability for Two-Photon Polarization-Entangled States

Quantum mechanics has the interpretation of being probabilistic in nature. Thus experiments to address questions in this field rely heavily on establishing the probability distributions of various measurement outcomes in order to reach their conclusions. For experiments involving bipartite entangled states, like those documented in the later chapters, the joint detection probability distributions, probability distributions of simultaneous detection events registered by the two parties, are measured.

Thus in order for us to better interpret the results from such measurements and to fit them to the available theoretical models for establishing various parameters, we need to derive analytical expressions describing the expected joint probability distribution of outcomes with different measurement bases given a model for the initial entangled state.

For the purpose of this thesis, we will limit our derivation here to the case of the joint probability of detection for the maximally-entangled two-photon polarization state  $|\psi^-\rangle$  (Eq. 2.8) for various linear polarization measurement bases.

We begin our derivation by considering the case of single photon polarization states. In the Jones vector notation<sup>9</sup>, the two single photon polarization basis states  $|H\rangle$  and  $|V\rangle$  are given by the column vectors:

$$|H\rangle = \begin{pmatrix} 1 \\ 0 \end{pmatrix}, |V\rangle = \begin{pmatrix} 0 \\ 1 \end{pmatrix},$$

respectively.

---

<sup>9</sup>It should be noted that the Jones vector notation is only valid for pure polarization states. For mixed polarization states, the Stokes vector notation needs to be applied.

When this is extended to the two-photon polarization states, an increased Hilbert space results, with four bases given by  $|H\rangle_A|H\rangle_B$ ,  $|H\rangle_A|V\rangle_B$ ,  $|V\rangle_A|H\rangle_B$ , and  $|V\rangle_A|V\rangle_B$ . The Jones vector notation describing the basis state  $|H\rangle_A|H\rangle_B$  for example, is given by:

$$|H\rangle_A|H\rangle_B = \begin{pmatrix} 1 \\ 0 \end{pmatrix} \otimes \begin{pmatrix} 1 \\ 0 \end{pmatrix} = \begin{pmatrix} 1 \\ 0 \\ 0 \\ 0 \end{pmatrix}.$$

In a similar fashion, we define an expanded rotation matrix given by:

$$R^{(2)}(\theta_A, \theta_B) = R(\theta_A) \otimes R(\theta_B),$$

where  $R(\theta_A)$  and  $R(\theta_B)$  are the local polarization rotations performed in spatial mode  $A$  and  $B$ , respectively. Applying the the expanded rotation matrix  $R^{(2)}(\theta_A, \theta_B)$  on basis  $|H\rangle_A|H\rangle_B$  we arrive at the rotated basis:

$$|\Phi\rangle = R(\theta_A, \theta_B)|H\rangle_A|H\rangle_B.$$

Thus joint detection probability of obtaining the measurement result  $|H\rangle_A|H\rangle_B$  with analyzer settings  $\theta_A$  and  $\theta_B$  for the input state  $|\psi^-\rangle$  (Eq. 2.8) is thus given by:

$$\begin{aligned} P_{HH}(\theta_A, \theta_B) &= \text{tr}(\rho_{\text{pure}} P_{|\Phi\rangle}) \\ &= \frac{1 - \cos[2(\theta_A - \theta_B)]}{4}, \end{aligned} \quad (2.9)$$

where  $\rho_{\text{pure}} = |\psi^-\rangle\langle\psi^-|$  and  $P_{|\Phi\rangle} = |\Phi\rangle\langle\Phi|$ . The same probability distribution is also obtained for any other degrees of freedom. Applying the same procedures, this derivation can be easily generalized to systems with more than two degrees of freedom or other measurement bases.

## 2.5 Characterization of Polarization-Entangled Photon Pairs

There are a number of measures and methods for assessing entanglement quality [70, 94, 95] of quantum systems. One can even appeal to full tomographic reconstructions [96, 97] of the quantum state of the system being investigated for the same purpose. However, the

sometimes experimentally complex or numerous measurements required for such characterizations coupled with need for significant post-processing of the acquired data mean that such measures and methods may not always be possible or practical. For example, to optimize the alignment of the down-conversion source mentioned in Section 2.3, one may need to perform numerous iterations of small adjustments to the pointing direction of the collection optics followed by a characterization of the quality of polarization-entanglement with the new alignment. Since the model for the entangled state being generated and the form of the noise contribution lowering the entanglement quality is known, it is possible to come up with a less general entanglement measure that is experimentally simple and can be carried out quickly.

A simple and routinely used method to assess the quality of polarization entanglement given the generated state can be approximated by one of the four maximally-entangled Bell states (Eq. 2.8) is to probe the visibilities of its linear polarization correlations in various bases. The procedure involves tabulating the coincidence counts obtained with the axis of the polarizer in one of the spatial modes set at  $H$  or  $V$  (the natural basis) and  $+45^\circ$  or  $-45^\circ$  (the complimentary basis), while rotating the axis of polarizer in the other.

A sinusoidal function is then fitted to the data and the fitted parameters used to calculate the phases of the curves and their maxima and minima for the evaluation of the visibilities. The two visibilities denoted respectively as  $V_{HV}$  and  $V_{45}$ , are given by:

$$V_{HV} = \frac{|C_{HV} - C_{HH}|}{C_{HV} + C_{HH}}, \quad (2.10a)$$

$$V_{45} = \frac{|C_{+-} - C_{++}|}{C_{+-} + C_{++}}, \quad (2.10b)$$

where  $C_{HV}$  or  $C_{+-}$  are the number of counts recorded when the polarizer in spatial mode A and B are set at  $H$  and  $V$  or  $+45^\circ$  and  $-45^\circ$ , respectively.

To understand how the visibilities in Eq. 2.10 are related to the quality of polarization entanglement, we first evaluate what are the expected outcomes for the state  $|\psi^-\rangle$  (Eq. 2.8). Setting  $\theta_A$  as  $0^\circ$  (H) and  $+45^\circ$  in Eq. 2.9 we get:

$$P_{HH}(H, \theta_B) = \frac{1 - \cos(2\theta_B)}{4}, \quad (2.11a)$$

$$P_{HH}(+45^\circ, \theta_B) = \frac{1 - \sin(2\theta_B)}{4}. \quad (2.11b)$$

Substituting the above results into Eq. 2.10, we get  $V_{HV} = V_{45} = 1$ . In addition, appealing to the result in Eq. 2.11b, it is thus possible in experiments to obtain the correct phase  $\phi$

(Eq. 2.6) to get the state  $|\psi^-\rangle$  by setting both  $\theta_A$  and  $\theta_B$  at  $+45^\circ$  and adjusting tilt of the CC until the minimum coincidence counts is obtained.

Now we consider the various contributions that will lead to a reduction of the entanglement quality. For the first case we, consider an imbalance between the decay path  $|H\rangle_A|V\rangle_B$  and  $|V\rangle_A|H\rangle_B$  which can be written in the form:

$$|\phi\rangle = \sqrt{p}|H\rangle_A|V\rangle_B - \sqrt{1-p}|V\rangle_A|H\rangle_B, \quad (2.12)$$

where  $|\phi\rangle \rightarrow |\psi^-\rangle$  when  $p = 0.5$ . Going through the same derivation steps but with state  $|\phi\rangle$  instead of  $|\psi^-\rangle$ , we get:

$$V_{HV} = 1, \\ V_{45} = 2\sqrt{p(1-p)}.$$

The results show  $V_{HV}$  is independent of  $p$  and is always 1. This is expected as  $V_{HV}$  post selects just one of decay paths in  $|\phi\rangle$  (Eq. 2.12). As for  $V_{45}$ , the visibility is the maximum for  $p = 0.5$  (balanced contribution from  $|H\rangle_A|V\rangle_B$  and  $|V\rangle_A|H\rangle_B$ ) and decreases as  $p \rightarrow 0$  or 1.

For the second case, we consider the two types of noise that will lower the quality of entanglement. They are given, in terms of density matrices, by the following:

$$\rho_{white} = \frac{1}{4}(|H\rangle_A|H\rangle_B\langle H|_A\langle H|_B + |H\rangle_A|V\rangle_B\langle H|_A\langle V|_B \\ + |V\rangle_A|H\rangle_B\langle V|_A\langle H|_B + |V\rangle_A|V\rangle_B\langle V|_A\langle V|_B), \quad (2.14a)$$

$$\rho_{colored} = \frac{1}{2}(|H\rangle_A|V\rangle_B\langle H|_A\langle V|_B + |V\rangle_A|H\rangle_B\langle V|_A\langle H|_B). \quad (2.14b)$$

As can be seen from Eq. 2.14a,  $\rho_{white}$  or white noise contains equal contributions from all possible combination of the basis states, while  $\rho_{colored}$  (Eq. 2.14b) or colored noise only contains terms of the entangled state,  $|\psi^-\rangle$  in our case. Depending on whether the distinguishability between decay channels is the main contribution to noise, in which case a natural choice is the "colored" state, whereas the "white" state describes a scenario when the background comes from multiple pairs<sup>10</sup>.

Since we are operating in the CW regime, the emission time of the down-converted photon pairs are random. Within the coincidence time window,  $\tau_C$ , we may be detecting photons from different pairs which are uncorrelated. The rate of coincidence counts due to

<sup>10</sup>These noise contributions originate from the 2nd order terms of the squeezing operator acting on vacuum.

these uncorrelated pairs, termed accidental count rate,  $R_{acc}$ , is given by:

$$R_{acc} = s_A \times s_B \times \tau_C, \quad (2.15)$$

where  $s_A$  and  $s_B$  are the count rate (singles rate) recorded locally in spatial mode A and B, respectively. These accidental events constitute a kind of white noise (Eq. 2.14a) that is dependent on  $\tau_C$  and single rates  $s_A$  and  $s_B$ .

In contrast to the CW cases, when the pump comes in short optical pulses, the production of the photon pairs within a pulse are well localized temporally and are correlated with each other. If the multiple photon pairs are not resolved during the detection, this will constitute a kind of colored noise (Eq. 2.14b).

Here we will look only at the case of white noise which is applicable to our situation. Taking the white noise contribution into consideration, the total density matrix is given by:

$$\rho_{mixed}(p) = p\rho_{pure} + (1 - p)\rho_{white},$$

where  $p$  now gives the proportion of  $\rho_{pure}$  and  $\rho_{noise}$ . Once again we derive  $V_{HV}$  and  $V_{45}$  but now for the case  $\rho_{mixed}$  and arrive at the simple result<sup>11</sup>:

$$V_{HV} = V_{45} = p,$$

where  $V_{HV}$  and  $V_{45}$  varies linearly with  $p$ .

Thus the results from this section suggest that a high visibility for  $V_{HV}$  and  $V_{45}$  is indicative of a high quality of polarization entanglement. Our derivation also suggest that white noise contributions play a significant role in lowering the entanglement quality. Given its link to the accidental counts, this contribution can be lowered by decreasing the pump power to reduce the singles rate,  $s_A$  and  $s_B$ , and reducing the coincidence time window  $\tau_C$ .

---

<sup>11</sup>For the sake of completeness, we state here the result for the case of colored noise (Eq. 2.14b) is given by visibilities  $V_{HV} = 1$  and  $V_{45} = p$ .



## Chapter 3

# Approaching Tsirelson's Bound in a Photon Pair Experiment

In 1964, John Stewart Bell published his seminal paper [69] entitled "On the Einstein Podolsky Rosen (EPR) paradox" where he presented an analogy (based on spin measurements on pairs of entangled electrons described by David Bohm in 1951 [36]) to the original EPR thought experiment [68]. Considering only classical correlations, specifically that correlations are described by a local hidden variable (LHV)  $\lambda$  determined at the source, Bell derived the Bell's inequality [79], based the assumptions of locality and realism of measurement results, which allows the prediction of quantum mechanics in or indeed any theory that allows non-classical correlations to be distinguished from that of LHVs theories in specific cases. Bell [69] showed that the results of measurements on quantum systems cannot be explained by LHVs, since they violate Bell's inequality with non-classical correlations between the outcomes of measurements of two distant locations  $A$  and  $B$ .

The original Bell's inequality was later rederived by Clauser *et al.* into an experimentally implementable form known as the CHSH inequality [70]. As in the case of the original Bell's inequality, the derivation of the CHSH inequality was based on two fundamental assumptions. The derivation starts by considering a bipartite system consisting of a pair of spin- $\frac{1}{2}$  particles. Conventionally, the two modes of the system are called Alice ( $A$ ) and Bob ( $B$ ), respectively. Two fundamental assumptions were made in the derivation:

1. Correlations between the result of measurements made by  $A$  and  $B$  can be accounted by a local realistic theory (specifically the LHV theory). In other words, the correlations can be explained by some local hidden variables, classical in nature, which are established at the source. This assumption is known as the "realism condition".

2. Measurements made by  $A$  and  $B$  are independent of each other<sup>1</sup>. This assumption is known as the "locality condition".

From the above assumptions, the joint probability  $P(i, j|a, b, \lambda)$  of  $A$  and  $B$  obtaining the measurement result  $i$  and  $j$  with analyzer setting  $a$  and  $b$ , respectively with a certain dependence on the local hidden variable  $\lambda$ , can be expressed as the product of the individual measurement probabilities:

$$P(i, j|a, b, \lambda) = P(i|a, \lambda)P(j|b, \lambda). \quad (3.1)$$

Using Eq. 3.1, a correlation function  $E(a, b)$  taking into account any LHVs can be defined as:

$$E(a, b) = \int d\lambda f(\lambda)\bar{A}(a, \lambda)\bar{B}(b, \lambda), \quad (3.2)$$

where  $\bar{A}(a, \lambda)$  and  $\bar{B}(b, \lambda)$  are the average values of the measurement outcomes obtained by  $A$  and  $B$  with analyzer setting  $a$  and  $b$ , respectively. The function  $f(\lambda)$  is a probability density function that is dependent on the hidden variable  $\lambda$ .

For a Stern-Gerlach type measurement [54, 55] on a spin- $\frac{1}{2}$  particle, there are two possible outcomes;  $-\frac{\hbar}{2}$  and  $\frac{\hbar}{2}$ . These outcomes can be written as the basis states  $| -1 \rangle$  and  $| +1 \rangle$ , respectively. If we assign the value of -1 and +1 to the measurement result  $| -1 \rangle$  and  $| +1 \rangle$ , respectively<sup>2</sup>, the average values of the measurement outcomes obtained by Alice and Bob with their respective analyzer setting  $a$  and  $b$  can be written as:

$$\begin{aligned} \bar{A}(a, \lambda) &= P(1|a, \lambda) - P(-1|a, \lambda), \\ \bar{B}(b, \lambda) &= P(1|b, \lambda) - P(-1|b, \lambda), \end{aligned}$$

This will automatically imply that  $|\bar{A}(a, \lambda)| \leq 1$  and  $|\bar{B}(b, \lambda)| \leq 1$ . The difference and sum between the correlation function  $E(a, b)$  for different analyzer settings,  $a = a_i$  and  $b = b_i$  where  $i = 0, 1$ , are given by:

$$E(a_0, b_0) - E(a_0, b_1) = \int d\lambda f(\lambda)\bar{A}(a_0, \lambda)[\bar{B}(b_0, \lambda) - \bar{B}(b_1, \lambda)], \quad (3.3a)$$

$$E(a_1, b_0) + E(a_1, b_1) = \int d\lambda f(\lambda)\bar{A}(a_1, \lambda)[\bar{B}(b_0, \lambda) + \bar{B}(b_1, \lambda)], \quad (3.3b)$$

<sup>1</sup>Measurements made by  $A$  and  $B$  can also be said to be spacelike separated.

<sup>2</sup>Indeed any two outcome measurement, e.g. polarization, can be treated in a similar fashion.

Given that  $|\bar{A}(a, \lambda)| \leq 1$ , it is possible to rewrite Eq. 3.3a and Eq. 3.3b into the following inequalities:

$$|E(a_0, b_0) - E(a_0, b_1)| \leq \int d\lambda f(\lambda) |\bar{B}(b_0, \lambda) - \bar{B}(b_1, \lambda)|, \quad (3.4a)$$

$$|E(a_1, b_0) + E(a_1, b_1)| \leq \int d\lambda f(\lambda) |\bar{B}(b_0, \lambda) - \bar{B}(b_1, \lambda)|, \quad (3.4b)$$

Since  $|\bar{B}(b, \lambda)| \leq 1$ , using the triangle inequality relation<sup>3</sup>, we obtain:

$$|\bar{B}(b_0, \lambda) - \bar{B}(b_1, \lambda) + \bar{B}(b_0, \lambda) + \bar{B}(b_1, \lambda)| \leq 2, \quad (3.5)$$

Substituting Eq. 3.5 into the sum of Eq. 3.4a and Eq. 3.4b, we arrived at the CHSH Bell inequality [70], which can be written as  $|S| \leq 2$ , where the parameter  $S$  is a combination of correlations  $E(a_i, b_j)$  defined as:

$$S = E(a_0, b_0) - E(a_0, b_1) + E(a_1, b_0) + E(a_1, b_1). \quad (3.6)$$

In the quantum mechanical case, the correlations  $E(a_i, b_j)$  are defined from the joint probabilities  $P(a_i = +1, b_j = +1)$ ,  $P(a_i = +1, b_j = -1)$ , etc. as

$$\begin{aligned} E(a_i, b_j) &= P(a_i = +1, b_j = +1) - P(a_i = +1, b_j = -1) \\ &\quad - P(a_i = -1, b_j = +1) + P(a_i = -1, b_j = -1). \end{aligned} \quad (3.7)$$

Experimentally, with the fair sampling assumption, each  $E$  can be estimated from the statistical frequency of coincidence counts  $N$  between  $A$  and  $B$ ,

$$E = \frac{N_{++} - N_{+-} - N_{-+} + N_{--}}{N_{++} + N_{+-} + N_{-+} + N_{--}}. \quad (3.8)$$

For the maximally-entangled states in Eq. 2.8, using the expressions for the joint probability derived in Section 2.4, it can be shown that a maximum violation of  $S = 2\sqrt{2}$  is obtained for suitable choices of settings  $a$  and  $b$ .

In 1980, B. S. Cirel'son went on further to show that this violation of  $S = 2\sqrt{2} \approx 2.82843$  is a fundamental theoretical upper limit to quantum mechanical correlations. This came to be known as the Tsirelson's bound [4].

---

<sup>3</sup>The triangle inequality relation is defined as  $|x + y| \leq |x| + |y|$  where  $x$  and  $y$  are real numbers.

### 3.1 Implications of Approaching the Tsirelson's Bound

Tsirelson [4] showed that, according to quantum theory,  $S$  cannot be higher than  $2\sqrt{2} \approx 2.82843$ . This is Tsirelson's bound. Popescu and Rorlich [98] demonstrated that values up to  $S = 4$  were compatible with the no-signaling principle that prevents superluminal communication. This difference stimulated the search for principles singling out Tsirelson's bound as part of the effort towards understanding quantum theory from fundamental principles. So far, principles such as information causality [18], macroscopic locality [19] and exclusivity [20] have been identified that enforce Tsirelson's bound and principles such as non-signaling [98] and nontriviality of communication complexity [99, 100] that allow for higher values. Interestingly, there are also arguments predicting that Tsirelson's bound is not experimentally reachable.

One of them, due to Grinbaum [3], is particularly compelling because it addresses a possible defect of quantum theory, namely, the cut [1] between observer and observed system due to a lack of a clear definition of what is an observer in quantum theory [2]. The intention of Grinbaum in [3] is to fix this problem by integrating the observer into the theory. For that, Grinbaum introduces a mathematical framework based on algebraic coding theory [101] that provides a general model for communication and enables an information-theoretic definition of observer. This definition involves a limit on the complexity of the strings the observer can store and handle. These strings contain all descriptions of states allowed by quantum theory, but may also contain information not interpretable in terms of preparations and measurements. The language dynamics of these strings leads to a continuous model in the critical regime that, when restricted to measurements on bipartite systems in a three-dimensional Euclidean space, under the assumption that the number of strings with the same complexity after uncomputable Kolmogorov reordering is 6 and some assumptions on the mappings between certain metric spaces [3], and using the most precise determination available of a critical exponent in three-dimensional Ising conformal field theory [102], predicts that the violation of the Bell CHSH inequality is upper bounded by  $2.82537(2)$ . According to Grinbaum, "The Hilbert space formalism (of quantum theory), then, emerges from this mathematical approach as an effective description of a fundamental discrete theory of 'quantum' languages in the critical regime, somewhat similarly to the description of phase transitions by the effective Landau theory" [3].

Approaching the Tsirelson's bound by maximally violating the CHSH inequality may imply cryptographic security, even if the measurements that lead to the violation are unknown to the legitimate parties. This is the so-called "device-independent security" for key distribution protocols [103]. It can be proven that, under the assumption that the probability distributions are known without error, a necessary and sufficient condition for having

probability distributions which are necessarily independent of the measurement results of any eavesdropper is that the observed probabilities are exactly the quantum probability distributions reaching the Tsirelson's bound [21]. This result leads to a protocol for certifying device-independent security based on reaching the Tsirelson's bound [21].

Measurements leading to non-local correlations can be treated as black boxes which, given an input (the measurement setting), return an output (the measurement result). Interestingly, the observation of violations of the CHSH inequality and the assumption of non-signaling, allow the certification of a variety of physical properties *without making any assumptions or having any knowledge of the initial state or the inner working of the measurement devices*. For example, the value of the violation of the CHSH Bell inequality can be used to estimate the amount of quantum randomness produced by the black boxes [22]. The higher the violation, the larger the amount of certified randomness. Reaching the Tsirelson's bound can also be used to certify that the state being measured is equivalent to a maximally entangled state and that the measurements performed by each party are of the type represented in quantum theory by anti-commuting operators [104]. This may be adapted to practical methods to estimate the fidelity of the maximally entangled states; e.g. a CHSH violation larger than 2.81, certifies a singlet fidelity greater than 96% [24]. Moreover, saturating the Tsirelson's bound can be used to certify that a general quantum computation was actually performed [25].

## 3.2 Prior Work

The violation of Bell's inequality has been observed in many experiments with exceedingly high statistical significance. Many of these experiments are based on the generation of correlated photon pairs using cascade decays in atoms [5, 6], or exploiting non-linear optical processes [7–9, 16, 17]. Other successful demonstrations were based on internal degrees of freedom of ions [10–12] and neutral atoms [14], Josephson junctions [13], and nitrogen-vacancy centers in diamond [15]. Figure 3.1 summarizes the result obtained for the Bell parameter and the corresponding uncertainty of several experimental tests.

Interestingly, while continuous experimental progress has made it possible to approach Tsirelson's bound with decreasing uncertainty, predictions such as Grinbaum's, which would imply a radical departure from standard quantum theory are compatible with all existing results.

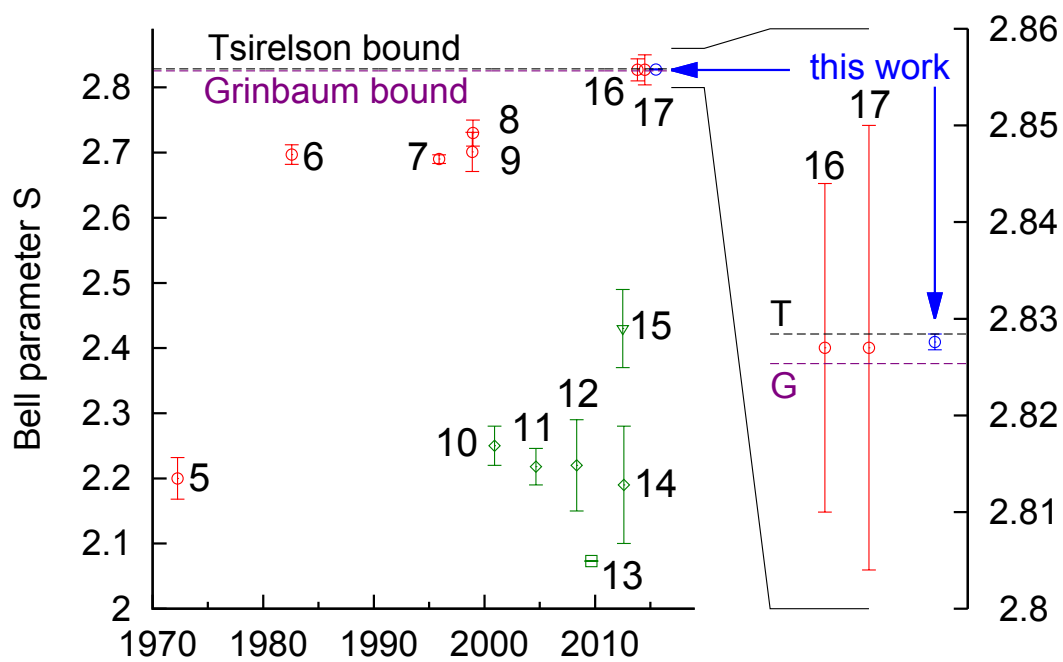


Fig. 3.1 Selected experimental tests of the CHSH Bell inequality with results close to the Tsirelson (T) and Grinbaum (G) bounds in photonic systems (circles), atoms and ions (diamonds), Josephson junctions (square), and nitrogen-vacancy centers in diamond (triangle). Numbers represent the references.

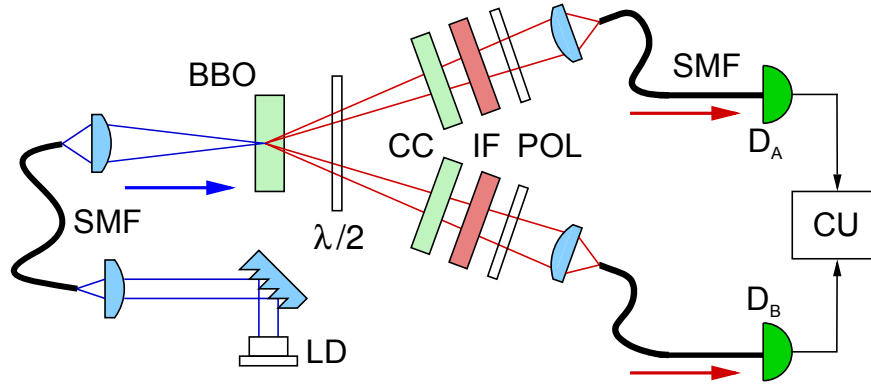


Fig. 3.2 Schematic of the experimental set-up. Polarization correlations of entangled-photon pairs are measured by film polarizers (POL) placed in front of the collection optics. All photons are detected by silicon avalanche photodetectors  $D_A$  and  $D_B$ , and registered in a coincidence unit (CU).

### 3.3 Experimental Implementation

Here, we report on an experiment with entangled photon pairs that pushes the uncertainty in the Bell parameter by another order of magnitude compared to previous experiments.

Our experiment follows the concept in [7] and is shown in Fig. 3.2. The output of a grating-stabilized laser diode (LD, central wavelength 405 nm) passes through a single mode optical fiber (SMF) for spatial mode filtering, and is focused to a beam waist of  $80 \mu\text{m}$  into a 2 mm thick BBO crystal.

In the crystal, cut for type-II phase-matching, spontaneous parametric down-conversion (SPDC) in a slightly non-collinear configuration generates photon pairs. Each down-converted pair consists of an ordinary and extraordinarily polarized photon, corresponding to horizontal (H) and vertical (V) in our setup. Two SMFs for 810 nm define two spatial modes, separated from either side of the pump beam by about  $3^\circ$ , are matched to the pump mode to optimize the collection [63]. A half-wave plate ( $\lambda/2$ ) and a pair of compensation crystals (CC) take care of the temporal and transversal walk-off [7], and allow the adjustment of the phase between the two decay components to obtain a singlet state  $|\Psi^-\rangle = 1/\sqrt{2}(|H\rangle_A|V\rangle_B - |V\rangle_A|H\rangle_B)$ .

Film polarizers (specified extinction ratio  $10^4$ ) perform the basis choice and polarization projection. Photons are detected by avalanche photo diodes (APDs, quantum efficiency  $\approx 40\%$ ), and corresponding detection events from the same pair identified by a coincidence unit (CU) if they arrive within  $\approx \pm 1.2 \text{ ns}$  of each other.

To arrive at a very clean singlet state, we carefully align the photon pair collection to balance the two photon pair contributions  $|HV\rangle$  and  $|VH\rangle$ , and adjust their relative phase with the CC. Furthermore, we minimize contributions from higher order parametric conversion processes [105] by restricting the pump power below 7 mW, leading to average detection rates of  $5016 \text{ s}^{-1}$  and  $4051 \text{ s}^{-1}$  at the two detectors (both uncorrected for dark counts), resulting in a detected photon pair rate of about  $567 \text{ s}^{-1}$ . The detectors exhibit dark count rates of  $91.7 \text{ s}^{-1}$  and  $106.2 \text{ s}^{-1}$ , respectively. This results in an accidental coincidence rate of  $0.0267 \pm 0.0047 \text{ s}^{-1}$ , determined by looking at coincidences in two time windows shifted by 10 ns and 25 ns from where the “true” coincidence were appearing.

We test the quality of polarization entanglement by measuring the polarization correlations in the  $\pm 45^\circ$  linear polarization basis. With interference filters (IF) of 5 nm bandwidth (FWHM) centered at 810 nm, we observe a visibility  $V_{45} = 99.9 \pm 0.1\%$ . The visibility in the natural H/V basis of the type-II down-conversion process also reaches  $V_{HV} = 99.9 \pm 0.1\%$ . This indicates a high quality of polarization entanglement; the uncertainties in the visibilities are obtained from propagated Poissonian counting statistics.

Due to imperfections in the state generation and errors in the setting of the polarizers, the setting  $\theta = 22.5^\circ$  may not yield the maximum possible violation. In order to observe the largest possible violation, and get as close as possible to the Tsirelson's bound, we optimized the angular settings of the polarizers.

The optimization starts by setting  $a = 0^\circ$ . This provides the initial reference axis and corresponds to  $a_0$ . Rotating  $b$  and recording the rate of coincidences, we identify the angles  $b'_0$  and  $b'_1$  that better match the expected correlation values. Setting  $b = b'_0$ , we repeat a similar procedure for  $a$ , obtaining  $a'_0$  and  $a'_1$ . This procedure converged to the resolution of the rotation motors (verified repeatability/resolution  $0.1^\circ$ ). For our experimental demonstration the optimal angles are  $a'_0 = 1.9^\circ$ ,  $b'_0 = 22.9^\circ$ ,  $a'_1 = 46.8^\circ$ , and  $b'_1 = 67.7^\circ$ . The deviation from the theoretically optimal angles can be attributed mainly to a systematic offset in the angular positions of the polarizers at the start of the measurement. The fact that the angular separation between the experiment are not at the theoretically optimal value of  $22.5^\circ$  could indicate a slight mismatch between the axes of the crystals and the defined  $H$  and  $V$  polarizations.

For evaluating how close we can come with the test of the CHSH Bell inequality to the Tsirelson's bound with a known uncertainty, we need to integrate for a sufficiently long time to acquire the necessary counting statistics, assuming we have the usual Poissonian statistics implied by the time invariance of our experiment. We collect coincidence events for each of the 16 settings required to evaluate  $S$  for 1 minute, and then repeat again the whole set. Within 312 such complete sets, we registered a total of 33,184,329 pair events. As a result,

we obtain in this experiment, via Eqs. (3.6) and (3.8), a value of  $S = 2.8276 \pm 0.00082$ , or a separation of  $2\sqrt{2} - S = 0.0008 \pm 0.00082$  from the Tsirelson's bound. The uncertainty is obtained only by propagating Poissonian counting statistics on the individual pair detections into the expression for  $S$ , as any systematical errors (attacks on detectors excluded [106], i.e., under the fair sampling assumption) would only lower the degree of violation.

So far we have worked under the assumption that Poissonian counting statistics is the sole contribution to the error in our experiment. However various other experimental conditions may also affect this error. First of such condition we will consider is the stability of the generated state. Fluctuations in the wavelength and intensity of the pump laser may affect the state being generated. The fluctuations in the state being generated will increase the spread of the value of  $S$  being evaluated. To quantify this contribution, we evaluated a series of values for  $S$  and the corresponding error  $\Delta S$  from a cumulative sum of the number of detected events for the 312 measurements by propagating the error from Poissonian counting statistics. The result of the obtained  $\Delta S$  versus the number of measurements accumulated is shown in Fig. 3.3. These errors are compared with those expected from a model of a maximally violation of  $|\Psi^-\rangle$  state for the same total counts. From the Fig. 3.3, it can be seen that the experimentally obtained error is in close agreement with model, giving us good confidence that the state is stable throughout the measurement run.

Another possible experimental condition that may contribute to the error is the presence of wedge errors within the polarizers. Wedge error results in the deviation of a beam as it passes through an optical element. For the polarizers where the orientation changes for different settings, wedge errors will induce setting dependence coupling efficiencies into the SMF for Alice and Bob, giving rise to non-uniform detection efficiencies for the different polarization. To assess this contribution, we first normalized the singles counts at Alice and Bob individually to their sum at every setting. This eliminates any fluctuation of the singles due to power fluctuations in the pump beam. The singles at Alice and Bob for settings  $a'_0$ ,  $a'_1$ , and  $b'_0$ ,  $b'_1$  and their orthogonal settings respectively are plotted against the number of measurements.

From Fig. 3.4, it can be seen that the detection efficiencies at each settings are different. The jumps in the plots are due to minute difference in the pump wavelength each time the laser goes out of lock with the wavemeter and is relocked. Evaluation of the value  $S$  for each of the 312 measurements reveals that these jumps have negligible impact on  $\Delta S$ . From the mean of the 8 traces we are able to calculate correction factor for each of settings. After applying the correction, we get a value of  $S = 2.8281 \pm 0.0031$ , indicating that wedge error in the polarizers are the major source of the residue deviation from  $2\sqrt{2}$

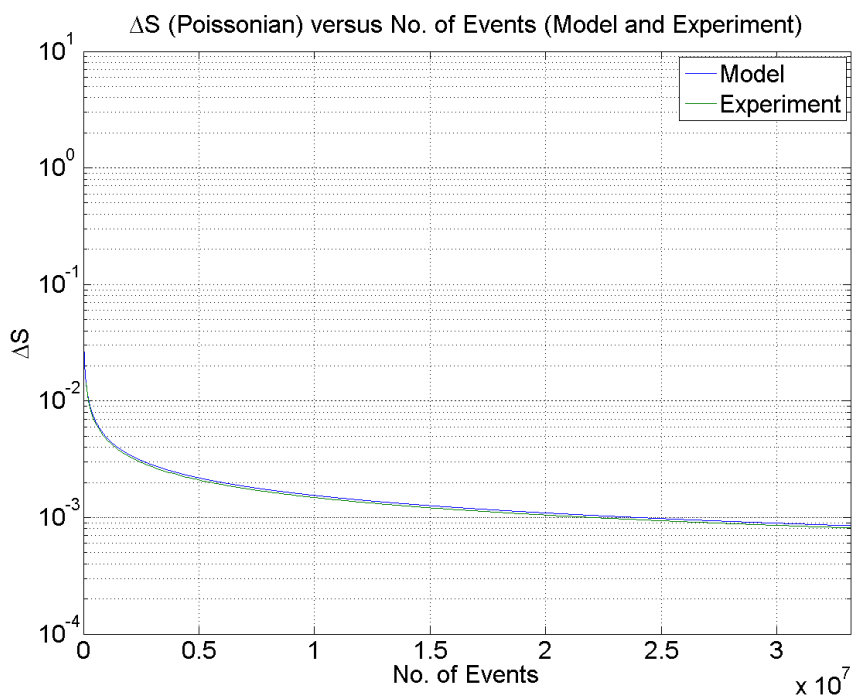


Fig. 3.3 A series of values for the error  $\Delta S$  are evaluated from a cumulative sum of the number detected events for the 312 measurements by propagating the error from Poissonian counting statistics. These errors are compared with those expected from a model of a maximally violation of  $|\Psi^-\rangle$  state for the same total counts. From the figure, it can be seen that the experimentally obtained error is in close agreement with model, giving us good confidence that the state is stable throughout the measurement.

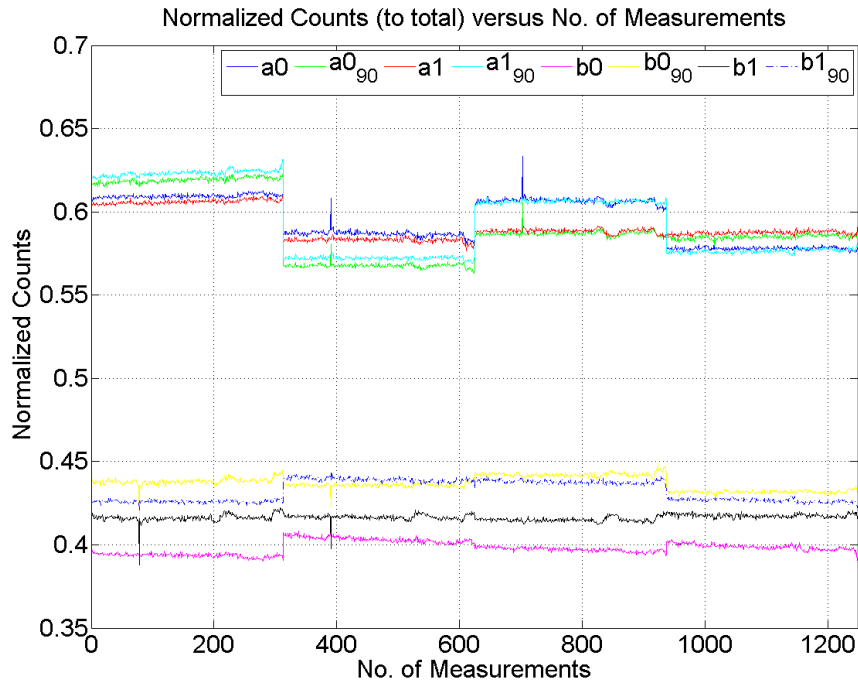


Fig. 3.4 To ascertain the effect of wedge errors of the polarizers on the final value of  $S$  obtained, we first normalized the singles counts at Alice and Bob individually to their sum at every settings to eliminate any effects on the singles due to power fluctuations in the pump beam. The singles for settings  $a'_0$ ,  $a'_1$ , and  $b'_0$ ,  $b'_1$  and their orthogonal settings respectively are plotted here against the number of measurement. The jumps in the plots are due to minute difference in the pump wavelength each time the laser goes out of lock with the wavemeter and is relocked. These are ascertain to have negligible impact on the spread of  $\Delta S$ . From the mean of the 8 traces we are able to calculate correction factor for each of settings. After applying the correction, we get a value of  $S = 2.8281 \pm 0.0031$ .

for our measurements. The error bound here is obtained by propagating the error from the Poissonian counting statistics for both the correction factor and the counted pairs.

### 3.4 Conclusions

The result of our experiment violates Grinbaum's bound by 2.72 standard deviations and constitutes the tightest experimental test of Tsirelson's bound ever reported. Therefore, it shows no evidence in favor of the thesis that quantum theory is only an effective version of a deeper theory and reinforces the thesis that quantum theory is fundamental and that the Tsirelson's bound is a natural limit that can be reached. This conclusion strengthens the potential value of those principles that predict Tsirelson's bound [18–20] for explaining the natural limits of correlations in all scenarios. The possibility of experimentally touching Tsirelson's bound as predicted by quantum theory also has important consequences for cryptographic security, since a necessary and sufficient condition for certifying probability distributions independent of the results of an eavesdropper in a device-independent scenario [103] is that the observed probabilities are exactly the ones corresponding to the Tsirelson's bound [21]. It is also important for the certification of a variety of physical properties based solely on the assumption of non-signaling (i.e. without making assumptions on the initial state of the system or the inner working of the measurement devices). In this respect, the degree of violation of the CHSH Bell inequality can be used to certify the amount of randomness [22]. The higher the violation, the larger the amount of certified randomness. Reaching the Tsirelson's bound can also be used to certify that the state being measured is a maximally entangled state and/or that the local measurements are of the type represented in quantum theory by anti-commuting operators [23]. This can be adapted to practical methods to estimate the fidelity of the maximally entangled states [24]. Finally, saturating the Tsirelson's bound can be used to certify that a general quantum computation was actually performed [25].

# Chapter 4

## Probing the Quantum-Classical Boundary with Compression Software

The idea that physical processes can be considered as computations done on some universal machines can be traced back to Turing and von Neumann [74], and the growth in computational power allowed the further development of these concepts. This resulted in a completely new approach to science in which the complexity of observed phenomena is closely related to the complexity of computational resources needed to simulate them [75]. In addition, there are physical phenomena that simply cannot be traced with analytical tools, which further motivated a computational approach to physics [107]. Moreover, the idea of quantum computation [108] led to a discovery of a few problems that seem not efficiently traceable on classical computers but can be done efficiently on a quantum version [51, 52].

Classical physics can be simulated on universal Turing machines or other computationally equivalent models [109]. On the other hand, efficient simulation of quantum systems requires a replacement of deterministic universal Turing machines with quantum computers whose states are non-classically correlated. Such machines can even simulate any local quantum system efficiently [110, 111]. Can we experimentally distinguish between these two descriptions of the universe using a logically self-contained computational approach?

In this chapter, we show that there are processes which cannot be simulated on local classical machines at all, independently of the available classical resources. We first introduce the notion of Kolmogorov complexity, a measure of the classical complexity of a phenomena, and later apply it to derive a bound on classical descriptions [26]. Next, we use the fact that Kolmogorov complexity can be approximated by compression algorithms [112]. We compress experimental data obtained from polarisation measurements on entangled photon pairs and show the violation of a classical bound.

## 4.1 Kolmogorov Complexity

Let's consider the description of a machine, whether classical or quantum, that outputs a string  $x$  made of 0's and 1's. In the case of a Turing machine  $U$ , we can always write a program  $\Lambda$  that generates  $x$ . The simplest such program is obviously 'PRINT  $x$ '. However, this is not optimal: in many cases the program can be much shorter than the string itself.

This brings us to the concept of Kolmogorov complexity  $K(x)$ , the minimal length  $l(\Lambda)$  of all programs  $\Lambda$  that reproduce a specific output  $x$ . If  $K(x)$  is of the order of the length of the output  $l(x)$  then our algorithmic description of  $x$  is inefficient and  $x$  is called algorithmically random [113]. In most cases  $K(x)$  cannot be computed [114]. To circumvent this issue, we can estimate the upper bounds for  $K(x)$  with some efficient lossless compression algorithm  $C(x)$  [112].

## 4.2 Simulation by Deterministic Universal Turing Machines

We now extend this picture by considering two Turing machines  $U_A$  (Alice) and  $U_B$  (Bob), which are spatially separated. If these machines cannot communicate, they generate two output strings that are independent, although the programs fed into the machines can be correlated. Moreover, the input programs are classical bit strings so the correlations between them must be classical.

We determine the complexity of the generated strings using the *Normalized Information Distance* (NID) [26]. This distance allows for a comparison of two data sets without detailed knowledge about their origin. In practice, we evaluate an approximation to the NID, the *Normalized Compression Distance* (NCD) [112], using a lossless compression software, in our case the LZMA Utilities (more on this in Section 4.4), based on the Lempel-Ziv-Markov chain algorithm [115].

We consider a model experiment, similar to the one we used for testing the Bell inequalities [69] in Section 3.3: a source emits pairs of photons that travel to two separate polarization analyzers  $M_A$  (Alice) and  $M_B$  (Bob). Each analyzer has two outputs associated with bit values 0 and 1, and can be set along directions  $a_0$  or  $a_1$  for  $M_A$ , and  $b_0$  or  $b_1$  for  $M_B$ . The record of the outputs from each analyzer forms a bit string (see Fig. 4.1).

The output  $x$  of each individual analyzer can be described as the output of a Turing machine  $U$ , fed with the settings  $a_j$  or  $b_k$  and a program  $\Lambda$ . The program will contain the information for generating the correct output for every detection event and for every setting.

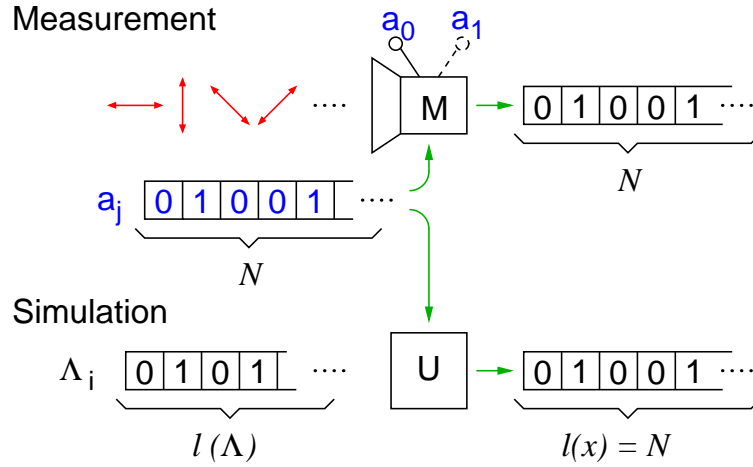


Fig. 4.1 Measurement:  $N$  particles enter a measuring device, characterized by two possible polarizer settings  $a_0$  and  $a_1$ , which generates a bit string of  $N$  measurement outcomes. Simulation: a universal Turing machine is fed with a program elements  $\Lambda_i$  and information about the chosen setting  $a_0$  or  $a_1$ . It delivers an output string of length  $N$ .

If we consider a string of finite length  $l(x) = N$ ,  $\Lambda$  will have to describe the  $4^N$  possible events. The length of the shortest  $\Lambda$  is equal to the Kolmogorov complexity of the generated string.

Next, we consider the simulation of the experiment with two local non-communicating machines  $U_A$  and  $U_B$  (see Fig. 4.2). We feed a program  $\Lambda$  to both of them and obtain two output strings,  $x$  and  $y$ , both of length  $N$ . In this case, the program has to describe the behavior of all  $2N$  events for all possible settings  $a_j$  and  $b_k$ , hence  $16^N$  possible events.

### 4.2.1 Normalized Information Distance

The Kolmogorov complexity of two bit strings  $K(x, y)$  is the length of the shortest program generating them simultaneously.  $K(x, y)$  can be shorter than  $K(x) + K(y)$  if  $x$  and  $y$  are correlated: the more correlated they are, the simpler it is to compute one string knowing the other. This idea was further carried out by Cilibrasi *et al.* [112] who constructed a distance measure between  $x$  and  $y$  called *Normalized Information Distance* (NID):

$$\text{NID}(x, y) = \frac{K(x, y) - \min\{K(x), K(y)\}}{\max\{K(x), K(y)\}}. \quad (4.1)$$

The NID obeys all required properties of a metric, in particular, the triangle inequality:

$$\text{NID}(x, y) + \text{NID}(y, z) \geq \text{NID}(x, z). \quad (4.2)$$

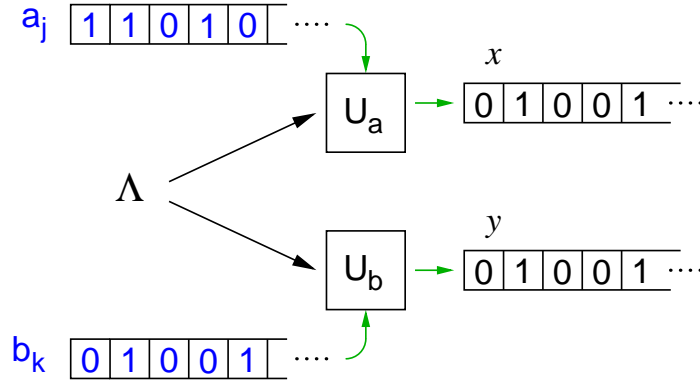


Fig. 4.2 Local classical machines simulating the generation of strings  $x$  and  $y$  by correlation measurements on an entangled state.

The above inequality holds up to a correction of order  $\log(l(x))$ , which can be neglected for sufficiently long strings [112].

## 4.2.2 Information Inequality

We consider the bit strings  $x_{a_j}$  and  $y_{b_k}$  generated by Alice and Bob with fixed setting  $a_j$  and  $b_k$ . Equation (4.2) then transforms into:

$$\text{NID}(x_{a_0}, y_{b_0}) + \text{NID}(y_{b_0}, y_{b_1}) \geq \text{NID}(x_{a_0}, y_{b_1}). \quad (4.3)$$

However,  $\text{NID}(y_{b_0}, y_{b_1})$  cannot be determined experimentally because the strings  $y_{b_0}$  and  $y_{b_1}$  come from measurements of incompatible observables. We therefore use the triangle inequality:

$$\text{NID}(x_{a_1}, y_{b_0}) + \text{NID}(x_{a_1}, y_{b_1}) \geq \text{NID}(y_{b_0}, y_{b_1}), \quad (4.4)$$

and combine it with inequality (4.3) to obtain a quadrangle inequality:

$$\text{NID}(x_{a_0}, y_{b_0}) + \text{NID}(x_{a_1}, y_{b_0}) + \text{NID}(x_{a_1}, y_{b_1}) \geq \text{NID}(x_{a_0}, y_{b_1}). \quad (4.5)$$

Similar to various tests of Bell inequalities, we introduce a scalar quantity  $S'$  that quantifies the degree of violation of Eq. (4.5)<sup>1,2</sup>:

$$\begin{aligned} S' = & \text{NID}(x_{a_0}, y_{b_1}) - \text{NID}(x_{a_0}, y_{b_0}) \\ & - \text{NID}(x_{a_1}, y_{b_0}) - \text{NID}(x_{a_1}, y_{b_1}) \leq 0 \end{aligned} \quad (4.6)$$

In order to experimentally test this inequality, we have to address the following problem. We can set up a source to generate entangled photon pairs in a state of our choosing, but we cannot control the nature of the measurement. For every experimental run  $i$  with the same preparation the resulting string  $x_{i,a_j}$  can be different. Consequently, the corresponding program  $\Lambda_i$  is different for every experimental run.

It is reasonable to assume that for every two experimental runs  $i$  and  $i'$  the complexity of the generated strings remains the same:  $K(x_{i,a_j}) = K(x_{i',a_j})$  and  $K(x_{i,a_j}, y_{i,b_k}) = K(x_{i',a_j}, y_{i',b_k})$ . Without these assumptions the same physical preparation of the experiment has different consequences and thus the notion of preparation loses its meaning. More generally, the predictive power of science can be expressed by saying that the same preparation results in the same complexity of observed phenomena. This assumption is analogous to the ensemble interpretation in quantum mechanics [116].

## 4.3 Estimation of Kolmogorov Complexity

In general the Kolmogorov complexity cannot be evaluated, but it can be estimated. One can adapt two conceptually different approaches.

### 4.3.1 Statistical Approach

This approach takes into account the ensemble of all possible  $N$ -bit strings and asks about their average Kolmogorov complexity. It can be shown that this average equals the Shannon entropy  $H(X)$  of the ensemble [114] and thus:

$$\langle \text{NID}(x, y) \rangle = \frac{H(x, y) - \min\{H(x), H(y)\}}{\max\{H(x), H(y)\}}. \quad (4.7)$$

<sup>1</sup>For the sake of completeness, we apply  $S'$  to the output of a PR box [104] given by  $x_{a_0} = y_{b_0}$ ,  $x_{a_1} = y_{b_0}$ ,  $x_{a_0} = y_{b_1}$ , and  $x_{a_1} = -y_{b_1}$ . The corresponding NID are then evaluated to be  $\text{NID}(x_{a_1}, y_{b_0}) = \text{NID}(x_{a_0}, y_{b_1}) = \text{NID}(x_{a_0}, y_{b_0}) = \text{NID}(x_{a_1}, -y_{b_1}) = 0$ , giving us  $S' = 0$ , which does not violate the inequality.

<sup>2</sup>Under the scenarios that the measurements are performed by Alice and Bob, this inequality has the same device independence as typical statistical based Bell's inequalities.

Inequality (Eq. 4.5) then becomes a type of entropic Bell inequality introduced by Braunstein *et al.* [117].

To evaluate the expected values for  $NID(x_a, y_b)$ , we assume the model that the bits that make up string  $x$  and  $y$  are obtained from the local measurements of coincidence events of photon pairs described by a maximally-entangled state  $|\psi^-\rangle$  (Eq. 2.8) with mapping of the outcomes of measurement with orthogonal polarizations for settings  $a$  and  $b$  to bit 0 or 1.

The entropy of each string obtained with a certain setting, e.g.  $H(x_a)$  with string length  $N$  and setting  $a$  is then given by:

$$\begin{aligned} H(x_a) &= -N \sum_{i=0,1} p_i(x_a) \log_2 p_i(x_a) \\ &= -N(p_0(x_a) \log_2 p_0(x_a) + (1 - p_0(x_a)) \log_2 (1 - p_0(x_a))), \end{aligned} \quad (4.8)$$

where  $p_{0,1}(x_a)$  gives the binomial distribution for the probability of obtaining bit 0 or 1 respectively, i.e.  $p_1 = 1 - p_0$ . The single photon density matrix, e.g.  $\rho_A$  describing the state that results from just considering events in Alice, can be expressed as a partial trace of the two-photon density matrix  $\rho_{AB} = |\psi^-\rangle\langle\psi^-|$  over one party, e.g. Bob for this situation. For the case of  $\rho_A$ , we obtain:

$$\begin{aligned} \rho_A &= Tr_B(\rho_{AB}), \\ &= \frac{1}{2}(|H\rangle\langle H| + |V\rangle\langle V|). \end{aligned}$$

The density matrix  $\rho_A$  describes a completely mixed state representing an unpolarized state. Measurement in any two orthogonal polarizations will yield equal probability of obtaining an outcome, i.e.  $p_i(x_a) = 1/2$ . Substituting this result into Eq. 4.8, we obtain the result that corresponds to the case of maximum local entropies:  $H(x_a) = H(y_b) = N$ .

The joint entropy of the two string  $H(x_a, y_b)$  is given by:  $H(x_a, y_b) = H(x_a|y_b) + H(x_a)$ , where  $H(x_a|y_b)$  is the conditional entropy of string  $y_b$  given  $x_a$ . The conditional entropy  $H(x_a|y_b)$  can be further expressed as:

$$H(x_a|y_b) = -N \sum_{i,j} p_{ij}(x_a, y_b) \log_2 \frac{p_i(x_a)}{p_{ij}(x_a, y_b)}, \quad (4.9)$$

where  $N$  here refers to the number of pairs,  $p_i(x_a) = 1/2$  as evaluated earlier and joint probability  $p_{ij}(x_a, y_b)$  can be evaluated from the derivation in Section 2.4. Substituting

Eq. 4.9 into Eq. 4.7, we arrive at:

$$\langle \text{NID}(x_a, y_b) \rangle = \sum_{i,j}^N p_{ij}(x_a, y_b) \log_2 \frac{1}{2p_{ij}(x_a, y_b)}. \quad (4.10)$$

Further simplification of the analysis can be done by appealing to the result shown in [117] that for a maximally-entangled polarization state of two photons and polarizer angles obeying the constraints:

$$\begin{aligned} \vec{a}_0 \cdot \vec{b}_1 &= \cos 3\theta, \\ \vec{a}_0 \cdot \vec{b}_0 &= \vec{a}_1 \cdot \vec{b}_0 = \vec{a}_1 \cdot \vec{b}_1 = \cos \theta, \end{aligned} \quad (4.11)$$

inequality (4.5) is violated for an appropriate range of  $\theta$ . Using this relation it is then possible to obtain the expected value of  $S'$  as a function of  $\theta$  (Fig. 4.6a). The maximal violation of this inequality is  $S' = 0.24$ , with a separation of  $\theta = 8.6^\circ$ .

### 4.3.2 Algorithmic approach

It is possible to avoid a statistical description of our experiment following the ideas pioneered in [112]. There, it was shown that the Kolmogorov complexity can be well approximated by the application of compression algorithms. This approximation introduces the new distance called *Normalized Compression Distance* (NCD):

$$\text{NCD}(x, y) = \frac{C(x, y) - \min\{C(x), C(y)\}}{\max\{C(x), C(y)\}}, \quad (4.12)$$

where  $C(x)$  is the length of the compressed string  $x$  and  $C(x, y)$  is the length of the compressed concatenated strings  $x, y$ . Replacing NID with NCD in Eq. (4.6) leads to a new inequality:

$$\begin{aligned} S' \rightarrow S &= \text{NCD}(x_{a_0}, y_{b_1}) - \text{NCD}(x_{a_0}, y_{b_0}) \\ &\quad - \text{NCD}(x_{a_1}, y_{b_0}) - \text{NCD}(x_{a_1}, y_{b_1}) \leq 0. \end{aligned} \quad (4.13)$$

This expression can be tested experimentally because the NCD distance measure is operationally defined.

To conduct an experiment we need to ensure the suitability of the compression software we use to evaluate the NCD. For this, we numerically simulate the outcome of an experiment based on a distribution of results predicted by quantum physics for the maximally-entangled

state  $|\psi^-\rangle$  (Eq. 2.8) using the derivation found in Section 2.4. Among the packages we tested, we found that the LZMA Utility [115] approaches the Shannon limit [118] most closely.

Most compression algorithms use some prediction about the data composition. If it matches this prediction, the compression can be done efficiently. Our experimental data fit the specifics of the LZMA Utility (refer to Section 4.4). In general our method can be used for data from any source by finding a suitable compression algorithm [112]. Thus, we are not limited to *independent identically distributed* (i.i.d.) sources, as it is commonly assumed in standard statistical ensemble-based experiments, like, for instance, Bell-type tests.

The simulation also verifies the angle that maximizes the violation (4.13). The results of the simulation are presented in Figure 4.6. More details on the generation of the simulated data and the choice of the compressor are covered next in Section 4.4.

## 4.4 Choice of Compressor

Before moving to the experiment, we need to ensure the suitability of the compression software we use to evaluate the NCD. For this, we numerically simulate the outcome of an experiment, based on a distribution of results predicted by quantum physics for the maximally-entangled state  $|\psi^-\rangle$  (steps for this derivation can be found in Section 2.4). The simulation also allows us to verify the angle that maximizes the violation of Eq. (4.13) predicted from Eq. (4.11).

In order to evaluate the NCDs of the binary strings, we need to choose a compression algorithm that performs close to the Shannon limit. This is necessary to ensure that it does not introduce any unintended artifacts that lead to an overestimation of the violation. Preferably we want to work in the regime where the obtained NCDs always underestimate the violation. For this purpose, we characterized four compression algorithms implemented by freely available compression programs: *lzma* [115], *gzip* [119], *gzip* [120], and *lzw* [121]. To eliminate the overhead associated with the compression of ASCII text files, we save data in a binary format.

For this characterization and simulation of the experiment, we need to generate a “random” string of bits (1, 0) or pairs of bits (00, 01, 10, and 11) of various length with various probability distributions. We generate these strings using the *MATLAB* [122] function *randsample()* that uses the pseudo random number generator *mt19937ar* with a long period of  $2^{19937} - 1$ . It is based on the Mersenne Twister [123], with *ziggurat* [124] as the algorithm that generates the required probability distribution. The complexity of this (deterministic) source of pseudorandom numbers should be high enough to *not* be captured as algorithmic.

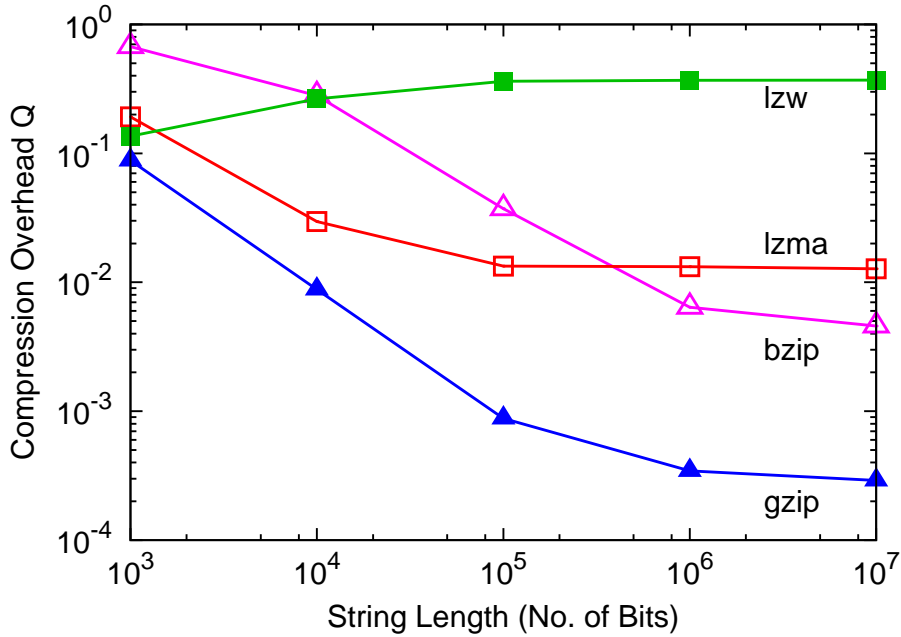


Fig. 4.3 Comparison of the compression overhead  $Q$  obtained using four different compression algorithms on pseudo-random strings of varying lengths. The expected value for an ideal compressor is 0. From this characterization we can exclude *lzw* as a useful compressor for our application.

The first part of this characterization involves establishing the minimum string length required for the compression algorithms to perform consistently. We start by generating binary strings,  $x$ , with equal probability of 1's and 0's, i.e. random strings, of varying length. For each  $x$ , we evaluate the compression overhead  $Q$  as:

$$Q = \frac{C(x) - H(x)}{l(x)}. \quad (4.14)$$

For a good compressor, we expect  $Q$  to be close to 0. From Fig. 4.3, it can be seen that for all the compressors,  $Q$  starts to converge after about  $10^5$  bits, setting the minimum string length required for the compressors to work consistently. The *lzw* compressor fails this test, converging to a  $Q$  of 0.37 for long string, while *bzip2*, *gzip*, and *lzma* give a  $Q$  below  $10^{-1}$ .

In the second part of this characterization, test the compressors with strings with a known amount of correlation. We generate a random string  $x$  of length  $10^7$  using the same technique already described. We then generate a second string  $y$  of equal length and with probability  $p$  of being correlated to  $x$ . For  $p = 0$ , the two strings are equal, i.e. perfectly correlated. For  $p = 0.5$ , they are uncorrelated.

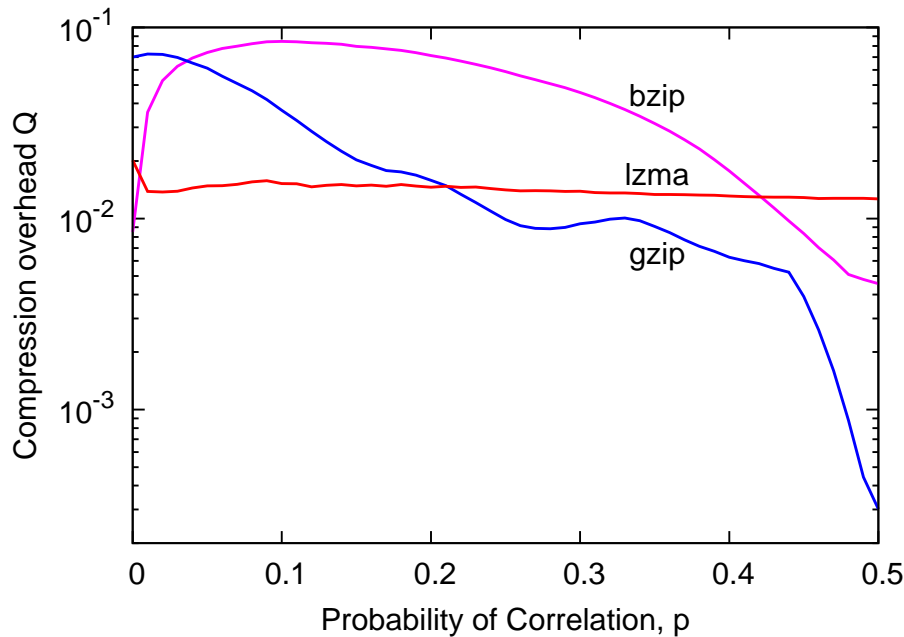


Fig. 4.4 Compression overhead  $Q$  for the string  $xy$  as a function of the probability of pairwise correlation  $p$  between the bits of the generating strings  $x$  and  $y$  for three different compressors: *bzip*, *gzip*, and *lzma*.

The two strings  $x$  and  $y$  are then combined to form the string  $xy$ : to avoid artifacts due to the limited data block size of the compression algorithms, the elements of  $x$  and  $y$  are interleaved. We then compress  $xy$  and evaluate the compression overhead  $Q$  as a function of  $p$ . The results for different compressors are shown in Fig. 4.4. Although there are ranges of  $p$  where *bzip* and *gzip* perform better than *lzma*, the latter shows a more uniform performance over the entire interval of  $p$ . It is reasonable to assume that the use of *lzma* should reduce the possibility of artifacts in the estimation of the NCD also for the data obtained from the experiment, giving us a lower bound for the violation.

Conceivably this kind of compressibility test can also be performed on the outputs from various random number generators, e.g. quantum number generators [125], to give some indication of their randomness especially in comparison with outputs from other sources. The only caveat here being that the expected period of these generators, if any, must be shorter than the size of memory block implemented in the compression software used for the test.

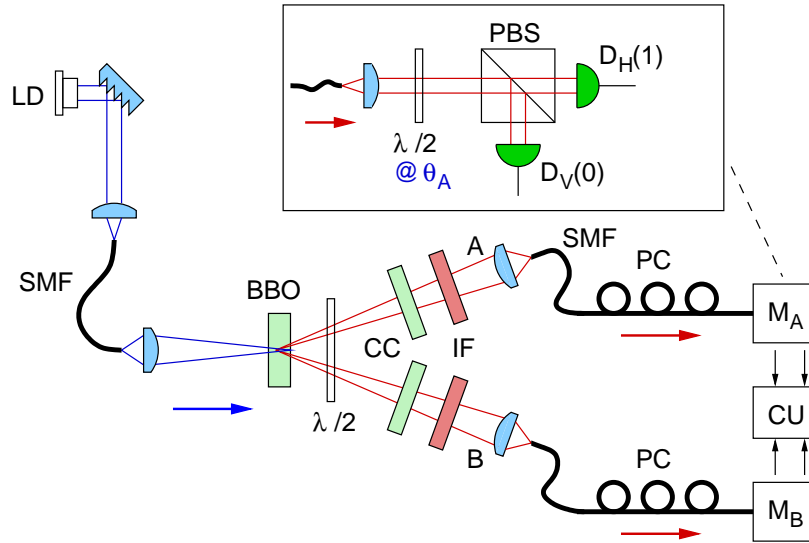


Fig. 4.5 Schematic of the experimental set-up. Polarization correlations of entangled-photon pairs are measured by the polarization analyzers  $M_A$  and  $M_B$ , each consisting of a half wave plate ( $\lambda/2$ ) followed by a polarization beam splitter (PBS). All photons are detected by Avalanche photodetectors  $D_H$  and  $D_V$ , and registered in a coincidence unit (CU).

## 4.5 Experiment Implementation

In our experiment (see Fig. 4.5), similar to that described in Section 3.3, the output of a grating-stabilized laser diode (LD, central wavelength 405 nm) passes through a single mode optical fiber (SMF) for spatial mode filtering, and is focused to a beam waist of  $80 \mu\text{m}$  into a 2 mm thick BBO crystal. In this crystal (cut for type-II phase-matching), photon pairs are generated via spontaneous parametric down-conversion (SPDC) in a slightly non-collinear configuration. A half-wave plate ( $\lambda/2$ ) and a pair of compensation crystals (CC) take care of the temporal and transversal walk-off [7].

Two spatial modes (labeled A and B) of down-converted light, defined by the SMFs for 810 nm, are matched to the pump mode to optimize the collection [63]. In type-II SPDC, each down-converted pair consists of an ordinary and extraordinarily polarized photon, corresponding to horizontal (H) and vertical (V) in our setup. A pair of polarization controllers (PCs) ensures that the stress-induced dispersion in the SMFs do not affect the polarization of the collected photons.

It is prudent to mention here that based on earlier work done in the group [126], these PCs typically still have unwanted dispersion remaining at the 1% level. Thus this places a constrain on the accuracy of state preparation and ultimately limits the quality of entanglement. This constrain was not present in the earlier experiment described in Chapter 3 as the

polarization analysis was done on the down-converted photons prior to being collected into the SMFs.

To arrive at an approximate singlet Bell state, the phase  $\phi$  between the two decay possibilities in the polarization state:

$$|\psi\rangle = \frac{1}{\sqrt{2}} \left( |H\rangle_A |V\rangle_B + e^{i\phi} |V\rangle_A |H\rangle_B \right), \quad (4.15)$$

is adjusted to  $\phi = \pi$  by tilting the CC.

In the experiment described in Section 3.3, the probability distribution of the four possible outcomes, i.e.  $P_{++}$ ,  $P_{+-}$ ,  $P_{-+}$ , and  $P_{--}$ , for various polarizer settings were evaluated. As we assumed the i.i.d. situation for the entangled pairs generated, it naturally follows that with the same integration time, the probability distribution of the measurement outcomes will remain constant. As a result, measurement of the four possible outcomes do not need to be performed simultaneously and the probability distribution can be obtained by normalizing the counts obtained for each outcome against the total number of coincidence events for all the outcomes.

This is in contrast to the current experiment where we rely on recording the the patterns of coincidence events and using them to build up binary strings for evaluation of the inequality  $S$ . Due to the continuous wave (CW) nature of the pump, the generation of the photon pairs occur at random times, thus there are no timing references that one can appeal to that indicate the time of generation of each photon pair. The absence of an detection event in one outcome thus does not imply there a detection event in another outcome. Due to this reason, all the outcomes need to be probed simultaneously. This is done in the polarization analyzers (Fig. 4.5), where the photons from SPDC are projected onto arbitrary linear polarization by  $\lambda/2$  plates, set to half of the analyzing angles  $\theta_{A(B)}$ , and polarization beam splitter (PBS) in each analyzer.

Photons are detected by avalanche photo diodes (APDs) and corresponding detection events from the same pair identified by a coincidence unit (CU) if they arrive within the coincidence time window,  $\tau_C \approx \pm 3$  ns, of each other. It is worthwhile to mention that  $\tau_C$  here has been increased from the previous value of 1.2 ns stated in Section 3.3. This was done to allow for a higher coincidence rate and thus a faster convergence to a long enough string length for the compressor to perform consistently. While it was established in Section 2.5 that increasing  $\tau_C$  would increase the rate of accidental coincidences thereby degrading the quality of polarization entanglement, the primary aim of this measurement was to demonstrate a violation of  $S$  (Eq. 4.13) and not necessarily to do so maximally.

The quality of polarization entanglement is tested by probing the polarization correlations in a basis complementary to the intrinsic HV basis of the crystal; for Bell states  $|\psi^\pm\rangle$ , strong polarization correlations are e.g. expected in a  $\pm 45^\circ$  linear polarization basis.

With interference filters (IF) of 5 nm bandwidth (FWHM) centered at 810 nm, we observe a visibility  $V_{45} = 99.9 \pm 0.1\%$ . The visibility in the natural H/V basis of the type-II down-conversion process also reaches  $V_{HV} = 99.9 \pm 0.1\%$ . A separate test of a CHSH-type Bell inequality [70], identical to that performed in Chapter 3, leads to a value of  $S = 2.826 \pm 0.0015$ . This indicates a relatively high quality of polarization entanglement; the uncertainties in the visibilities are obtained from propagated Poissonian counting statistics. The slight decrease in the value of  $S$  from that obtained in Chapter 3 can be attributed to the limitation in the accuracy of the entangled state preparation imposed by the PCs and an increase in the rate of accidental coincidences due the increased  $\tau_C$ .

We record two-fold coincidences of detection events between detectors at A and B. For each PBS, the transmitted output is associated with 0 and the reflected one with 1. The resulting binary strings  $x$  from A, and  $y$  from B are written into two individual binary files. From these, we calculate the NCD using Eq. (4.12). This procedure is repeated for each of the four settings  $(a_0, b_0)$ ,  $(a_1, b_0)$ ,  $(a_1, b_1)$ , and  $(a_0, b_1)$  in order to obtain the value for  $S$ .

## 4.6 Symmetrization of detector efficiencies

The experimental setup (Fig. 4.5) uses four APDs:  $D_{HA}$ ,  $D_{VA}$  (Alice), and  $D_{HB}$ ,  $D_{VB}$  (Bob) to register photon pair events in the two spatial modes. By denoting events at  $D_H$  and  $D_V$  as 1 and 0, the four possible output patterns are 00, 01, 10, and 11, where the least and most significant bit corresponds to the Alice and Bob mode, respectively. Due to differences in the the losses in the transmitted and reflected port of the PBS, efficiencies in coupling light into the APDs, and the quantum efficiencies of APDs, the detection efficiencies for the four output combinations are different. The resulting effective pair efficiencies are then given by the product of the contributing detection efficiencies  $\eta_{VB}$ ,  $\eta_{HB}$ ,  $\eta_{VA}$ , and  $\eta_{HA}$ .

This asymmetry will skew the statistics of the measurement results. We symmetrize the effective pair efficiencies for each  $(\theta_A, \theta_B)$  measuring also the following settings:  $(\theta_A + 45^\circ, \theta_B)$ ,  $(\theta_A, \theta_B + 45^\circ)$ , and  $(\theta_A + 45^\circ, \theta_B + 45^\circ)$ . This procedure swaps the output ports of the PBS at which each polarization state is detected. The resulting outcomes are then interleaved, providing an uniform detection probability for the four possible outcomes. The effective pair detection efficiency for all four combinations is then  $(\eta_{VB}\eta_{VA} + \eta_{VB}\eta_{HA} + \eta_{HB}\eta_{VA} + \eta_{HB}\eta_{HA})/4$ .

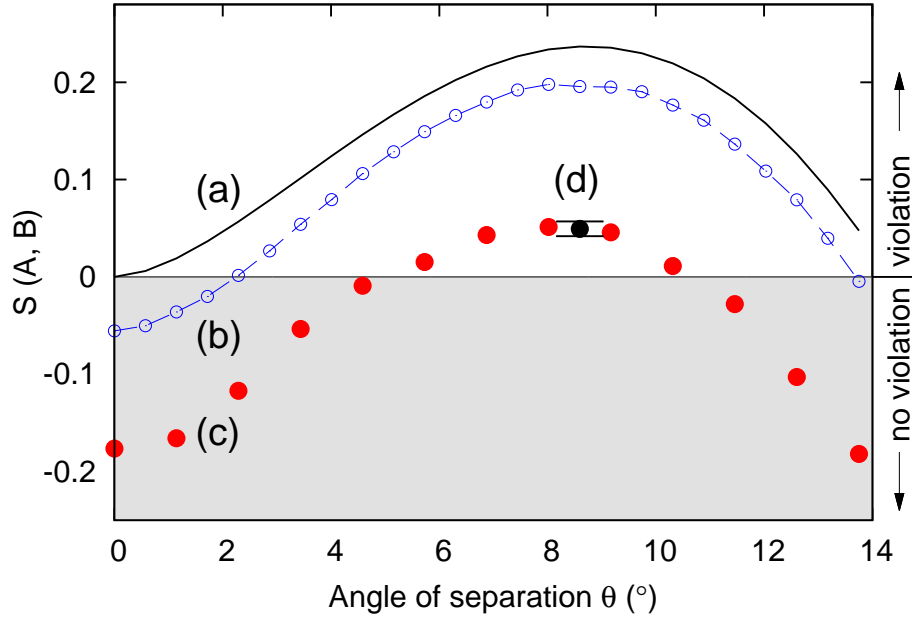


Fig. 4.6 Plots of  $S$  versus angle of separation  $\theta$ . (a) Result obtained from Eq. (4.7) (b) result obtained from using the LZMA compressor on a simulated data ensemble, (c) measurement of  $S$  in the experiment shown in Fig. 4.5, and (d) longer measurement at the optimal angle  $\theta = 8.6^\circ$ .

## 4.7 Results

The inequality is experimentally tested by evaluating  $S$  in Eq. (4.13) for a range of  $\theta$ ; the obtained values [points (c), (d) in Fig. 4.6] are consistently lower than the trace (a) calculated via entropy using Eq. (4.7) and than a simulation with the same compressor (b). This is because the LZMA Utility is not working exactly at the Shannon limit and also due to imperfect state generation and detection.

As a consequence of Eq. (4.11), we expect the maximal violation for  $\theta = 8.6^\circ$ . For this particular angle we collected results from a large number of photon pairs. Although we set out in this work to avoid a statistical argument in the interpretation of measurement results, we do resort to statistical techniques to assess the confidence in an experimental finding of a violation of inequality Eq. (4.13). To estimate an uncertainty of the experimentally obtained values for  $S$ , this large data set was subdivided into files with length greater than  $10^5$  bits. The results from all the subdivided files are then averaged to obtain the final result of  $S(\theta = 8.6^\circ) = 0.0494 \pm 0.0076$ , with the latter indicating a relatively small standard deviation over these different subsets.

## 4.8 Conclusion

There is a trend to look at physical systems and processes as programs run on a computer made of the constituents of our universe. We could show that this is not possible if one uses a computation paradigm of a local deterministic Turing machine. Although this has been already extensively researched in quantum information theory, we present a complementary algorithmic approach for an explicit, experimentally testable example. This algorithmic approach is complementary to the orthodox Bell inequality approach to quantum nonlocality [69] that is statistical in its nature.

Any process that can be simulated on a local universal Turing machine can be encoded as a program that is fed into it. For every such a program there exists its shortest description called Kolmogorov complexity, which in most of the cases can only be approximated using compression software. Moreover, such a description must obey distance properties as shown in [26, 112]. By testing Eq. 4.13, we showed that this is unattainable in the specific case of polarization-entangled photon pairs. Therefore, there exist physical processes that cannot be simulated on local universal Turing machines.

There are two fundamentally different notions of complexity in computer science. On one hand, computational complexity, mainly researched on in quantum information science, studies how much resources are needed to solve a computational problem. These studies focus on complexity classes such as P, NP [127] and its main concern is, given an input program, how efficiently it can be computed. On the other hand, algorithmic complexity deals with a problem of what the most efficient encoding of an input program is. This complementary problem to computation complexity has not yet received enough attention in quantum information science and it would require a further work on quantum version of Kolmogorov complexity [128].

We would like to stress that our analysis of the experimental data is purely and consistently algorithmic. We do not resort to statistical methods that are alien to the concept of computation. If this approach can be extended to all quantum experiments, it would allow us to bypass the commonly used statistical interpretation of quantum theory.

At the same time we believe that this approach can also serve to complement typical probability based Bell's inequalities. One thing to note is that since the same assumptions, e.g. detection loophole, fair sampling, and freedom of choice, goes into it's evaluation, the approach will probably be susceptible to the same set of loopholes as with any other Bell's inequalities. The use of real compressors in our evaluation just lowers the violation and does not open up any other new loopholes. That being said, this is still a topic for further in depth studies.



## Chapter 5

# Generation of Energy-Time Entangled Photons and Higher Dimensional States

In the experiment described in Chapter 3 and 4, we employed the polarization degree of freedom of correlated photon pairs generated by spontaneous parametric down-conversion (SPDC) to encode the maximally entangled state,  $|\psi^-\rangle$  (Eq. 2.8), for use in our measurements. These polarization-entangled qubit pairs can be implemented experimentally [7, 62, 63, 93] with relative ease, i.e. the down-conversion setup also serves to generate polarization entanglement, as the polarization correlations between the photons in each pair is a natural consequence of the phase-matching conditions (Eq. 2.3) obeyed by the SPDC process. These polarization qubits are often used in free space optical links for various quantum key distribution (QKD) [129, 130] and quantum communication [131, 132] experiments.

Two major limitations of such free space optical links are that they require direct lines of sight and that the quality of the transmission channel is strongly affected by atmospheric attenuations and turbulences [133]. Such limitations can be overcome by implementation of these links in optical fibers instead. The use of optical fibers for QKD is further advantaged when one considers the situation where the comprehensive fiber optics network currently in place for telecommunication purposes can also serve as ready infrastructures for experimentation [134–136] and conceivably its eventual commercialization.

However, the use of optical fibers in such optical links, like in the case for free space, is not without its problems. One of such problems is while the glass or plastic used in the core of these optical fibers is naturally isotropic, inhomogeneous mechanical stresses applied on the fibers can induce birefringence [137], which in turn affects the polarisation mode of the light traveling through it. This non-preservation of the polarization of the light passing through the fibers may render some QKD protocols impossible. For short length of fibers changes in polarization are relatively stable and can be compensated using

polarization controllers [138] (used in the experimental setup described in Chapter 3 and 4). For long length of optical fibers, due to the random mechanical and thermal stresses on the fibers, active compensation of the polarization changes may not always be possible. Thus the use of polarization qubits is not very suited for this purpose.

A more suitable degree of freedom for this purpose is that of energy-time. This degree of freedom has its origin in an experiment, proposed by Franson in 1989 [39], involving the preparation of an energy-time entangled state using three-level atoms with unbalanced Mach-Zehnder interferometers [139, 140] in each of the photon paths (Fig. 5.1) for analysis. The term energy-time here refers to the energy-time uncertainty relation [141]. The highest and lowest state of the three-level atomic system have long emission lifetimes and it is separated by an intermediate state with a comparatively short lifetime. Due to the uncertainty of the emission time of the photons brought about by the long lifetime of the highest state, the total energy of the two photons emitted can be determined with great precision. However, the short intermediate lifetime means that upon detecting one photon, the other can be very precisely localized temporally, making the determination of its energy uncertain.

This situation mirrored the discussion about the problem of position-momentum entanglement in the original EPR experiment [68]. With quantum mechanical considerations, J. D. Franson predicted that by simultaneously monitoring the coincidence events between detector  $D_1$  and  $D_2$  (Fig. 5.1), and scanning the phases of the interferometers, one would observe a sinusoidally oscillation of the coincidence signal, something that is not possible in a classical context. In 1990, Ou *et al.* [142] demonstrated energy-time entanglement successfully using photon pairs generated from SPDC. As the energy-time degree of freedom deals only with the measurement of the arrival times of photons, it is not affected by birefringence, thus making it a suitable candidate for the encoding qubits for transmission through optical fibers.

Going a step further, there are experiments, e.g. reference frame independent QKD [143–145] and the experimental violation of higher dimensional Bell's inequality [49], that require entangled states with dimensionality more than the entangled state that we present in Chapter 3 and 4. One way to expand this dimensionality is to increase the number of qubits by entangling a greater number of particles [146]. However, this may be complicated and resource intensive. Another way is to 'combine' different degrees of freedom to achieve a state with a higher dimensionality. The resulting state is called a hyperentangled state [77, 147]. This is possible due to the fact that each physical carrier, in our case the photon, has multiple degrees of freedom on which qubits can be encoded. Thus essentially, each photon can be encoded with more than one qubit.

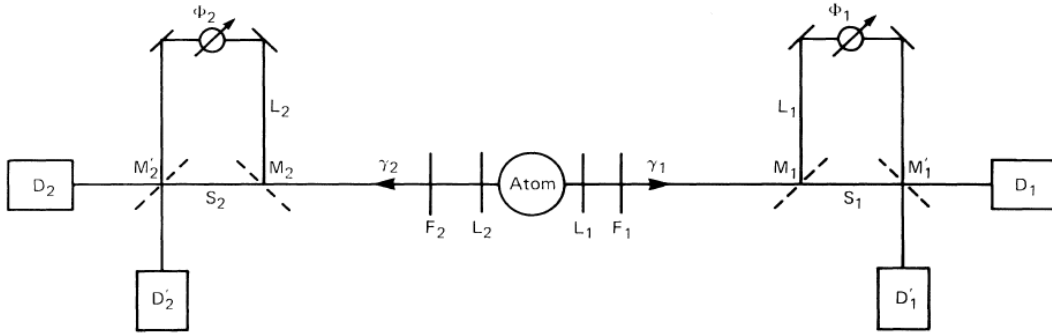


Fig. 5.1 Schematic of experiment proposed by Franson in 1989. Wavelength-correlated photons,  $\gamma_1$  and  $\gamma_2$ , generated by spontaneous decay from the excited state of a three-level atomic system passes through an unbalanced Mach-Zehnder interferometers on each path. Photon coincidence measurements of the interference between the amplitudes along the shorter paths,  $S_1$  and  $S_2$ , and the longer paths,  $L_1$  and  $L_2$  for various phase setting of  $\phi_1$  and  $\phi_2$  were taken (Figure adapted from [39]).

In this chapter, we will first cover, in Section 5.1 the generation of energy-time entangled photons using the process of SPDC. This is followed by a detailed discussion of the experimental parameters required in the generation. We then highlight the theoretical background of how such energy-time entangled state can be characterized in Section 5.2. Lastly, in Section 5.3, we will present ways of increasing the dimensionality of quantum systems and examining in-depth into how the same can be achieved by combining the polarization and the energy-time degree of freedom to form a hyperentangled state.

## 5.1 Generation of Energy-Time Entanglement

The first idea for energy-time entanglement originated from an experiment (Fig. 5.1) proposed by Franson in 1989 [39]. The proposed experiment calls for photon pairs to be created in an atomic decay process in a three-level system. This proposal was later implemented experimentally by Ou *et al.* [142] but using SPDC instead for the generation of the photon pairs. The schematic of an experimental setup, functionally similar to that implemented by Ou *et al.*, is found in Fig. 5.2. The photon pairs generated by SPDC<sup>1</sup> are analyzed by an unbalanced Mach-Zehnder interferometer in each of the Alice (*A*) and Bob (*B*) path of the

<sup>1</sup>It should be noted that the SPDC process here is only required to generate wavelength degenerate photon pairs. The polarization degree of freedom is not resolved in this experiment and thus the alignment to get the two decay paths of  $|H\rangle_A|V\rangle_B$  and  $|V\rangle_A|H\rangle_B$ , as indicated in Section 2.3, is not necessary.

down-conversion. For the generation of energy-time entangled photons, a few conditions must be satisfied:

1. *The path-length difference  $\Delta L$  within the A and B interferometers must be longer than the coherence length  $l_{C_{dc}}$  of the down-converted photons:* This condition ensures there is no single photon interference [148] of the down-converted photons in the interferometers.
2. *The time difference,  $\Delta T = \frac{\Delta L}{c}$ , where  $c$  is the speed of light, must be greater than the coincidence time window  $\tau_C$ :* We first consider all the possible paths the pairs of down-converted photon can take through the two interferometers to reach detector  $D_A$  and  $D_B$ . The states of the four possible paths are given by  $|s\rangle_A|l\rangle_B$ ,  $|l\rangle_A|s\rangle_B$ ,  $|s\rangle_A|s\rangle_B$ , and  $|l\rangle_A|l\rangle_B$ , where  $s$  and  $l$  represent the short and long path of the interferometers respectively. Considering  $t_A - t_B$ , the arrival time of a photon at  $D_A$  with respect to  $D_B$  (Fig. 5.2a), we obtain the time difference of  $-\Delta T$  and  $\Delta T$  for the combination  $|s\rangle_A|l\rangle_B$  and  $|l\rangle_A|s\rangle_B$  respectively. For the combination  $|s\rangle_A|s\rangle_B$ , and  $|l\rangle_A|l\rangle_B$ , there is no difference in arrival time, i.e.  $t_A - t_B = 0$ , assuming that the two interferometers are identical.

If we plot the probability of obtaining a coincidence event between  $D_A$  and  $D_B$  versus  $t_A - t_B$ , we obtain Fig. 5.3. The width of the peaks, given by the convolution of the two single photon temporal profiles of the down-converted photons in the pairs, provides a sort of two-photon coherence time. As explained in Section 2.3, two indistinguishable decay paths are needed for entanglement and from Fig. 5.3, it is clear that this condition is only satisfied for the central peak. Thus to only post-select the central peak, the coincidence time window  $\tau_C$  must also be less than  $\Delta T$ .

It is noteworthy to mention that as this is an interferometric measurement, it is highly susceptible to stability issues due to mechanical disturbances, e.g. acoustic vibrations and thermally induced length changes of structure of the interferometers. Often the longer the path-length difference  $\Delta L$ , the more pronounced is the stability issue, shortening the characteristic stable time of the interferometers. Thus as a matter of practical consideration,  $\Delta L$  is chosen to be as short as possible such that the adjacent peaks do not overlap. This minimum  $\Delta L$  is thus limited by the coherence length of the down-converted photons  $l_{C_{dc}}$  and the size of the of the coincidence time window  $\tau_C$ .

3. *The coherence length  $l_{C_p}$  of the pump light must be greater than the path-length difference  $\Delta L$  in each of the interferometers:* This is to ensure there is coherence between the short path  $|s\rangle$  and long path  $|l\rangle$  of the interferometers.

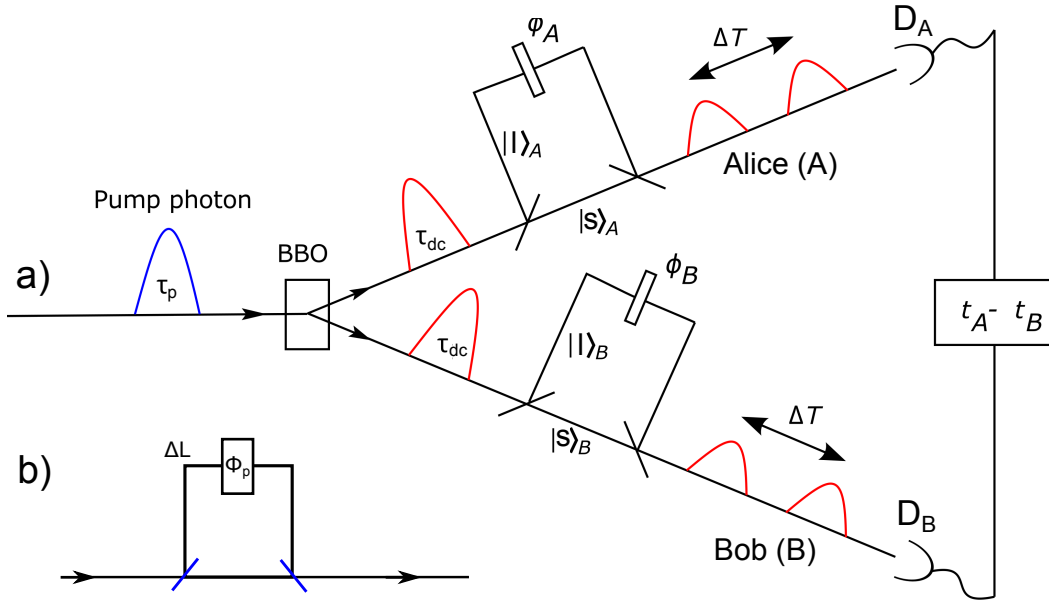


Fig. 5.2 a) Experimental setup for the preparation of energy-time entangled photon pairs. A pump photon with coherence time  $\tau_p$  is down-converted into correlated photon pairs with coherence time  $\tau_{dc}$ . The photon pairs are sent into Mach-Zehnder interferometers which introduces a time delay  $\Delta T$  due to the unbalanced arm lengths (short path  $|s\rangle$  and long path  $|l\rangle$ ). The condition  $\Delta T < \tau_2$  guarantees the coherent superposition of the photon pairs which take the short path  $|s\rangle$  or long path  $|l\rangle$  in the interferometers. The Franson interference [39] or second order correlation between the photon pairs are measured by silicon avalanche photodiodes (APD), with a time delay  $t_A - t_B$  between  $D_A$  and  $D_B$ . b) For the generation of time-bin entanglement, the pump is operated in a pulsed regime, with an inclusion of an unbalanced Mach-Zehnder interferometer in the path of the pump.

4. *The path-length difference  $\Delta L$  in the A and B interferometer should be identical or within the coherence length of the down-converted photons  $l_{dc}$  of each other:* This is to ensure there is biphoton interference of the two states  $|s\rangle_A |s\rangle_B$ , and  $|l\rangle_A |l\rangle_B$ .

These four constraints thus determine the geometries and dimensions of the experimental setup.

It is prudent to highlight here, the essential difference between energy-time and time-bin entanglement [61, 149]. In time-bin entanglement (Fig. 5.2b), the pump is operated in a pulsed regime as opposed to a continuous wave (CW) regime for energy-time entanglement. These pulses, generated from a mode-locked femtosecond laser for example, are in general not coherent with each other. Due to the broadband nature of these short optical pulses,

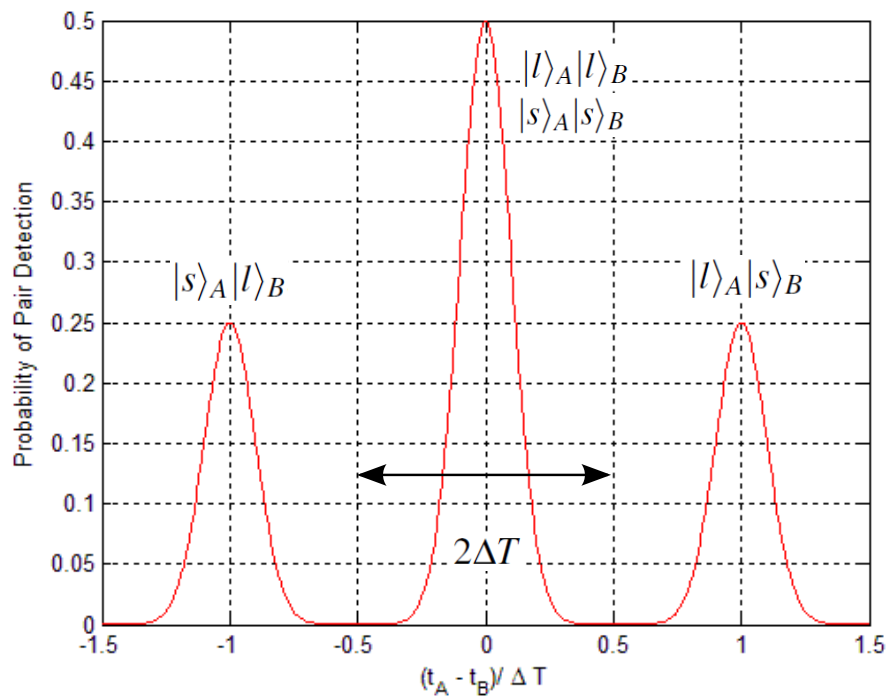


Fig. 5.3 Four possible amplitudes of the photon pairs in the time delay basis. The two coherent states  $|s\rangle_A |s\rangle_B$  and  $|l\rangle_A |l\rangle_B$  overlap up to the coherence length of the down-converted photon pairs and there is no single photon interference under the condition where the coherence length of the down-converted photons are less than that introduced by the unbalanced Mach-Zehnder interferometer,  $l_{Cdc} < \Delta L$ .

the short coherence length  $l_{C_p}$  of the pump light would not be able to satisfy the previously mentioned listed 3rd condition.

To restore the coherence between the early and late pulses, another interferometer is introduced into the path of the pump light. Introducing an additional unbalanced Mach-Zehnder interferometer in the pump beam splits the pulse train into a fixed delay  $\Delta T$ . Thus, the successive pulses are now indistinguishable from the preceding pulses which were generated  $\Delta T$  earlier. The states of the photon pairs  $|s\rangle_A|s\rangle_B$  and  $|l\rangle_A|l\rangle_B$  generated from SPDC are also now indistinguishable.

The phase  $\phi_p$  of the pump interferometer between and  $s$  and  $l$  path can be adjusted by changing the path-length difference. The path-length difference in the pump interferometer in this case must also be matched by the two Mach-Zehnder interferometers used for analysis for proper post-selection. In such a configuration, the entangled photon pairs will have well-defined emission times in contrast to the energy-time case. The resulting entangled state is given by:

$$|\phi\rangle_t = \frac{1}{\sqrt{2}} \left( |s\rangle_A|s\rangle_B + e^{i(\phi_A + \phi_B + \phi_p)} |l\rangle_A|l\rangle_B \right), \quad (5.1)$$

where  $\phi_{A,B}$  is the relative phase between the  $|s\rangle$  and  $|l\rangle$  path in  $A$  and  $B$  (Fig. 5.2).

The corresponding  $\phi_p$  for energy-time entanglement, where a CW pump is used, is given by the relative phase difference of the light from two points in the pump beam separated by  $\Delta L$ , the path-length difference of the analyzer interferometers. Since this phase  $\phi_p$  cannot be adjusted directly, it is offset by combining it with one of the phases of the analyzer interferometers, i.e.  $\phi'_a = \phi_a + \phi_p$ .

It is illuminating to think of the time-bin case as a special case of energy-time entanglement. The CW pump is coherent between any two points separated by the coherence length  $l_{C_p}$  or less. In the context of a pulsed pump, this can be seen as a continuum of pump interferometers with various path-length differences. The analyzer interferometers just post-select the case corresponding to a path-length difference  $\Delta L$ .

For our experiment in the coming chapter, we have opted for the implementation of the energy-time entanglement. This decision was prompted by our previous experiences with wavelength stability issues with our femtosecond pulsed laser in earlier work [90, 150, 151].

## 5.2 Characterization of Energy-Time Entangled Photon Pairs

Similar to the measurement of visibility for the polarization correlation described Section 2.5, the quality of energy-time correlation is determined by measuring the joint detection prob-

ability of the photon pairs while varying the phases  $\phi_A$  or  $\phi_B$  in one of the interferometers (Fig. 5.2a) and evaluating the visibility of the interference known as Franson interference [39]. The visibility is determined both by how well the  $s$  and  $l$  spatial mode overlaps within each interferometer and the overlap of between spatial mode  $A$  and  $B$ .

To obtain the expected result for the case of perfect overlap in both cases, we start by considering the field amplitude at detector  $D_A$  and  $D_B$  which can be written as:

$$\psi(\mathbf{r}_j, t) = \frac{1}{2}\psi_0(\mathbf{r}_j, t) + \frac{1}{2}e^{i\phi_{A,B}}\psi_0(\mathbf{r}_j, t - \Delta T).$$

where  $j = A, B$ , respectively. The field amplitudes  $\psi_0(\mathbf{r}_j, t)$  and  $\psi_0(\mathbf{r}_j, t - \Delta T)$  are the field amplitude due to the  $s$  and  $l$  path respectively at the detectors. If we consider only cases where both down-converted photons take the short path  $s$ . The coincidence function  $R$  between  $D_A$  and  $D_B$  is given by:

$$R = \langle s | \psi^\dagger(\mathbf{r}_A, t) \psi^\dagger(\mathbf{r}_B, t) \psi(\mathbf{r}_A, t) \psi(\mathbf{r}_B, t) | s \rangle,$$

which then expands to<sup>2</sup>:

$$R = \frac{1}{16} \langle s | [ \psi_0^\dagger(\mathbf{r}_A, t) \psi_0^\dagger(\mathbf{r}_B, t) + e^{-i(\phi_A + \phi_B)} \psi_0^\dagger(\mathbf{r}_A, t - \Delta T) \psi_0^\dagger(\mathbf{r}_B, t - \Delta T) ] \times [ \psi_0(\mathbf{r}_A, t) \psi_0(\mathbf{r}_B, t) + e^{i(\phi_A + \phi_B)} \psi_0(\mathbf{r}_A, t - \Delta T) \psi_0(\mathbf{r}_B, t - \Delta T) ] | s \rangle. \quad (5.2)$$

The conservation of energy requires that:

$$\omega_p + \Delta\omega = \omega_s + \omega_i,$$

where  $\omega_{s,i}$  are the frequencies of the signal and idler of the down-converted light (assumed to be identical for the wavelength degenerate case),  $\omega_p$  is the frequency of the pump, and  $\Delta\omega$  is the uncertainty of the pump frequency. We then write:

$$\psi_0(\mathbf{r}_A, t - \Delta T) \psi_0(\mathbf{r}_B, t - \Delta T) = e^{i(\omega_p + \Delta\omega)\Delta T} \psi_0(\mathbf{r}_A, t) \psi_0(\mathbf{r}_B, t).$$

---

<sup>2</sup>The case where both down-converted photons take the long path will be similar to the case shown here.

Assuming  $\Delta\omega\Delta T \ll 1$  and neglecting the contribution from this term, the coincidence function  $R$  (Eq. 5.2) can be written as:

$$\begin{aligned} R &\propto \left[ 1 + e^{-i(\omega_p\Delta T + \phi_A + \phi_B)} \right] \left[ 1 + e^{i(\omega_p\Delta T + \phi_A + \phi_B)} \right] \\ &\propto \cos^2 \left( \frac{\omega_p\Delta T + \phi_A + \phi_B}{2} \right). \end{aligned} \quad (5.3)$$

The coincidence function depends on the sum of the relative phases and a constant offset<sup>3</sup> given  $\omega_p\Delta T$ . The coincidence function  $R$  varies between 0 and 1 giving a perfect visibility. Any mismatch between either the  $s$  and  $l$  mode or between the  $A$  and  $B$  spatial mode will result in an increase in the minimum of  $R$  decreasing the visibility.

### 5.3 Generation of Higher Dimensional States and Hyperentanglement

In the next chapter, we experimentally determine the lower bound of the dimensionality of a bipartite quantum system. The dimensionality  $d$  of the system is defined there as the number of independent bases needed to completely span the Hilbert space of each individual party  $A$  or  $B$ . Based on this definition, the maximally-entangled polarization Bell states in Eq. 2.8 have  $d = 2$ , since there are only two independent polarization bases,  $|H\rangle$  and  $|V\rangle$ , for either  $A$  or  $B$ .

There are multiple ways of implementing a bipartite quantum system with a higher dimensionality<sup>4</sup>, i.e.  $d > 2$ . For a typical SPDC setup, similar to the one described in Chapter 3 and 4 which generates polarization-entangled photon pairs in a crossed-ring configuration [7, 63, 93], one way to accomplish this is to increase the pump power. This is due to the fact that the probability of down-conversion scales linearly with the pump power [152–154]. At sufficiently high power, the probability of generation of double pairs that are temporally close to each other becomes significant compared to that of pairs, resulting in contributions from two-photon states with  $d = 2$  and multiphoton states with  $d = 4$  [155, 156]. This increase in pump power is often effected by operating the pump in the pulsed regime [155–157] where the instantaneous power is much higher than that found in the CW case. As mentioned in Section 2.5, when conducting 2-photon measurements in which the 4-photon

<sup>3</sup>The origin of this term for both the energy-time and time-bin case is explained in Section 5.1

<sup>4</sup>For the purpose of this thesis, we will only be touching on the dimensionality of these quantum states and not the quality of entanglement associated with them, i.e. specifics about the form of these higher dimensional states will not be covered.

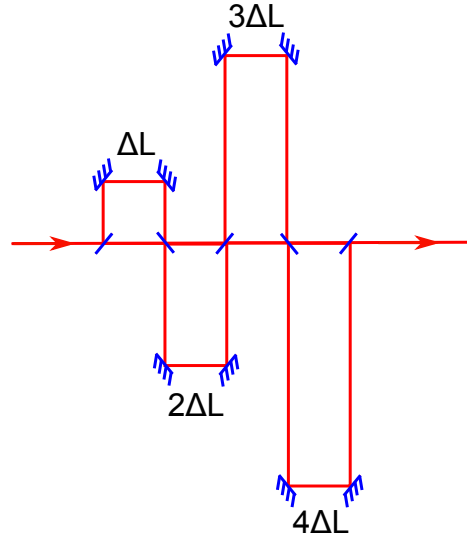


Fig. 5.4 Energy-time bipartite states with a dimensionality,  $d > 2$ , can be implemented by cascading two or more interferometers in each arm of both  $A$  and  $B$  [40–42]. The difference between the long path of each of the interferometers must be greater than the coherence length of the down-converted photons to avoid single photon interference and  $\Delta T$  must be greater than coincidence window  $\tau_C$  such that the various energy-time combinations are distinguishable. Given the constraint, the natural choice of the length of the long paths for a cascade of  $n$  interferometer is  $\Delta L$ ,  $2\Delta L$ ,  $3\Delta L$ , ..., and  $n\Delta L$ .

states are not resolved, these double pairs would manifest themselves as white noise, lowering the quality of entanglement. When the double pairs are made coherent to each other like in the case of stimulated emission [157, 158], a maximally entangled 4-photon polarization state is obtained.

Energy-time bipartite states with a higher dimensionality,  $d > 2$ , can be implemented by cascading two or more interferometers (Fig. 5.4) in each arm of both  $A$  and  $B$  [40–42]. All the interferometers in each arm need to satisfy the conditions listed in Section 5.1. The difference between the long path of each of the interferometers must be greater than the coherence length of the down-converted photons to avoid single photon interference and  $\Delta T$  must be greater than coincidence window  $\tau_C$  such that the various energy-time combinations are distinguishable. Given the constraint, the natural choice of the length of the long paths for a cascade of  $n$  interferometer is  $\Delta L$ ,  $2\Delta L$ ,  $3\Delta L$ , ..., and  $n\Delta L$ . If for example there are two cascaded interferometers, the photons can take one of 4 possible paths,  $|s + s\rangle$ ,  $|l + s\rangle$ ,  $|s + 2l\rangle$ , and  $|l + 2l\rangle$  to the detector.

It should be noted that as long as the coherence length  $l_{C_p}$  of pump is longer than the path-length difference between the shortest and longest path taken by the photons through the

cascaded interferometers, the dimensionality is directly dependent upon the post-selection by the interferometers. The dimensionality of these states, unlike the polarization case, are not limited to the number of photons in each individual mode  $A$  or  $B$  as they not using the internal degrees of freedom of the photon for encoding the state<sup>5</sup>. Experimental implementation of this scheme would however be difficult as it requires a complicated stabilization scheme for the all the interferometers. A complicated multiple delay coincidence detection scheme is also required to resolve the different combination.

For the experiment described in Chapter 6, we need to generate a bipartite state with  $d = 4$ . Instead of obtaining this expanded dimensionality by using the same degrees of freedom, similar to the two cases discussed earlier, we combined different degrees of freedom to produce what is termed a hyperentangled state [76–78]. Hyperentangled states allow improvement in super dense coding [159], full Bell-state analysis [160–163], simplification of quantum logic [164], remote entangled state preparation [165], and enhancing the quantum nonlocality tests [166]. A hyperentangled state  $|\Phi\rangle$  can be defined as follows:

$$|\Phi\rangle = \prod_{i=1}^N |\phi_i\rangle, \quad (5.4)$$

where each term  $|\phi_i\rangle$  corresponds the state encoded in one of the  $N$  degrees of freedom describing the bipartite system. For the state used in Chapter 6, is given by:

$$|\Phi^+\rangle = |\phi_{polarization}^+\rangle \otimes |\phi_{energy-time}^+\rangle, \quad (5.5)$$

where  $|\phi_{polarization}^+\rangle$  and  $|\phi_{energy-time}^+\rangle$ , maximally entangled state (Eq. 2.8) for polarization and energy-time degree of freedom, are given by:

$$\begin{aligned} |\phi_{polarization}^+\rangle &= \frac{1}{\sqrt{2}} (|H\rangle_A |H\rangle_B + |V\rangle_A |V\rangle_B), \\ |\phi_{energy-time}^+\rangle &= \frac{1}{\sqrt{2}} (|s\rangle_A |s\rangle_B + |l\rangle_A |l\rangle_B), \end{aligned} \quad (5.6)$$

respectively.

It is interesting to note for  $|\Phi^+\rangle$  (Eq. 5.4), a product state of two quantum states, the measurements associated with each degree of freedom are uncoupled and can be performed independently.

---

<sup>5</sup>This observation provides a very clear distinction between the physical carriers, in this case the photons, and the quantum information that is encoded with the carriers' various degrees of freedom, the qubits.



# Chapter 6

## Experimental Estimation of the Dimension Witness Quantum Systems

Certain quantum information processing and communication tasks require presence of entanglement in the system. This leads to the concept that entanglement is a kind resource to be utilized. However, the very same can well be said about the dimensionality of the Hilbert space of quantum systems. Realistically, for any practical application utilizing entangled quantum systems, high-dimensional entangled states are required, e.g. protocols involving reference frame free communication and dense coding for more decoherence resistance communication.

With such high-dimensional systems comes the need for techniques to evaluate their dimensionality. One such class of techniques is termed the dimension witnesses. Various experiments have been reported recently about the implementation of such witnesses [27, 28]. However, the major limitation with these witnesses is that they are unable distinguish a classical  $d$ -dimensional state from a  $d$ -dimensional entangled state. What is needed here is a dimension witness that does not suffer from the same limitation and is capable of assessing the dimensionality of a quantum system in a device independent way. One promising candidate which we will investigate in this chapter is the CGLMP inequality which is generalized for arbitrary high-dimensional bipartite systems. In this chapter we give a detailed overview of the derivation of the CGLMP inequality for a dimensionality of  $d = 4$ . We will also touch on the implementation of a hyperentangled state and highlight the findings from our attempt to violate the 4-dimensional CGLMP inequality.

## 6.1 CGLMP Inequality

In Chapter 3, we presented our experimental attempt at maximally violating the CHSH inequality [70] as a way to approach Tsirelson's bound [4]. The CHSH inequality, which belongs to a class of mathematical formulations broadly termed as Bell's inequalities, allow us to distinguish the predictions of local hidden variable theories (LHVs) and theories involving non-classical correlations, specifically quantum theory in our case. In that experiment, we worked with a maximally-entangled state (Eq. 2.8) with a dimensionality of  $d = 2$ , i.e. the number of independent outcomes of the measurements. The maximum violation of the CHSH inequality expected for such a bipartite, two-outcome experiment is  $S = 2\sqrt{2}$ .

The CHSH inequality can however be also generalized to experiments with  $d > 2$  [49, 151, 167] given suitable modification to correlation function  $E$  (Eq. 3.7). This inequality has the feature that the expected theoretical maximum violation decreases with the increasing  $d$  [151] and converges to the classical limit of  $S = 2$  for  $d = \infty$ . This feature may suggest somekind of an approach to classicality with large particle counts. As one might also imagine this feature renders the CHSH inequality unusable as a means to probe the dimensionality of quantum systems. A violation of less than  $S = 2\sqrt{2}$  may indicate the system has  $d > 2$  or it might due to the non-maximally entangled nature of the state describing the quantum system under test.

In 2002, Daniel Collins, Nicolas Gisin, Noah Linden, Serge Massar, and Sandu Popescu came up with a set of Bell's inequalities which came to be known collectively as the CGLMP inequality [35]. The inequality is generalized for arbitrary high-dimensional bipartite systems with two measurement settings and  $d$  outcomes on each side. What this means is that the violation increases with the dimensionality  $d$  of the system. When the inequality of a certain dimension  $d$  is violated, one can then make some deduction of the lower bound of the dimensionality of the system being probed being at least of dimensionality  $d$ .

In a bipartite system, suppose that both parties, Alice ( $A$ ) and Bob ( $B$ ) each can carry out two possible measurements,  $A_1$  or  $A_2$ , and  $B_1$  or  $B_2$ , respectively. Each measurement may have  $d$  possible outcomes denoted by  $0, \dots, d - 1$  (Fig. 6.1). The expression for the CGLMP expression can then be written as:

$$\begin{aligned}
 I_d \equiv \sum_{k=0}^{\lfloor d/2 \rfloor - 1} \left( 1 - \frac{2k}{d-1} \right) \{ & [P(A_1 = B_1 + k) + P(B_1 = A_2 + k + 1) \\
 & + P(A_2 = B_2 + k) + P(B_2 = A_1 + k)] \\
 & - [P(A_1 = B_1 - k - 1) + P(B_1 = A_2 - k) \\
 & + P(A_2 = B_2 - k - 1) + P(B_2 = A_1 - k - 1)] \}, \quad (6.1)
 \end{aligned}$$

where  $P(A_a = B_b + k)$  is the probability that the measurements  $A_a$  and  $B_b$  have outcomes that differ by  $k$  modulo  $d$ :

$$P(A_a = B_b + k) \equiv \sum_{j=0}^{d-1} P(A_a = j, B_b = j + k \bmod d), \quad (6.2)$$

where  $d \geq 2$ . For any dimensionality  $d$ , the CGLMP inequality has the classical limit of  $I_d \leq 2$ .

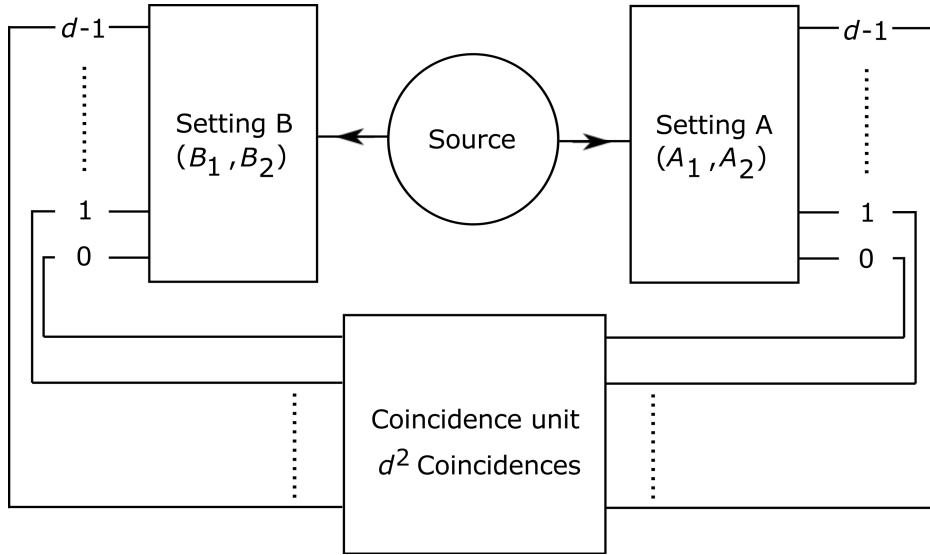


Fig. 6.1 A  $d$ -dimensional quantum system with two measurement settings  $A_1$  and  $A_2$  or  $B_1$  and  $B_2$ , and  $d$  outcomes on each side. The four different combinations of settings give in total of  $4d^2$  possible outcome of coincidence patterns which can be used for calculating the CGLMP inequality.

For bipartite system with two outcomes on each side, i.e.  $d = 2$ , the CGLMP inequality expression  $I_2$  can be written as,

$$\begin{aligned} I_2 = & [P(A_1 = B_1) + P(B_1 = A_2 + 1) + P(A_2 = B_2) + P(B_2 = A_1)] \\ & - [P(A_1 = B_1 - 1) + P(B_1 = A_2) + P(A_2 = B_2 - 1) \\ & + P(B_2 = A_1 - 1)] \end{aligned}$$

which further expands to:

$$\begin{aligned}
&= P(A_1 = 0, B_1 = 0) + P(A_1 = 1, B_1 = 1) + P(A_2 = 0, B_1 = 1) \\
&+ P(A_2 = 1, B_1 = 0) + P(A_2 = 0, B_2 = 0) + P(A_2 = 1, B_2 = 1) \\
&+ P(A_1 = 0, B_2 = 0) + P(A_1 = 1, B_2 = 1) - P(A_1 = 0, B_1 = 1) \\
&- P(A_1 = 1, B_1 = 0) - P(A_2 = 0, B_1 = 0) - P(A_2 = 1, B_1 = 1) \\
&- P(A_2 = 0, B_2 = 1) - P(A_2 = 1, B_2 = 0) - P(A_1 = 0, B_2 = 1) \\
&- P(A_1 = 1, B_2 = 0) \\
&= E(A_1, B_1) + E(A_2, B_2) + E(A_1, B_2) - E(A_2, B_1), \\
&= S,
\end{aligned} \tag{6.3}$$

thus recovering the original expression for the CHSH inequality (Eq. 3.6) for the same dimensionality.

As the dimensionality of the Hilbert space increases, the maximal violation for a maximally-entangled state:

$$|\Phi_d^+\rangle = \frac{1}{\sqrt{d}} \sum_{j=0}^{d-1} |j\rangle_A \otimes |j\rangle_B, \tag{6.4}$$

also increases. It is noteworthy to mention that for  $d > 2$ , the inequality  $I_d$  does not give the maximum violation for a maximally-entangled state [168–170]. Paradoxically, a maximum violation for  $I_d$  only occurs for the case of a non-maximally entangled state. This demonstrates the fundamental properties that non-maximally entangled states are more resistant to noise than maximally-entangled states. The same conclusion cannot be reached with the CHSH inequality.

For the purpose of this chapter, to assess the CGLMP inequality as a dimension witness, we will focus on the case of a bipartite system with dimensionality  $d = 4$  (this is the minimum dimensionality where the behaviors of CHSH and CGLMP inequality diverges), with two measurement settings at each party.  $A$  and  $B$  can each perform two possible measurements,  $A_1$  or  $A_2$ , and  $B_1$  or  $B_2$ , respectively. Each measurement will yield 4 possible outcomes, giving a total of 64 joint outcomes when all 4 possible combinations of  $A$  and  $B$  settings are considered.

The computation of these high-dimensional CGLMP inequalities has been the subject of several numerical studies [171, 172] in recent years. They provided a simple expression for the CGLMP expression:

Let  $P_{AB}^{o_a o_b}(s_a, s_b)$  be the joint probability of  $A$  and  $B$  obtaining outcomes  $o_a$  and  $o_b$  with the measurement setting  $s_a$  and  $s_b$ , respectively, where  $o = 1, \dots, d$  and  $s = 1, \dots, m$  ( $m$  pos-

sible measurement settings). Suppose now  $A$  and  $B$  have  $m_A$  and  $m_B$  possible measurement settings that would each generate  $d_A$  and  $d_B$  outcomes, respectively. For a compact description of the number of local measurement settings and the number of possible outcomes for each local measurement, we denote  $\mathbf{m} \equiv (m_A, m_B)$  and  $\mathbf{d} \equiv (d_A, d_B)$ . A simplified and equivalent CGLMP expression  $I_{\mathbf{m};\mathbf{d}}$  with two measurement settings  $m_A = m_B = 2$  and  $d$  possible outcomes,  $d_A = d_B = d$ , can then be defined as [173]:

$$I_{22dd}(\text{LHV}) = \sum_{o_a=1}^{d-1} \sum_{o_b=1}^{d-o_a} P_{AB}^{o_a o_b}(1, 1) + \sum_{o_a=1}^{d-1} \sum_{o_b=n-o_a}^{d-1} [P_{AB}^{o_a o_b}(1, 2) + P_{AB}^{o_a o_b}(2, 1) - P_{AB}^{o_a o_b}(2, 2)] - \sum_{o_a=1}^{d-1} P_A^{o_a}(1) - \sum_{o_b=1}^{d-1} P_B^{o_b}(1) \leq 0. \quad (6.5)$$

For two outcomes  $d = 2$ , the above expression further reduces to:

$$I_{2222}(\text{LHV}) = P_{AB}^{11}(1, 1) + P_{AB}^{11}(1, 2) + P_{AB}^{11}(2, 1) + P_{AB}^{11}(2, 2) - P_A^1(1) - P_B^1(1) \leq 0, \quad (6.6)$$

which is a form known as the CH74 [174] inequality developed by Clauser and Horne in 1974 which is equivalent to the original CHSH inequality under the assumption of no-signaling. By making the fair sampling assumption<sup>1</sup>, the CHSH inequality can be recovered from the CH74.

The  $I_{2222}$  contains only the measurement with one outcome  $P_A^1(1)$  or  $P_B^1(1)$ , so whether or not the total measurement outcomes 1 and 2 represents a fair sample of the total events emitted from the source is irrelevant. Fair sampling takes into account no detection and double detection events in  $A$  and  $B$ 's outcomes. It is considerably more general compared to the CHSH inequality but is difficult to implement in practice. This is because one would need ideal detectors to measure the total events received by  $A$  and  $B$  in order to establish the quantity  $P_A^1(1)$  and  $P_B^1(1)$ .

The CGLMP expression  $I_d$  in Eq. 6.1 is equivalent to the  $I_{22dd}$  expression in Eq. 6.6 [173] and the two inequalities are related as follows:

$$I_{22dd} = \frac{d-1}{2d}(I_d - 2). \quad (6.7)$$

In the presence of white noise, the quantum state becomes (similar to that given in Eq. 2.14b):

$$\rho(p) = p|\Phi_d^+\rangle\langle\Phi_d^+| + (1-p)\frac{\mathbb{I}_d \otimes \mathbb{I}_d}{d^2}, \quad (6.8)$$

<sup>1</sup>The fair sampling assumption states that the sample of detected pairs is representative of the pairs emitted.

where  $\mathbb{I}$  is an identity matrix with dimension  $d$  and  $p$  is the weight of the  $d$ -dimensional maximally-entangled state in the mixture. The CGLMP expression is certainly violated if  $p > \frac{2}{I_d(\text{QM})} = p_w$ .

Table 6.1 shows the summary of different types of violation with two measurement settings and  $d$  outcomes. It has been shown that the maximum CGLMP violation  $I_d^{\max}(\text{QM})$  does not correspond to maximally entangled input states [168, 175].  $I_d^{|\Phi_d^+\rangle}$  is the maximum violation for an maximally entangled input state  $|\Phi_d^+\rangle$ .  $I_{22dd}^{|\Phi_d^+\rangle}$  is the corresponding best known  $I_{22dd}$  violation given in Eq. 6.7. Below the threshold weight  $p_w$ , no violation is expected. For  $d \geq 2$ ,  $I_d^{\max}(\text{QM})$  increases suggesting a larger violation could be possible by

Table 6.1 CGLMP  $I_d(\text{QM})$  and  $I_{22dd}$  violation [173].

$d$	$I_d^{\max}(\text{QM})$	$I_d^{ \Phi_d^+\rangle}$	$I_{22dd}^{ \Phi_d^+\rangle}$	$p_w$
2	2.8284	2.8284	0.20711	0.70711
3	2.9149	2.8729	0.29098	0.69615
4	2.9727	2.8962	0.33609	0.69055
5	3.0157	2.9105	0.36422	0.68716
6	3.0497	2.9202	0.38342	0.68488
7	3.0776	2.9272	0.39736	0.68326
8	3.1013	2.9324	0.40793	0.68203
9	3.1217	2.9365	0.41622	0.68108
10	-	2.9398	0.42291	0.68032
100	-	2.9668	0.47856	0.67413
1000	-	2.9695	0.48427	0.67351
$\infty$	-	2.9698	0.48491	0.67349

increasing the dimension of the system. The  $p_w$  values indicate that the CGLMP violation of higher dimensional systems are more resistant to noise.

In the later section, we will use the CGLMP inequality as a dimension witness for our  $d = 4$  experiment. The idea of dimension witness is that there exists an upper bound of CGLMP violation if we restrict ourself to lower dimensional systems. In this particular case, the maximum violation of  $I_{2244}$  with qutrits ( $d = 3$ ), is strictly lesser than ququads ( $d = 4$ ). The maximal violation of  $I_{2244}$  with qutrits could be shown to be identical to  $I_{2233}^{\max} = 0.304951$  [176, 177]. To summarize, for experiment with two measurement settings and four outcomes on each side, if the bound  $I_{2233}^{\max} \leq 0.304951$  is violated, the dimension of the entangled system under investigation is at least 4.

This  $I_{2244}$  will be useful later for comparison with our experimental results to verify if we indeed have a 4-dimensional maximally-entangled state.

### 6.1.1 Derivation of the 4-Dimensional CGLMP Inequality

We now attempt to derive the maximum violation of  $I_{2244} = 0.33609$  (in Table 6.1) for a 4-dimensional maximally-entangled state using the CGLMP expression in Eq. 6.5. Following the derivation steps given in Section 2.4, we start by writing a 4-dimensional maximally-entangled state given by:

$$|\Phi\rangle = \frac{1}{2} (|00\rangle + |11\rangle + |22\rangle + |33\rangle), \quad (6.9)$$

with the definitions:

$$\begin{aligned} |0\rangle &= (1, 0, 0, 0)^T \\ |1\rangle &= (0, 1, 0, 0)^T \\ |2\rangle &= (0, 0, 1, 0)^T \\ |3\rangle &= (0, 0, 0, 1)^T \end{aligned}$$

The detection probability (coincidence) between outcome  $|k\rangle_{A,a}$  and  $|l\rangle_{B,b}$  is written as

$$P_{AB}^{kl}(a, b) = \text{tr}(|k\rangle_{A,a}\langle l|_{B,b} |k\rangle_{A,a}\langle l|_{B,b} \rho). \quad (6.10)$$

The corresponding density matrix is written as (the zeros are replaced by dots):

$$\rho = |\Phi\rangle\langle\Phi| = \begin{pmatrix} \frac{1}{4} & \cdot & \cdot & \cdot & \frac{1}{4} & \cdot & \cdot & \cdot & \cdot & \frac{1}{4} & \cdot & \cdot & \cdot & \cdot & \frac{1}{4} \\ \cdot & \cdot \\ \cdot & \cdot \\ \cdot & \cdot \\ \frac{1}{4} & \cdot & \cdot & \cdot & \frac{1}{4} & \cdot & \cdot & \cdot & \cdot & \frac{1}{4} & \cdot & \cdot & \cdot & \cdot & \frac{1}{4} \\ \cdot & \cdot \\ \cdot & \cdot \\ \cdot & \cdot \\ \frac{1}{4} & \cdot & \cdot & \cdot & \frac{1}{4} & \cdot & \cdot & \cdot & \cdot & \frac{1}{4} & \cdot & \cdot & \cdot & \cdot & \frac{1}{4} \\ \cdot & \cdot \\ \cdot & \cdot \\ \cdot & \cdot \\ \frac{1}{4} & \cdot & \cdot & \cdot & \frac{1}{4} & \cdot & \cdot & \cdot & \cdot & \frac{1}{4} & \cdot & \cdot & \cdot & \cdot & \frac{1}{4} \end{pmatrix}. \quad (6.11)$$

Referring to the CGLMP expression in Eq. 6.5, for  $d = 4$ , this expression can be written as:

$$\begin{aligned} I_{2244}(\text{QM}) &= \sum_{k=1}^3 \sum_{l=1}^{4-k} P_{AB}^{kl}(1,1) + \sum_{k=1}^3 \sum_{l=4-k}^3 [P_{AB}^{kl}(1,2) + P_{AB}^{kl}(2,1) - \\ & P_{AB}^{kl}(2,2)] - \sum_{k=1}^3 P_A^k(1) - \sum_{l=1}^3 P_B^l(1) \\ &= P_{AB}^{11}(1,1) + P_{AB}^{12}(1,1) + P_{AB}^{13}(1,1) + P_{AB}^{21}(1,1) \\ &+ P_{AB}^{22}(1,1) + P_{AB}^{31}(1,1) + P_{AB}^{13}(1,2) + P_{AB}^{22}(1,2) \\ &+ P_{AB}^{23}(1,2) + P_{AB}^{31}(1,2) + P_{AB}^{32}(1,2) + P_{AB}^{33}(1,2) \\ &+ P_{AB}^{13}(2,1) + P_{AB}^{22}(2,1) + P_{AB}^{23}(2,1) + P_{AB}^{31}(2,1) \\ &+ P_{AB}^{32}(2,1) + P_{AB}^{33}(2,1) - P_{AB}^{13}(2,2) - P_{AB}^{22}(2,2) \\ &- P_{AB}^{23}(2,2) - P_{AB}^{31}(2,2) - P_{AB}^{32}(2,2) - P_{AB}^{33}(2,2) \\ &- P_A^1(1) - P_A^2(1) - P_A^3(1) - P_B^1(1) - P_B^2(1) - P_B^3(1). \end{aligned} \quad (6.12)$$



We then perform a swap of Bob's outcomes shown in Table 6.3 with -1 representing the coefficient of the probability of  $P_A^k$  or  $P_B^l$  shown in Eq. 6.12. The six additional terms, namely  $P_A^1(1)$ ,  $P_A^2(1)$ ,  $P_A^3(1)$ ,  $P_B^1(1)$ ,  $P_B^2(1)$  and  $P_B^3(1)$  are practically impossible to measure. As an example, with the condition  $P_{AB}^{14}(1, 1) + P_{AB}^{24}(1, 1) + P_{AB}^{34}(1, 1) + P_{AB}^{44}(1, 1) - P_B^4(1) = 0$ , we added the coefficients of this condition into Table 6.4 [178].

The coefficients of the non-joint probabilities in the Table 6.4 are taken care of by the conditions,  $-P_A^1(1) - P_A^2(1) - P_A^3(1) - P_A^4(1) = 1$  and  $-P_B^1(1) - P_B^2(1) - P_B^3(1) - P_B^4(1) = 1$ . Therefore these probabilities need not be measured in the experiment. The CGLMP inequality thus requires a minimum of 32 joint probabilities to be measured. Finally, for a 4-dimensional maximally-entangled state, the maximum violation of the CGLMP is evaluated to be  $I_{2244}^{\max}(\text{QM}) = 0.33609$ . Thus for a verification of a dimensionality of  $d = 4$ , we need  $0.304951 \leq I_{2244}^{\max}(\text{QM}) \leq 0.33609$ .

## 6.2 Implementation of 4-Dimensional Entangled Photons

For our experimental test of the CGLMP inequality  $I_{2244}$  as a dimension witness for a dimensionality of  $d = 4$ , we implemented a hyperentangled state consisting of a maximally-entangled polarization  $|\phi_{\text{polarization}}^+\rangle$  and energy-time  $|\phi_{\text{energy-time}}^+\rangle$  state each with a dimensionality of  $d = 2$ . As discussed in Section 5.3 the hyperentangled state can be written as:

$$|\Phi^+\rangle = |\phi_{\text{polarization}}^+\rangle \otimes |\phi_{\text{energy-time}}^+\rangle. \quad (6.13)$$

Similar to the experiments performed in Chapter 3 and 4, for the polarization degree of freedom, we implemented a typical spontaneous parametric down-conversion source (SPDC) to generate the maximally-entangled polarization state  $|\phi_{\text{polarization}}^+\rangle$  (Eq. 2.8). In our experiment (Fig. 6.2a), the output of a laser diode (LD, central wavelength 405 nm) passes through a single mode optical fiber (SMF) for spatial mode filtering and is focused to a beam waist of  $80 \mu\text{m}$  into a 2 mm thick BBO crystal. In this crystal (cut for type-II phase-matching), photon pairs are generated via SPDC in a slightly non-collinear configuration. A half-wave plate ( $\lambda/2$ ) and a pair of compensation crystals (CC) take care of the temporal and transversal walk-off [7].

Two spatial modes (labeled  $A$  and  $B$ ) of down-converted light, defined by the SMFs for 810 nm, are matched to the pump mode to optimize the collection [63]. In type-II SPDC, each down-converted pair consists of an ordinary and extraordinarily polarized photon, corresponding to horizontal (H) and vertical (V) in our setup. A pair of polarization controllers (PCs) ensures that the stress-induced dispersion in the SMFs do not affect the polarization of the collected photons. One of the PCs is adjusted such that it rotates the polarization of

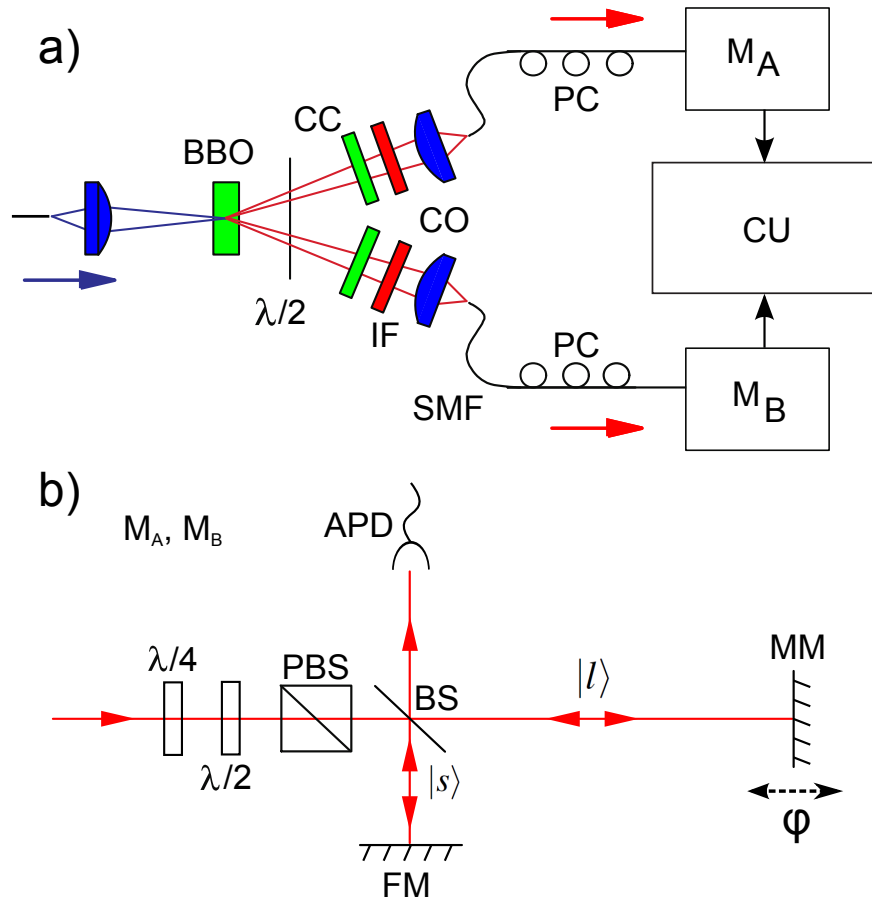


Fig. 6.2 Implementation and analysis of the polarization and energy-time hyperentangled state with a dimensionality of  $d = 4$ . a) Entangled photon pairs are generated by a typical spontaneous parametric down-conversion (SPDC) setup in a crossed-ring configuration. b) The polarization degree of freedom of the down-converted photons is first analyzed on an optical bench consisting of a quarter-wave ( $\lambda/4$ ), half-wave plate ( $\lambda/2$ ), and a polarization beam splitter (PBS). This is followed by an unbalanced Michelson interferometer where the energy-time degree of freedom is analyzed. The photons are detected by silicon avalanche photodetectors (APD) and the signals registered on a coincidence unit (CU).

the photons by  $90^\circ$ , i.e.  $|H\rangle \leftrightarrow |V\rangle$ . The CC is then adjusted to generate a  $|\phi_{polarization}^+\rangle$  state. Interference filters (IF) with bandwidth of 5 nm are placed in front of the collection for spectral filtering of the intended down-conversion wavelength of 810 nm.

In the analyzer (Fig. 6.2b), projection of the collected down-converted photons onto arbitrary the polarization is done by an optical bench consisting of a quarter-wave ( $\lambda/4$ ) and half-wave plate ( $\lambda/2$ ) followed by a polarization beam splitter (PBS). For the energy-time

analysis, we implemented two unbalanced Michelson interferometers<sup>2</sup>  $M_A$  and  $M_B$ . Each interferometer consist of a 50:50 beam splitter (BS) with a fixed retro-reflecting mirror (FM) and a moveable retro-reflecting mirror (MM). The BS splits the incoming light into two paths which get retro-reflected by the mirrors and recombined in the same BS. Movement of the MM is effected by means of a piezo<sup>3</sup> driven translation stage with a travel range of up to  $17.4\ \mu\text{m}$ . The directions of movement are aligned to be parallel to the path of the beam. The MM assembly of one of the interferometers is further mounted on a motorized linear translation stage, which extends its range of travel to 25 mm. This is used for coarse scanning purposes later on. To further enhance the spatial mode overlap between the  $|s\rangle$  and  $|l\rangle$  path, we introduce short patch of SMF just before APDs to spatially select a single spatial mode. Photons are detected by avalanche photo diodes (APDs, quantum efficiency  $\approx 40\%$ ) and corresponding detection events from the same pair identified by a coincidence unit (CU) if they arrive within  $\approx \pm 1.2\ \text{ns}$  of each other.

As mentioned in Section 5.1, a number of conditions must be satisfied for the generation of energy-time entanglement. The pump light comes from a grating feedback stabilized external cavity diode laser. The typical frequency bandwidth of such a laser is on the order of a few MHz which translates a coherence length  $l_{C_p}$  of meters. This was independently verified by sending light from the laser into an unbalanced Michelson interferometer with a path-length different of 4 m and seeing high visibility of the interference fringes.

The CU has a minimum coincidence time window of  $\tau_C$  is 1.2 ns. From Section 5.1 we established that the minimum path-length difference of the interferometer has to be at least  $2c\tau_C$ , where  $c$  is the speed of light, in order for the different energy-time combinations to be distinguished. This corresponds to a minimum path-length difference of 0.72 m in our case. For our interferometer, we set the length difference between the FM-BS and MM-BS distance<sup>4</sup> to be 0.38 m, giving us a round trip path-length difference of 0.76 m between the two arms of the interferometer, greater than the minimum required. As the down-converted light typically has a bandwidth of a few nm, its coherence length  $l_{C_{dc}}$  is much shorter than of path-length difference of the interferometers in our case. Thus there is no concern of single photon interference.

---

<sup>2</sup>The Michelson interferometer is functionally similar to the Mach-Zehnder interferometer but it is easier to set up and alignment in our case. The choice is also motivated by our use of a movable mirror to effect the phase shift  $\phi$  in the interferometer

<sup>3</sup>Piezoelectric actuator AE0505D16F, Thorlabs.

<sup>4</sup>The experiment is being installed on an imperial optical table where the mounting holes are all 1 inch apart. For the ease of referencing, we chose the length difference between the FM-BS and MM-BS distance to be 15 mounting holes apart or 15 inch, giving us the seemingly odd choice of 0.38 m.

### 6.2.1 Setting the Electronic Delays

The CU can reach a minimum coincidence time window  $\tau_C$  of 1.2 ns. Thus in order to properly post-select the central peak (Fig. 5.3) consisting of the  $|l\rangle_A|l\rangle_B$  and  $|s\rangle_A|s\rangle_B$  combinations, the total delay, including both optical and electronic delays, must be equal. In order to zero the delay between the two output signals of the APDs at the CU, an electronic delay stage is fitted to each of the two signal lines leading to the CU. To ascertain the correct delay settings, we monitor the coincidence counts between the two APDs and while keeping  $A$ 's delay fixed, we scan the electronic delay of the signal from  $B$ 's detector over a range of a few ns. By doing this, we obtain Figure 6.3.

From Figure 6.3, we can see that the delay between consecutive peaks is  $\approx 2.5$  ns, consistent with that expected from a path-length difference of  $\Delta L = 0.76$  m in the interferometers. By setting the  $B$ 's delay to 3.38 ns, we are in the regime of zero delay between the output signals from the two APDs at the CU. We can also deduce that with our choice of 0.76 m for the path-length difference of the interferometers, the CU can efficiently post-select just events from the  $|l\rangle_A|l\rangle_B$  and  $|s\rangle_A|s\rangle_B$  combinations.

### 6.2.2 Optimizing the Quality of the Interferometers

To achieve high quality entanglement of the energy-time degree of freedom, we first need to ensure that there is a good overlap between the spatial modes of the  $|s\rangle$  and  $|l\rangle$  path within each interferometer. Light from the input coupler going into the analyzer is made highly collimated such that it maintains its the spatial profile after propagating through the two paths of the interferometer and still overlap nicely before the the collection of the APDs. Using light from a grating feedback stabilized external cavity 810 nm diode laser, our calibration laser, which has a coherence length longer the than the path-length difference  $\Delta L$  of the interferometers, we measure the visibility of the interference obtained by scanning the position of the MM with the piezo stage. Small adjustments are then made to the pointing of the FM, MM and the tilt of the BS until visibility is maximized for both interferometers .

Secondly we need to ensure that the path-length difference of the two interferometers are identical. This check is done by first coupling the output from the  $A$  interferometer to the input of the  $B$  interferometer. Light from an infrared LED is then sent into the input of the  $A$  interferometer and the output signal from the  $B$  interferometer is monitored while MM for  $B$  is scanned using the motorized translation stage (Fig. 6.4). As the light from the infrared LED is fairly broadband, it has a coherence length on the order of hundreds of  $\mu\text{m}$ . Thus there will only be interference of the the two path  $|s\rangle_A|l\rangle_B$  and  $|l\rangle_A|s\rangle_B$  when the two path-length differences are near identical. We term this as the zero path-length condition.

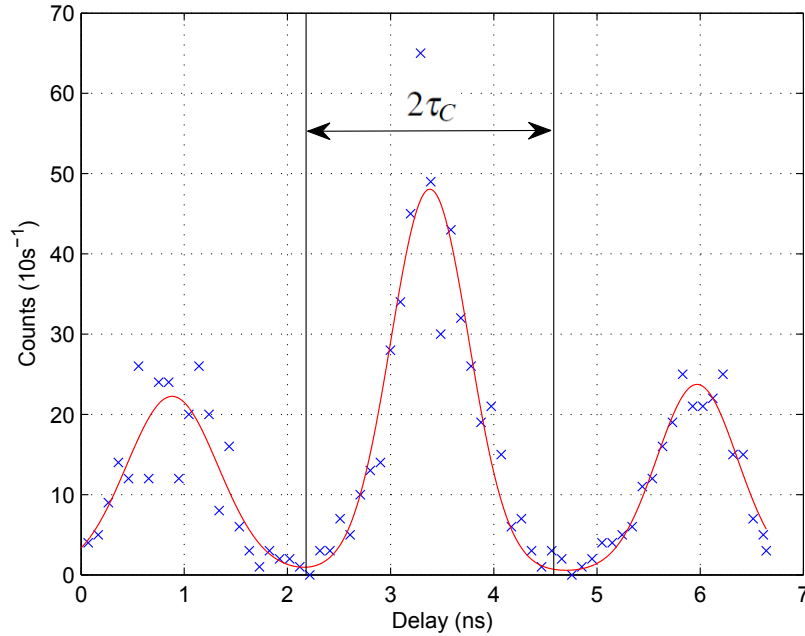


Fig. 6.3 In order to zero the delay between the two output signals of the APDs at the CU, an electronic delay stage is fitted to each of the two signal lines leading to the CU. To ascertain the correct delay settings, we monitor the coincidence counts between the two APDs and while keeping  $A$ 's delay fixed, we scan the electronic delay on the signal from  $B$ 's detector over a range of a few ns.

The position of the MM for  $B$  is then set to the center of the envelope of the interference for the zero path-length regime.

As the last process involving scanning the position of MM for  $B$  over a range much larger than that of the piezo, there is a high chance of the MM getting misaligned. Thus the total alignment procedure involves iterating between these two steps until a high visibility of interference is achieved for both interferometers. For this particular alignment, we got the visibility of interference to be a 97.4% and 97.3% for  $A$  and  $B$ 's interferometer respectively just before the collection of the APDs. With the inclusion of a short patch of SMF for spatial filtering, these figures increased to 99.4% and 99.6% respectively. The visibility of the interference of the two interferometer thus imposes an upper limit of 99.0% to expected visibility of the Franson interference for the energy-time state that we will characterize later.

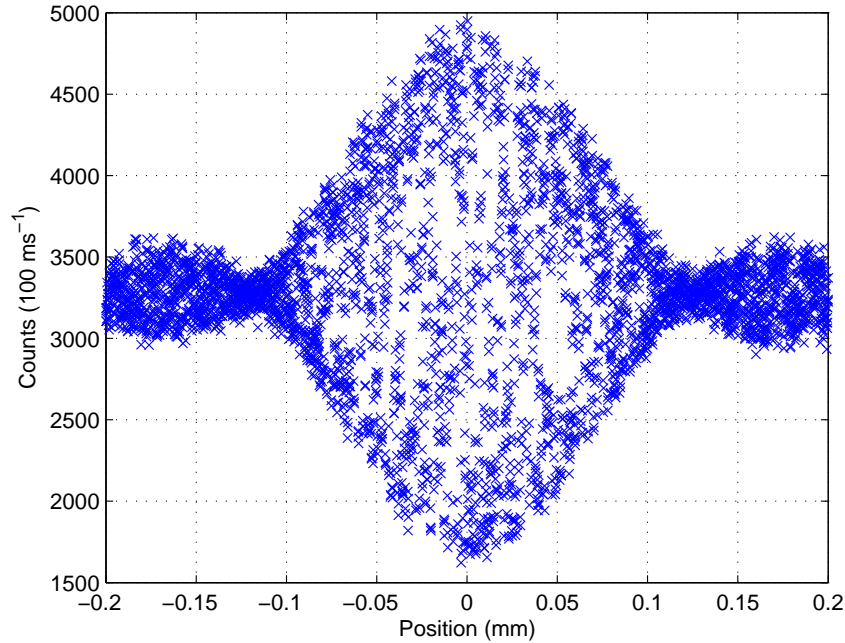


Fig. 6.4 By cascading the two interferometers one after the other and scanning the MM of the  $B$  interferometer, interference between the  $|s\rangle_A|l\rangle_B$  and  $|l\rangle_A|s\rangle_B$  path can be observed using broadband light from an infrared LED. The position of the center of the interference envelope corresponds to the case of a zero path-length difference between the  $|s\rangle_A|l\rangle_B$  and  $|l\rangle_A|s\rangle_B$ , indicating that the individual path-length difference of each interferometer,  $\Delta L$  are identical.

### 6.2.3 Phase Setting and Stabilization of the Interferometers

To effect the various phase settings,  $\phi$  between the  $|s\rangle$  and  $|l\rangle$  path in each of the two interferometers, the MM are moved minutely using piezoelectric actuators. These piezos transform electrical energy into precisely controlled mechanical displacements. They are ideal for applications requiring rapid, precise positional changes on the nanometer or micrometer scale. However, they suffer from the non-linearity of the mechanical displacements with the voltage applied and hysteresis effect.

To overcome this issue, we opted for the use of piezo stacks with integrated strain gauges. These strain gauges are small resistance bridges that are stretched along the length of the piezos. Their resistance changes linearly with extension of the piezos. Using the output resistance of these strain gauges as feedbacks, we implemented a closed-loop PID control of the extension of the piezos.

To set a certain phase,  $\phi$  between the  $|s\rangle$  and  $|l\rangle$  path, we first send narrowband 810 nm light from our calibration laser, mentioned in the previous section, into each interferometer and scan the MM over a range of slightly more than a complete wavelength. We then fit the resulting measurements of the number of counts registered by the APDs versus the strain gauge reading to a sinusoidally varying function. From the fit parameters, we can determine the correct strain gauge reading that corresponds to the phase setting we want. We then command the piezo to move to the corresponding position with that particular strain gauge reading. To characterize the accuracy of this procedure, we measured multiple cycles of the counts versus the phase setting  $\phi$  ranging from 0 to  $2\pi$ . The curves are then fitted to a sinusoidally varying function to determine their minimum positions which is expected at  $\phi = \pi$ . The result of the repeated measurement shows a spread of the expected minimum position  $\pi$  by  $\pm 0.1$  rad, giving us the uncertainty of the phase setting with this procedure.

To lessen the effect of thermal fluctuation and mechanical vibration on the stability of the interferometers, both analyzers are enclosed with a cover. With the enclosure the interferometers display a characteristic time of about 1.5 min before the set phase,  $\phi$  starts to drift. This limits the integration time of each measurement point to less than 1.5 min and at the same time, the calibration cycle needs to be performed for both interferometers before every measurement.

#### 6.2.4 Stabilization of the Calibration and Pump Laser

From Eq. 5.1, we can see that the energy-time entangled state depends on the phase,  $\phi_A$  and  $\phi_B$  of the  $A$  and  $B$  interferometer, respectively. It is also dependent on the phase,  $\phi_p$  of the pump which in our case is related to the frequency of the pump light. Since a 810 nm calibration laser is used to calibrate the phase settings of the two interferometers, the resulting energy-time entangled state is thus heavily dependent on the relative frequency of the two lasers.

In order to maintain a fixed frequency relation between the two lasers, both lasers have their frequency locked to the same wavemeter. Output readings from the wavemeter are used in a closed loop feedback control of the position of the grating to keep their output stable at a certain frequency. The frequency accuracy of 60 MHz for the wavemeter limits how well the lasers are locked to each other and thus the accuracy at which we can generate the required energy-time entangled state.

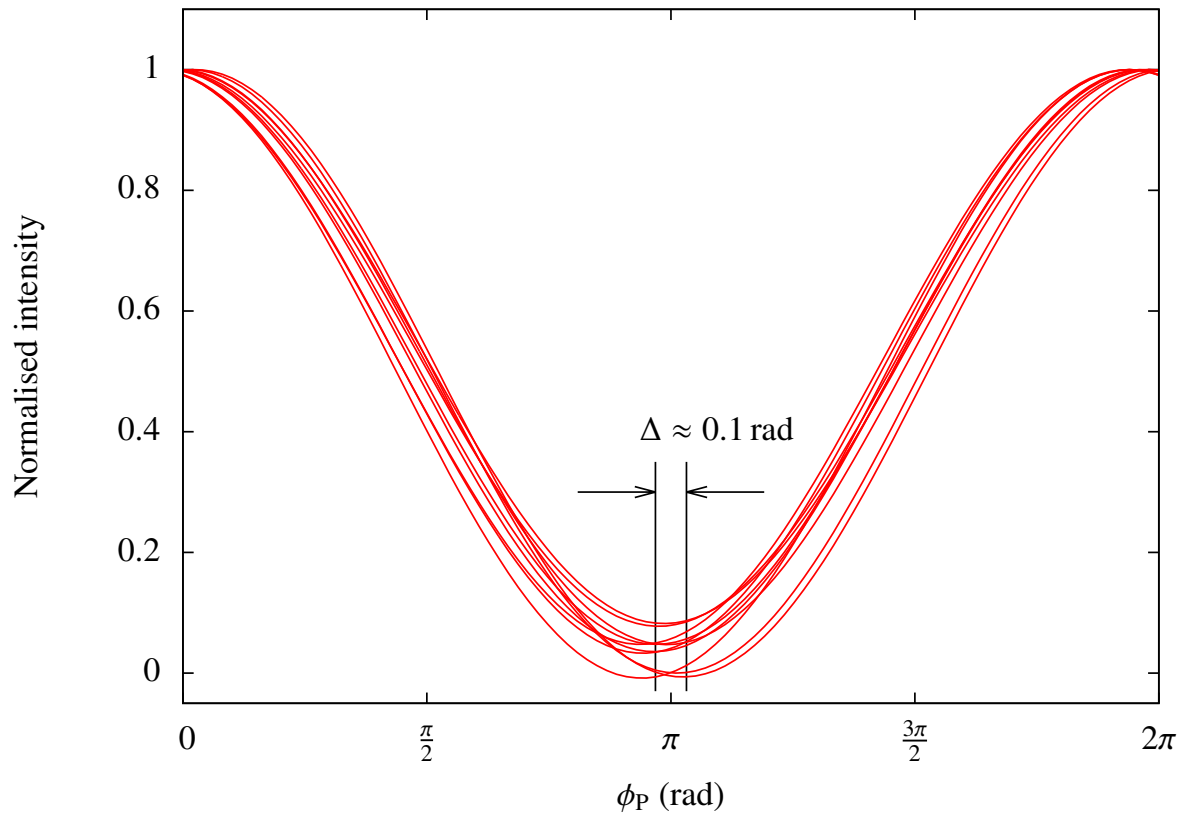


Fig. 6.5 In order to characterize the accuracy at which we can set the phases in the interferometers, multiple cycles of the counts versus the phase setting  $\phi$  ranging from 0 to  $2\pi$  were measured. Fits to a sinusoidally varying function were performed to determine their minimum positions which is expected at  $\phi = \pi$ . The fitted minimum positions show a spread of the expected minimum position  $\pi$  by  $\pm 0.1$  rad, giving us the uncertainty of the phase setting with this procedure.

### 6.2.5 Characterization of the Hyperentangled State

In order to ascertain the quality of entanglement between the photon pairs, we probe their polarization and energy-time degree of freedom separately. For polarisation entanglement between the photon pairs, polarization correlations in the H/V basis (the natural basis, *i.e.*, the basis aligned to the crystal axes) and  $+45^\circ/-45^\circ$  bases (the complementary basis) are measured (Fig. 6.6, upper). We obtain  $V_{HV} = 100 \pm 1\%$  and  $V_{45} = 99.1 \pm 0.9\%$ . For the energy-time correlations, we measured the Franson interference of the path  $|s\rangle_A|s\rangle_B$  and  $|l\rangle_A|l\rangle_B$  (Fig. 6.6, lower) and obtain a visibility of  $V = 100 \pm 9\%$ . The large error bound for  $V$  can be attributed to the low signal counts collected within the short integration time. The non-zero phase of the Franson interference can be attributed to a mismatch between the wavelength of the light from the calibration laser and the pump laser. This mismatch is compensated for in the main measurement by offset the phase setting of the  $B$  interferometer by the same corresponding amount.

## 6.3 Measurement Settings

In Section 6.1.1 we derived the maximal violation of the CGLMP,  $I_{2244}$  expected for a maximally-entangled state (Eq. 6.9) with  $d = 4$ , written in the form of:

$$|\Phi\rangle = \frac{1}{2} (|00\rangle + |11\rangle + |22\rangle + |33\rangle).$$

We now look at the equivalence between the above maximally-entangled state and the hyperentangled state in Eq. 6.13. We start with the hyperentangled state given in Eq. 6.13:

$$|\Phi^+\rangle = |\phi_{\text{polarization}}^+\rangle \otimes |\phi_{\text{energy-time}}^+\rangle, \quad (6.14)$$

where  $|\phi_{\text{polarization}}^+\rangle$  and  $|\phi_{\text{energy-time}}^+\rangle$  are given by Eq. 5.6:

$$\begin{aligned} |\phi_{\text{polarization}}^+\rangle &= \frac{1}{\sqrt{2}} (|H\rangle_A|H\rangle_B + |V\rangle_A|V\rangle_B), \\ |\phi_{\text{energy-time}}^+\rangle &= \frac{1}{\sqrt{2}} (|s\rangle_A|s\rangle_B + |l\rangle_A|l\rangle_B), \end{aligned}$$

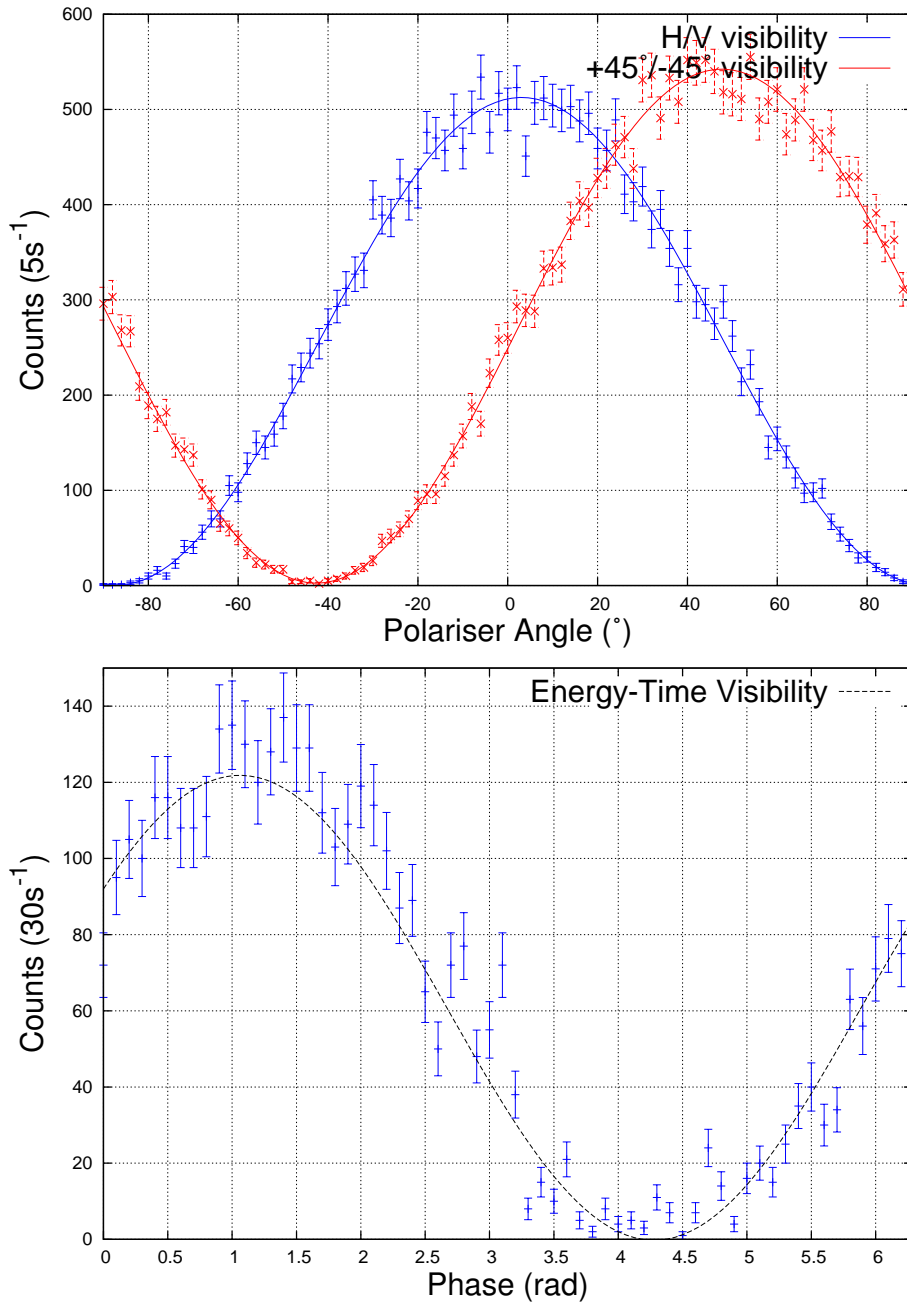


Fig. 6.6 Polarization correlations (upper) in the H/V and  $+45^\circ/-45^\circ$  bases. We observed direct visibilities of  $V_{HV} = 100 \pm 1\%$  and  $V_{45} = 99.1 \pm 0.9\%$ . The energy-time visibility (lower) for coincidences between the signals at output of both interferometers is  $V = 100 \pm 9\%$ . The large error bound for  $V$  can be attributed to the low signal counts collected within the short integration time.

respectively. Thus  $|\Phi^+\rangle$  can be expanded to:

$$\begin{aligned} |\Phi^+\rangle &= \frac{1}{\sqrt{2}} (|H\rangle_A |H\rangle_B + |V\rangle_A |V\rangle_B) \otimes \frac{1}{\sqrt{2}} (|s\rangle_A |s\rangle_B + |l\rangle_A |l\rangle_B), \\ &= \frac{1}{2} (|Hs\rangle_A |Hs\rangle_B + |Hl\rangle_A |Hl\rangle_B + |Vs\rangle_A |Vs\rangle_B + |Vl\rangle_A |Vl\rangle_B), \end{aligned} \quad (6.15)$$

where, for example  $|Hs\rangle_A = |H\rangle_A |s\rangle_A$ . By making the following mapping:

$$\begin{aligned} |Hs\rangle &\rightarrow |0\rangle, \\ |Hl\rangle &\rightarrow |1\rangle, \\ |Vs\rangle &\rightarrow |2\rangle, \\ |Vl\rangle &\rightarrow |3\rangle, \end{aligned} \quad (6.16)$$

the maximally-entangled state,  $|\Phi\rangle$  in Eq. 6.9 can be recovered.

In the CGLMP paper [35] discussed the Eq. 6.4, a maximally-entangled state of a two  $d$ -dimensional system has the nondegenerate eigenvectors given by:

$$\begin{aligned} |k\rangle_{A,a} &= \frac{1}{\sqrt{d}} \sum_{j=0}^{d-1} e^{i\frac{2\pi}{d} j(k+\alpha_a)} |j\rangle_A, \\ |l\rangle_{B,b} &= \frac{1}{\sqrt{d}} \sum_{j=0}^{d-1} e^{i\frac{2\pi}{d} j(-l+\beta_b)} |j\rangle_B, \end{aligned} \quad (6.17)$$

with operators  $A_a$  where  $a = 1, 2$  measured by Alice and  $B_b$  where  $b = 1, 2$  measured by Bob, and  $\alpha_1 = 0$ ,  $\alpha_2 = \frac{1}{2}$ ,  $\beta_1 = \frac{1}{4}$  and  $\beta_2 = -\frac{1}{4}$ . Eq. 6.17 has been shown to maximize the violation of the CGLMP inequality for the maximally-entangled state of two  $d$ -dimensional system [179, 180]. We consider a dimensionality of  $d = 4$  and expand the eigenvectors:

$$|k=0\rangle_{A,1} = |0\rangle + |1\rangle + |2\rangle + |3\rangle$$

$$|k=1\rangle_{A,1} = |0\rangle + i|1\rangle - |2\rangle - i|3\rangle$$

$$|k=2\rangle_{A,1} = |0\rangle - |1\rangle + |2\rangle - |3\rangle$$

$$|k=3\rangle_{A,1} = |0\rangle - i|1\rangle - |2\rangle + i|3\rangle$$

$$|k=0\rangle_{A,2} = |0\rangle + e^{i\frac{\pi}{4}}|1\rangle + e^{i\frac{\pi}{2}}|2\rangle + e^{i\frac{3\pi}{4}}|3\rangle$$

$$|k=1\rangle_{A,2} = |0\rangle + ie^{i\frac{\pi}{4}}|1\rangle - e^{i\frac{\pi}{2}}|2\rangle - ie^{i\frac{3\pi}{4}}|3\rangle$$

$$|k=2\rangle_{A,2} = |0\rangle - e^{i\frac{\pi}{4}}|1\rangle + e^{i\frac{\pi}{2}}|2\rangle - e^{i\frac{3\pi}{4}}|3\rangle$$

$$|k=3\rangle_{A,2} = |0\rangle - ie^{i\frac{\pi}{4}}|1\rangle - e^{i\frac{\pi}{2}}|2\rangle + ie^{i\frac{3\pi}{4}}|3\rangle$$

$$|l=0\rangle_{B,1} = |0\rangle + e^{i\frac{\pi}{8}}|1\rangle + e^{i\frac{\pi}{4}}|2\rangle + e^{i\frac{3\pi}{8}}|3\rangle$$

$$|l=1\rangle_{B,1} = |0\rangle - ie^{i\frac{\pi}{8}}|1\rangle - e^{i\frac{\pi}{4}}|2\rangle + ie^{i\frac{3\pi}{8}}|3\rangle$$

$$|l=2\rangle_{B,1} = |0\rangle - e^{i\frac{\pi}{8}}|1\rangle + e^{i\frac{\pi}{4}}|2\rangle - e^{i\frac{3\pi}{8}}|3\rangle$$

$$|l=3\rangle_{B,1} = |0\rangle + ie^{i\frac{\pi}{8}}|1\rangle - e^{i\frac{\pi}{4}}|2\rangle - ie^{i\frac{3\pi}{8}}|3\rangle$$

$$|l=0\rangle_{B,2} = |0\rangle + e^{-i\frac{\pi}{8}}|1\rangle + e^{-i\frac{\pi}{4}}|2\rangle + e^{-i\frac{3\pi}{8}}|3\rangle$$

$$|l=1\rangle_{B,2} = |0\rangle - ie^{-i\frac{\pi}{8}}|1\rangle - e^{-i\frac{\pi}{4}}|2\rangle + ie^{-i\frac{3\pi}{8}}|3\rangle$$

$$|l=2\rangle_{B,2} = |0\rangle - e^{-i\frac{\pi}{8}}|1\rangle + e^{-i\frac{\pi}{4}}|2\rangle - e^{-i\frac{3\pi}{8}}|3\rangle$$

$$|l=3\rangle_{B,2} = |0\rangle + ie^{-i\frac{\pi}{8}}|1\rangle - e^{-i\frac{\pi}{4}}|2\rangle - ie^{-i\frac{3\pi}{8}}|3\rangle$$

(6.18)

If we perform the reverse mapping shown in Eq. 6.16 and decompose the resulting vector into the polarization and energy-time degree of freedom, we can obtain the corresponding settings in terms of polarization and energy-time degree of freedom to maximally violate  $I_{2244}$ . The settings are given by:

$$\begin{aligned}
|k=0\rangle_{A,1} &= (|H\rangle_A + |V\rangle_A) \otimes (|s\rangle_A + |l\rangle_A) \\
|k=1\rangle_{A,1} &= (|H\rangle_A + e^{i\pi}|V\rangle_A) \otimes (|s\rangle_A + e^{i\frac{\pi}{2}}|l\rangle_A) \\
|k=2\rangle_{A,1} &= (|H\rangle_A + e^{i2\pi}|V\rangle_A) \otimes (|s\rangle_A + e^{i\pi}|l\rangle_A) \\
|k=3\rangle_{A,1} &= (|H\rangle_A + e^{i3\pi}|V\rangle_A) \otimes (|s\rangle_A + e^{i\frac{3\pi}{2}}|l\rangle_A) \\
\\
|l=0\rangle_{A,2} &= (|H\rangle_A + e^{i\frac{\pi}{2}}|V\rangle_A) \otimes (|s\rangle_A + e^{i\frac{\pi}{4}}|l\rangle_A) \\
|l=1\rangle_{A,2} &= (|H\rangle_A + e^{i\frac{3\pi}{2}}|V\rangle_A) \otimes (|s\rangle_A + e^{i\frac{3\pi}{4}}|l\rangle_A) \\
|l=2\rangle_{A,2} &= (|H\rangle_A + e^{i\frac{5\pi}{2}}|V\rangle_A) \otimes (|s\rangle_A + e^{i\frac{5\pi}{4}}|l\rangle_A) \\
|l=3\rangle_{A,2} &= (|H\rangle_A + e^{i\frac{7\pi}{2}}|V\rangle_A) \otimes (|s\rangle_A + e^{i\frac{7\pi}{4}}|l\rangle_A) \\
\\
|k=0\rangle_{B,1} &= (|H\rangle_B + e^{-i\frac{\pi}{4}}|V\rangle_B) \otimes (|s\rangle_B + e^{-i\frac{\pi}{8}}|l\rangle_B) \\
|k=1\rangle_{B,1} &= (|H\rangle_B + e^{i\frac{11\pi}{4}}|V\rangle_B) \otimes (|s\rangle_B + e^{i\frac{11\pi}{8}}|l\rangle_B) \\
|k=2\rangle_{B,1} &= (|H\rangle_B + e^{i\frac{7\pi}{4}}|V\rangle_B) \otimes (|s\rangle_B + e^{i\frac{7\pi}{8}}|l\rangle_B) \\
|k=3\rangle_{B,1} &= (|H\rangle_B + e^{i\frac{3\pi}{4}}|V\rangle_B) \otimes (|s\rangle_B + e^{i\frac{3\pi}{8}}|l\rangle_B) \\
\\
|l=0\rangle_{B,2} &= (|H\rangle_B + e^{i\frac{\pi}{4}}|V\rangle_B) \otimes (|s\rangle_B + e^{i\frac{\pi}{8}}|l\rangle_B) \\
|l=1\rangle_{B,2} &= (|H\rangle_B + e^{i\frac{13\pi}{4}}|V\rangle_B) \otimes (|s\rangle_B + e^{i\frac{13\pi}{8}}|l\rangle_B) \\
|l=2\rangle_{B,2} &= (|H\rangle_B + e^{i\frac{9\pi}{4}}|V\rangle_B) \otimes (|s\rangle_B + e^{i\frac{9\pi}{8}}|l\rangle_B) \\
|l=3\rangle_{B,2} &= (|H\rangle_B + e^{i\frac{5\pi}{4}}|V\rangle_B) \otimes (|s\rangle_B + e^{i\frac{5\pi}{8}}|l\rangle_B)
\end{aligned} \tag{6.19}$$

Using same derivation technique that we recounted in Section 2.4, the above eigenvectors for the polarization degree of freedom can be translated to the settings for the angles of the  $\lambda/2$  and  $\lambda/4$  waveplates. For the energy-time degree of freedom, the phase can be directly set on the interferometers.

Alice and Bob each have 8 possible settings. Thus in total the whole  $I_{2244}$  requires 64 joint measurements. Results of these 64 joint measurements are then used in Eq. 6.12 to evaluate the inequality.

## 6.4 Results and Conclusions

Due to random drifts in the interferometers, there is a need to recalibrate them for every measurement. Although the calibration process has been automated, it still takes up to a minute to characterize and to set a specific phase for each interferometer. Thus to minimize the number of calibration cycles, we went with an integration time of 1 min, less than the characteristic time of the interferometer of 1.5 min, for each point in the measurement. Taking these factors into consideration, each complete  $I_{2244}$  inequality will take up to 2 hours to complete.

There are multiple issues with the generation and evaluation of the energy-time entangled state that renders long data runs nearly impossible. One of the possible issues is the frequency lock between the pump and calibration laser using the wavemeter. It turns out the 60 MHz resolution of the wavemeter still leaves significant play between the frequencies of the two lasers, resulting in a large variation of the energy-time entangled state generated. So far attempts at refining this lock with a dual wavelength transfer cavity has not been successfully implemented. Another possible reason lies in the inaccuracy in setting the required phases in the interferometers. This issue seems to be inherited from the difficulty in obtaining a good fit to the calibration data in order to obtain the required parameters for setting the phases. Any small artifact in the data will render the fitted parameters to be inaccurate.

Another issue is with the low signal rate. Due to the geometry of Michelson interferometer, half of the signal is lost when the retro-reflected light is sent the wrong way. This lowers the coincidence rate significantly making the accumulation of statistics difficult. So far with best data run, we have had 10 consecutive complete measurements of  $I_{2244}$ . From the measurement, we obtained a value of  $I_{2244} = 0.31 \pm 0.03$ . The error bound is too large to fall into the earlier evaluated range of  $0.304951 \leq I_{2244}^{\max}(\text{QM}) \leq 0.33609$ . Thus we cannot make a conclusive comment on the use of the CGLMP inequality  $I_{2244}$  as a dimension witness.

Unfortunately, shortly before wrapping up this thesis, we realized that because the maximally-entangled state with  $d = 4$  can be expressed as the product state of two maximally-

---

entangled states with  $d = 2$ , the inequality can still be violated purely by the classical feed-forward of an earlier measurement result onto the choice of settings for a later measurement. This makes our dimension witness susceptible to the same limitations as earlier experiments [27–29]. Whether this is a limitation of the specific form of the CGLMP inequality we were working with or indeed with any other dimensional witnesses, are still subjects of ongoing work.



# Chapter 7

## Conclusions

In this thesis, we presented the background theories, the implementation steps and the results obtained from three separate experiments, delving into various fundamental issues surrounding the Tsirelson's bound for quantum correlation, an algorithmic interpretation of quantum mechanics and the dimensionality of quantum systems.

In Chapter 3, we implemented an experiment to violate the CHSH inequality [70] using maximally polarization-entangled photon pairs from a SPDC source. With careful consideration of the experimental parameters and optimization of the settings, we obtained a violation of  $2.8276 \pm 0.00082$ , providing the smallest distance with respect to the Tsirelson's bound ever reported, namely,  $0.0008 \pm 0.00082$ . The Grinbaum's bound, which is slightly lower than the Tsirelson's bound, but is consistent with all previously available experimental results [5–17], was also violated by 2.72 standard deviations with this result, thus adding further support that there is no evidence in favor of the that quantum theory is only an effect version of a deeper theory for explaining the natural limits of correlations in all scenarios. Conversely, this strong violation strengthened the position of those principles that predict the Tsirelson's bound [18–20].

The large violation also has important implication for cryptographic security where approaching the Tsirelson' bound is a necessary and sufficient condition on certifying probability distributions in a device independent scenarios [103]. A similar situation applies for the certification of a variety of physical properties based solely on the assumption of non-signaling. In this respect, the degree of violation of the CHSH Bell inequality can be used to certify the amount of randomness [22]. As presented in Section 4.3.1, the binary output from either  $A$  or  $B$  is random in the ideal case. Thus, the higher the violation, the larger the amount of certified randomness. Distance from the Tsirelson's bound can also be used check whether the state being measured is a maximally entangled state and/or that the local measurements are of the type represented in quantum theory by anti-commuting

operators [23]. This can be adapted to practical methods to estimate the fidelity of the maximally-entangled states [24].

In Chapter 4, we highlighted the increasing alternative trend of viewing physical systems and processes as programs that run on a computer made of the constituents of our universe. In this interpretation, any process that can be simulated on a local universal Turing machine<sup>1</sup> can be encoded as a program that is fed into it. For every such a program there exists its shortest description called Kolmogorov complexity, which in most cases can only be approximated using compression software. As such a description must obey distance properties as shown in [26, 112], it allowed us to derive a brand new type of Bell type inequality that is independent of any statistical interpretation. With our experimental implementation of polarization measurements performed on photons pairs described by a maximally-entangled state and evaluation of approximations to Kolmogorov complexity using the compression software *LZMA* [115], we obtained the value of  $0.0494 \pm 0.0076$  for the inequality, which is 6.5 standard deviations from the classical limits.

This result thus suggests that there exist physical processes that cannot be simulated on local universal Turing machines. Furthermore, this algorithmic approach is complementary to the orthodox Bell inequality approach to quantum nonlocality [69] that is statistical in its nature and if extended to all quantum experiments, it would allow us to bypass the commonly used statistical interpretation of quantum theory. The result also beckons for a reformulation the traditional algorithmic complexity in terms of the quantum information science context, thus requiring further work on quantum version of Kolmogorov complexity [128]<sup>2</sup>.

In Chapter 6, we highlighted the importance of the dimensionality of the Hilbert space of a system as a quantum resource similar to entanglement in various quantum information processing tasks. Previous attempts at experimentally witnessing large Hilbert space dimension have the limitation of not being able to distinguish between classical and quantum dimension [27–29] or requiring a priori knowledge of the state under test to make a full assessment [30–33]. With that in mind, we motivated for the need for a device independent way of assessing the minimal dimension of Hilbert space.

Generalizing the work of Brunner [34], we formulated a dimension witness based on the CGLMP inequality [35] and experimentally implemented an energy-time and polarization hyperentangled state with a dimensionality  $d = 4$  for assessing it. However, due to

<sup>1</sup>This is analogous to the statement of non-separability of entangled states described in Section 1.1.3.

<sup>2</sup>Drawing a parallel between the algorithmic and statistical interpretation of quantum theory we have: A quantum Turing machine description would be equivalent to a non-separable entangled state while the quantum Kolmogorov complexity would then be equivalent to the joint probability of measurement outcomes in the statistical interpretation.

persistent stability issues in the generation of the hyperentangled state, we only manage to obtain the result of  $0.31 \pm 0.03$  at the time of writing of this thesis. This result does not violate the limit of 0.30 for  $d = 4$  with a small enough error bar and thus does not provide an conclusive assessment of the CGLMP inequality as a dimension witness. Unfortunately, shortly before the conclusion of this thesis, we realized that the inequality can be violated with entangled states of a lower dimensionality purely by the classical feed-forward of an earlier measurement result onto the choice of settings for a later measurement, making our dimensions witness susceptible to the same limitations mentioned earlier. Whether this is a limitation of the specific form of the CGLMP inequality we were working with or indeed with any other dimensional witnesses are subjects of ongoing work.



# References

- [1] N. Bohr. *Atomic Theory and the Description of Nature: Four Essays with an Introductory Survey*. Number v. 1. Cambridge University Press, 2011.
- [2] J.A. Wheeler and W.H. Zurek. *Quantum Theory and Measurement*. Princeton Legacy Library. Princeton University Press, 1983.
- [3] Alexei Grinbaum. Quantum theory as a critical regime of language dynamics. *Found Phys*, Jul 2015.
- [4] B. S. Cirel'son. Quantum generalizations of bell's inequality. *Letters in Mathematical Physics*, 4(2):93–100, March 1980.
- [5] Stuart J. Freedman and John F. Clauser. Experimental test of local hidden-variable theories. *Physical Review Letters*, 28(14):938–941, Apr 1972.
- [6] Alain Aspect, Philippe Grangier, and Gérard Roger. Experimental tests of realistic local theories via bell's theorem. *Physical Review Letters*, 47(7):460–463, August 1981.
- [7] Paul G. Kwiat, Klaus Mattle, Harald Weinfurter, Anton Zeilinger, Alexander V. Sergienko, and Yanhua Shih. New high-intensity source of polarization-entangled photon pairs. *Physical Review Letters*, 75(24):4337–4341, December 1995.
- [8] Gregor Weihs, Thomas Jennewein, Christoph Simon, Harald Weinfurter, and Anton Zeilinger. Violation of bell's inequality under strict Einstein locality conditions. *Physical Review Letters*, 81(23):5039–5043, Dec 1998.
- [9] W. Tittel, J. Brendel, H. Zbinden, and N. Gisin. Violation of bell inequalities by photons more than 10 km apart. *Physical Review Letters*, 81(17):3563–3566, Oct 1998.
- [10] M. A. Rowe, D. Kielpinski, V. Meyer, C. A. Sackett, W. M. Itano, C. Monroe, and D. J. Wineland. Experimental violation of a bell's inequality with efficient detection. *Nature*, 409(6822):791–794, Feb 2001.
- [11] D. L. Moehring, M. J. Madsen, B. B. Blinov, and C. Monroe. Experimental bell inequality violation with an atom and a photon. *Physical Review Letters*, 93(9), Aug 2004.
- [12] D. N. Matsukevich, P. Maunz, D. L. Moehring, S. Olmschenk, and C. Monroe. Bell inequality violation with two remote atomic qubits. *Physical Review Letters*, 100(15), Apr 2008.

- [13] Markus Ansmann, H. Wang, Radoslaw C. Bialczak, Max Hofheinz, Erik Lucero, M. Neeley, A. D. O’Connell, D. Sank, M. Weides, J. Wenner, and et al. Violation of bell’s inequality in Josephson phase qubits. *Nature*, 461(7263):504–506, Sep 2009.
- [14] J. Hofmann, M. Krug, N. Ortegel, L. Gerard, M. Weber, W. Rosenfeld, and H. Weinfurter. Heralded entanglement between widely separated atoms. *Science*, 337(6090):72–75, Jul 2012.
- [15] Wolfgang Pfaff, Tim H. Taminiau, Lucio Robledo, Hannes Bernien, Matthew Markham, Daniel J. Twitchen, and Ronald Hanson. Demonstration of entanglement-by-measurement of solid-state qubits. *Nat Phys*, 9(1):29–33, Oct 2012.
- [16] B. G. Christensen, K. T. McCusker, J. B. Altepeter, B. Calkins, T. Gerrits, A. E. Lita, A. Miller, L. K. Shalm, Y. Zhang, S. W. Nam, and et al. Detection-loophole-free test of quantum nonlocality, and applications. *Physical Review Letters*, 111(13), Sep 2013.
- [17] Mohamed Nawareg, Fabrizio Bisesto, Vincenzo D’Ambrosio, Elias Amselem, Fabio Sciarrino, Mohamed Bourennane, and Adan Cabello. Bounding quantum theory with the exclusivity principle in a two-city experiment. November 2013.
- [18] Marcin Pawłowski, Tomasz Paterek, Dagomir Kaszlikowski, Valerio Scarani, Andreas Winter, and Marek Zukowski. Information causality as a physical principle. *Nature*, 461(7267):1101–1104, Oct 2009.
- [19] Miguel Navascués and Harald Wunderlich. A glance beyond the quantum model. *Proceedings of the Royal Society of London A: Mathematical, Physical and Engineering Sciences*, 466(2115):881–890, 2010.
- [20] Adán Cabello. Simple explanation of the quantum limits of genuine  $n$ -body nonlocality. *Phys. Rev. Lett.*, 114:220402, Jun 2015.
- [21] T. Franz, F. Furrer, and R. F. Werner. Extremal quantum correlations and cryptographic security. *Physical Review Letters*, 106(25), Jun 2011.
- [22] S. Pironio, A. Acín, S. Massar, A. Boyer de la Giroday, D. N. Matsukevich, P. Maunz, S. Olmschenk, D. Hayes, L. Luo, T. A. Manning, and C. Monroe. Random numbers certified by Bell’s theorem. *Nature*, 464(7291):1021–1024, Apr 2010.
- [23] Dominic Mayers and Andrew Yao. Self testing quantum apparatus. *Quantum Info. Comput.*, 4(4):273–286, July 2004.
- [24] Jean-Daniel Bancal, Miguel Navascués, Valerio Scarani, Tamás Vértesi, and Tzyh Haur Yang. Physical characterization of quantum devices from nonlocal correlations. *Phys. Rev. A*, 91(2), Feb 2015.
- [25] Ben W. Reichardt, Falk Unger, and Umesh Vazirani. Classical command of quantum systems. *Nature*, 496(7446):456–460, Apr 2013.
- [26] M. Li, X. Chen, X. Li, B. Ma, and P.M.B. Vitanyi. The similarity metric. *IEEE Trans. Inform. Theory*, 50(12):3250–3264, December 2004.

- [27] Johan Ahrens, Piotr Badziąg, Adán Cabello, and Mohamed Bourennane. Experimental device-independent tests of classical and quantum dimensions. *Nat Phys*, 8(8):592–595, Jun 2012.
- [28] Martin Hendrych, Rodrigo Gallego, Michal Micuda, Nicolas Brunner, Antonio Acín, and Juan P. Torres. Experimental estimation of the dimension of classical and quantum systems. *Nat Phys*, 8(8):588–591, Jun 2012.
- [29] Johan Ahrens, Piotr Badziąg, Marcin Pawłowski, Marek Żukowski, and Mohamed Bourennane. Experimental tests of classical and quantum dimensionality. *Physical Review Letters*, 112(14), Apr 2014.
- [30] Adetunmise C. Dada, Jonathan Leach, Gerald S. Buller, Miles J. Padgett, and Erika Andersson. Experimental high-dimensional two-photon entanglement and violations of generalized bell inequalities. *Nat Phys*, 7(9):677–680, May 2011.
- [31] P. Ben Dixon, Gregory A. Howland, James Schneeloch, and John C. Howell. Quantum mutual information capacity for high-dimensional entangled states. *Physical Review Letters*, 108(14), Apr 2012.
- [32] R. Fickler, R. Lapkiewicz, W. N. Plick, M. Krenn, C. Schaeff, S. Ramelow, and A. Zeilinger. Quantum entanglement of high angular momenta. *Science*, 338(6107):640–643, November 2012.
- [33] M. Krenn, M. Huber, R. Fickler, R. Lapkiewicz, S. Ramelow, and A. Zeilinger. Generation and confirmation of a (100 x 100)-dimensional entangled quantum system. *Proceedings of the National Academy of Sciences*, 111(17):6243–6247, Mar 2014.
- [34] Nicolas Brunner, Stefano Pironio, Antonio Acin, Nicolas Gisin, André Allan Méthot, and Valerio Scarani. Testing the dimension of Hilbert spaces. *Physical Review Letters*, 100(21), May 2008.
- [35] Daniel Collins, Nicolas Gisin, Noah Linden, Serge Massar, and Sandu Popescu. Bell inequalities for arbitrarily high-dimensional systems. *Physical Review Letters*, 88(4), January 2002.
- [36] D. Bohm. *Quantum Theory*. Dover Books on Physics Series. Prentice-Hall, 1951.
- [37] Carl A. Kocher and Eugene D. Commins. Polarization correlation of photons emitted in an atomic cascade. *Physical Review Letters*, 18(15):575–577, April 1967.
- [38] David C. Burnham and Donald L. Weinberg. Observation of simultaneity in parametric production of optical photon pairs. *Physical Review Letters*, 25(2):84–87, July 1970.
- [39] J. D. Franson. Bell inequality for position and time. *Physical Review Letters*, 62(19):2205–2208, May 1989.
- [40] R. Thew, A. Acín, H. Zbinden, and N. Gisin. Experimental realization of entangled qutrits for quantum communication. *Quantum Info. Comput.*, 4(2):93–101, March 2004.

- [41] D. Richart. *Entanglement of Higher Dimensional Quantum States*. PhD thesis, Technische Universität München, 2008.
- [42] D. Richart, Y. Fischer, and H. Weinfurter. Experimental implementation of higher dimensional time-energy entanglement. *Applied Physics B*, 106(3):543–550, Jan 2012.
- [43] Charles H. Bennett, François Bessette, Gilles Brassard, Louis Salvail, and John Smolin. Experimental quantum cryptography. *Journal of Cryptology*, 5(1), 1992.
- [44] Dik Bouwmeester, Jian-Wei Pan, Klaus Mattle, Manfred Eibl, Harald Weinfurter, and Anton Zeilinger. Experimental quantum teleportation. *Nature*, 390(6660):575–579, Dec 1997.
- [45] Fabio Antonio Bovino, Pietro Varisco, Anna Maria Colla, Giuseppe Castagnoli, Giovanni Di Giuseppe, and Alexander V. Sergienko. Effective fiber-coupling of entangled photons for quantum communication. *Optics Communications*, 227(4-6):343–348, Nov 2003.
- [46] Cyril Branciard, Nicolas Brunner, Nicolas Gisin, Christian Kurtsiefer, Antia Lamas-Linares, Alexander Ling, and Valerio Scarani. Testing quantum correlations versus single-particle properties within leggett’s model and beyond. *Nat Phys*, 4(9):681–685, September 2008.
- [47] S. Gaertner, C. Kurtsiefer, M. Bourennane, and H. Weinfurter. Experimental demonstration of four-party quantum secret sharing. *Physical Review Letters*, 98(2), Jan 2007.
- [48] Jun Suzuki, Gelo Noel Macuja Tabia, and Berthold-Georg Englert. Symmetric construction of reference-frame-free qudits. *Phys. Rev. A*, 78(5), Nov 2008.
- [49] John C. Howell, Antia Lamas-Linares, and Dik Bouwmeester. Experimental violation of a spin-1 bell inequality using maximally entangled four-photon states. *Physical Review Letters*, 88(3), Jan 2002.
- [50] Mark D. de Burgh, Nathan K. Langford, Andrew C. Doherty, and Alexei Gilchrist. Choice of measurement sets in qubit tomography. *Phys. Rev. A*, 78(5), November 2008.
- [51] P.W. Shor. Algorithms for quantum computation: discrete logarithms and factoring. *Proceedings 35th Annual Symposium on Foundations of Computer Science*, 1994.
- [52] Lov K. Grover. A fast quantum mechanical algorithm for database search. *Proceedings of the twenty-eighth annual ACM symposium on Theory of computing - STOC '96*, 1996.
- [53] D.G. Angelakis. *Quantum Information Processing: From Theory to Experiment*. NATO science series. Series III, Computer and systems sciences. IOS Press, 2006.
- [54] Walther Gerlach and Otto Stern. Das magnetische moment des silberatoms. *Zeitschrift für Physik*, 9(1):353–355, Dec 1922.

- [55] Walther Gerlach and Otto Stern. Der experimentelle nachweis der richtungsquantelung im magnetfeld. *Zeitschrift für Physik*, 9(1):349–352, Dec 1922.
- [56] J. Q. You and Franco Nori. Superconducting circuits and quantum information. *Phys. Today*, 58(11):42–47, Nov 2005.
- [57] C. Monroe, D. M. Meekhof, B. E. King, W. M. Itano, and D. J. Wineland. Demonstration of a fundamental quantum logic gate. *Physical Review Letters*, 75(25):4714–4717, Dec 1995.
- [58] J. A. Jones and M. Mosca. Implementation of a quantum algorithm on a nuclear magnetic resonance quantum computer. *The Journal of Chemical Physics*, 109(5):1648, 1998.
- [59] F. W. Sun, Z. Y. Ou, and G. C. Guo. Projection measurement of the maximally entangled  $n$ -photon state for a demonstration of the  $n$ -photon de broglie wavelength. *Phys. Rev. A*, 73(2), Feb 2006.
- [60] J Brendel, E Mohler, and W Martienssen. Experimental test of bell’s inequality for energy and time. *Europhysics Letters (EPL)*, 20(7):575–580, December 1992.
- [61] I. Marcikic, H. de Riedmatten, W. Tittel, V. Scarani, H. Zbinden, and N. Gisin. Time-bin entangled qubits for quantum communication created by femtosecond pulses. *Phys. Rev. A*, 66(6), Dec 2002.
- [62] Paul G. Kwiat, Edo Waks, Andrew G. White, Ian Appelbaum, and Philippe H. Eberhard. Ultrabright source of polarization-entangled photons. *Phys. Rev. A*, 60(2):R773–R776, August 1999.
- [63] Christian Kurtsiefer, Markus Oberparleiter, and Harald Weinfurter. High-efficiency entangled photon pair collection in type-ii parametric fluorescence. *Phys. Rev. A*, 64(2), July 2001.
- [64] D. Dieks. Communication by EPR devices. *Physics Letters A*, 92(6):271–272, Nov 1982.
- [65] William K. Wootters and Wojciech H. Zurek. The no-cloning theorem. *Phys. Today*, 62(2):76–77, Feb 2009.
- [66] Dagmar Bruß, David P. DiVincenzo, Artur Ekert, Christopher A. Fuchs, Chiara Macchiavello, and John A. Smolin. Optimal universal and state-dependent quantum cloning. *Phys. Rev. A*, 57(4):2368–2378, Apr 1998.
- [67] Michael A. Nielsen and Isaac L. Chuang. *Quantum Computation and Quantum Information*. Cambridge University Press, New York, NY, USA, 2000.
- [68] A. Einstein, B. Podolsky, and N. Rosen. Can quantum-mechanical description of physical reality be considered complete? *Phys. Rev.*, 47(10):777–780, May 1935.
- [69] J. S. Bell. On the Einstein-podolsky-rosen paradox. *Physics I*, 1(3):195–200, 1964.

- [70] John F. Clauser, Michael A. Horne, Abner Shimony, and Richard A. Holt. Proposed experiment to test local hidden-variable theories. *Physical Review Letters*, 23(15):880–884, October 1969.
- [71] Jing-Ling Chen, Chunfeng Wu, L. C. Kwak, and C. H. Oh. Bell inequalities for three particles. *Phys. Rev. A*, 78(3), Sep 2008.
- [72] Alain Aspect, Philippe Grangier, and Gérard Roger. Experimental realization of Einstein-podolsky-rosen-bohm *Gedankenexperiment*: A new violation of bell's inequalities. *Physical Review Letters*, 49(2):91–94, July 1982.
- [73] Alain Aspect, Jean Dalibard, and Gérard Roger. Experimental test of bell's inequalities using time-varying analyzers. *Phys. Rev. Lett.*, 49:1804–1807, December 1982.
- [74] P.V. Coveney and R. Highfield. *Frontiers of Complexity: The Search for Order in a Chaotic World*. A Fawcett Columbine book. Fawcett Columbine, 1996.
- [75] Stephen Wolfram. Undecidability and intractability in theoretical physics. *Physical Review Letters*, 54(8):735–738, February 1985.
- [76] Julio T. Barreiro, Nathan K. Langford, Nicholas A. Peters, and Paul G. Kwiat. Generation of hyperentangled photon pairs. *Physical Review Letters*, 95(26), Dec 2005.
- [77] Stephen P. Walborn. Hyperentanglement: Breaking the communication barrier. *Nat Phys*, 4(4):268–269, Apr 2008.
- [78] Wei-Bo Gao, Chao-Yang Lu, Xing-Can Yao, Ping Xu, Otfried Gühne, Alexander Goebel, Yu-Ao Chen, Cheng-Zhi Peng, Zeng-Bing Chen, and Jian-Wei Pan. Experimental demonstration of a hyper-entangled ten-qubit schrödinger cat state. *Nat Phys*, 6(5):331–335, March 2010.
- [79] J. S. Bell and Alain Aspect. *Speakable and Unspeakable in Quantum Mechanics*. Cambridge University Press, 2004.
- [80] Alois Mair, Alipasha Vaziri, Gregor Weihs, and Anton Zeilinger. Entanglement of the orbital angular momentum states of photons. *Nature*, 412(6844):313–316, July 2001.
- [81] Thomas Jennewein, Christoph Simon, Gregor Weihs, Harald Weinfurter, and Anton Zeilinger. Quantum cryptography with entangled photons. *Physical Review Letters*, 84(20):4729–4732, May 2000.
- [82] Simon Groblacher, Tomasz Paterek, Rainer Kaltenbaek, Caslav Brukner, Marek Zukowski, Markus Aspelmeyer, and Anton Zeilinger. An experimental test of non-local realism. *Nature*, 446(7138):871–875, April 2007.
- [83] S. Cova, M. Ghioni, A. Lacaita, C. Samori, and F. Zappa. Avalanche photodiodes and quenching circuits for single-photon detection. *Appl. Opt.*, 35(12):1956, 1996.
- [84] S O Flyckt and Carole Marmonier. *Photomultiplier tubes: principles and applications; 2nd ed.* Photonis, Brive, 2002.

- [85] M. Fox. *Quantum Optics : An Introduction: An Introduction*. Oxford Master Series in Physics. OUP Oxford, 2006.
- [86] B.E.A. Saleh and M.C. Teich. *Fundamentals of Photonics*. Wiley Series in Pure and Applied Optics. Wiley, 2007.
- [87] D.N. Klyshko. *Photons Nonlinear Optics*. Taylor & Francis, 1988.
- [88] C. K. Hong and L. Mandel. Theory of parametric frequency down conversion of light. *Phys. Rev. A*, 31(4):2409–2418, April 1985.
- [89] Robert W. Boyd. *Nonlinear Optics, Third Edition*. Academic Press, 3rd edition, 2008.
- [90] Hou Shun Poh, Chune Yang Lum, Ivan Marcikic, Antía Lamas-Linares, and Christian Kurtsiefer. Joint spectrum mapping of polarization entanglement in spontaneous parametric down-conversion. *Phys. Rev. A*, 75(4), April 2007.
- [91] Shigeki Takeuchi. Beamlike twin-photon generation by use of type ii parametric downconversion. *Opt. Lett.*, 26(11):843–845, Jun 2001.
- [92] A. V. Burlakov, M. V. Chekhova, O. A. Karabutova, and S. P. Kulik. Collinear two-photon state with spectral properties of type-i and polarization properties of type-ii spontaneous parametric down-conversion: Preparation and testing. *Phys. Rev. A*, 64:041803, Sep 2001.
- [93] Christian Kurtsiefer, Markus Oberparleiter, and Harald Weinfurter. Generation of correlated photon pairs in type-ii parametric down conversion – revisited. *Journal of Modern Optics*, 48(13):1997–2007, November 2001.
- [94] M. Barbieri, F. De Martini, G. Di Nepi, P. Mataloni, G. M. D’Ariano, and C. Macchiavello. Detection of entanglement with polarized photons: Experimental realization of an entanglement witness. *Physical Review Letters*, 91(22), Nov 2003.
- [95] Otfried Gühne and Géza Tóth. Entanglement detection. *Physics Reports*, 474(1-6):1–75, Apr 2009.
- [96] Daniel F. V. James, Paul G. Kwiat, William J. Munro, and Andrew G. White. Measurement of qubits. *Phys. Rev. A*, 64(5), October 2001.
- [97] Jaroslav Řeháček, Berthold-Georg Englert, and Dagomir Kaszlikowski. Minimal qubit tomography. *Phys. Rev. A*, 70(5), November 2004.
- [98] Sandu Popescu and Daniel Rohrlich. Quantum nonlocality as an axiom. *Foundations of Physics*, 24(3):379–385, Mar 1994.
- [99] Wim van Dam. Implausible consequences of superstrong nonlocality. *Natural Computing*, 12(1):9–12, Nov 2012.
- [100] Gilles Brassard, Harry Buhrman, Noah Linden, André Allan Mthot, Alain Tapp, and Falk Unger. Limit on nonlocality in any world in which communication complexity is not trivial. *Physical Review Letters*, 96(25), Jun 2006.

- [101] F.J. MacWilliams and N.J.A. Sloane. *The Theory of Error Correcting Codes*. Number pts. 1-2 in North-Holland mathematical library. North-Holland Publishing Company, 1977.
- [102] Sheer El-Showk, Miguel F. Paulos, David Poland, Slava Rychkov, David Simmons-Duffin, and Alessandro Vichi. Solving the 3d ising model with the conformal bootstrap ii. *c*-minimization and precise critical exponents. *J Stat Phys*, 157(4-5):869–914, Jun 2014.
- [103] Antonio Acín, Nicolas Brunner, Nicolas Gisin, Serge Massar, Stefano Pironio, and Valerio Scarani. Device-independent security of quantum cryptography against collective attacks. *Physical Review Letters*, 98(23), Jun 2007.
- [104] Sandu Popescu and Daniel Rohrlich. Which states violate Bell’s inequality maximally? *Physics Letters A*, 169(6):411–414, Oct 1992.
- [105] Wojciech Wasilewski, Czesław Radzewicz, Robert Frankowski, and Konrad Banaszek. Statistics of multiphoton events in spontaneous parametric down-conversion. *Phys. Rev. A*, 78(3), Sep 2008.
- [106] Ilja Gerhardt, Qin Liu, Antáa Lamas-Linares, Johannes Skaar, Valerio Scarani, Vadim Makarov, and Christian Kurtsiefer. Experimentally faking the violation of bell’s inequalities. *Physical Review Letters*, 107(17), Oct 2011.
- [107] Cristopher Moore. Unpredictability and undecidability in dynamical systems. *Physical Review Letters*, 64(20):2354–2357, May 1990.
- [108] Richard P. Feynman. Simulating physics with computers. *Int J Theor Phys*, 21(6-7):467–488, June 1982.
- [109] S. Wolfram. *A new kind of science*. General science. Wolfram Media, 2002.
- [110] D. Deutsch. Quantum theory, the church-turing principle and the universal quantum computer. *Proceedings of the Royal Society A: Mathematical, Physical and Engineering Sciences*, 400(1818):97–117, Jul 1985.
- [111] S. Lloyd. Universal quantum simulators. *Science*, 273(5278):1073–1078, Aug 1996.
- [112] R. Cilibrasi and P.M.B. Vitanyi. Clustering by compression. *IEEE Trans. Inform. Theory*, 51(4):1523–1545, April 2005.
- [113] M Li and P M B Vitanyi. *An Introduction to Kolmogorov Complexity and Its Applications*. Texts in Computer Science. Springer New York, 2009.
- [114] T M Cover and J A Thomas. *Elements of Information Theory*. Wiley-Interscience, 2nd edition, 2006.
- [115] Igor Pavlov. <http://www.7-zip.org/sdk.html>.
- [116] L. E. BALLENTINE. The statistical interpretation of quantum mechanics. *Rev. Mod. Phys.*, 42(4):358–381, Oct 1970.

- [117] Samuel L. Braunstein and Carlton M. Caves. Information-theoretic bell inequalities. *Physical Review Letters*, 61(6):662–665, Aug 1988.
- [118] C. E. Shannon. A mathematical theory of communication. *Bell System Technical Journal*, 27(3):379–423, July 1948.
- [119] Julian Seward. <http://www.bzip.org/>.
- [120] Jean-loup Gailly and Mark Adler. <http://www.gzip.org/>.
- [121] Welch. A technique for high-performance data compression. *Computer*, 17(6):8–19, Jun 1984.
- [122] MATLAB R2010a, The MathWorks, Inc., Natick, Massachusetts, United States.
- [123] Makoto Matsumoto and Takuji Nishimura. Mersenne twister: a 623-dimensionally equidistributed uniform pseudo-random number generator. *TOMACS*, 8(1):3–30, Jan 1998.
- [124] George Marsaglia and Wai Wan Tsang. The ziggurat method for generating random variables. *Journal of Statistical Software*, 5(8):1–7, 10 2000.
- [125] Bruno Sanguinetti, Anthony Martin, Hugo Zbinden, and Nicolas Gisin. Quantum random number generation on a mobile phone. *Physical Review X*, 4(3), Sep 2014.
- [126] Euk Jin Alexander Ling. *Entangled State Preparation For Optical Quantum Communication: Creating and characterizing photon pairs from Spontaneous Parametric Down Conversion inside bulk uniaxial crystals*. PhD thesis, National University of Singapore, 2008.
- [127] C.H. Papadimitriou. *Computational Complexity*. Theoretical computer science. Addison-Wesley, 1994.
- [128] Markus Mueller. Quantum kolmogorov complexity and the quantum turing machine. December 2007.
- [129] Ivan Marcikic, Antía Lamas-Linares, and Christian Kurtsiefer. Free-space quantum key distribution with entangled photons. *Appl. Phys. Lett.*, 89(10):101122, 2006.
- [130] R. Ursin, F. Tiefenbacher, T. Schmitt-Manderbach, H. Weier, T. Scheidl, M. Lindenthal, B. Blauensteiner, T. Jennewein, J. Perdigues, P. Trojek, and et al. Entanglement-based quantum communication over 144 km. *Nat Phys*, 3(7):481–486, Jun 2007.
- [131] Juan Yin, Yuan Cao, Shu-Bin Liu, Ge-Sheng Pan, Jin-Hong Wang, Tao Yang, Zhong-Ping Zhang, Fu-Min Yang, Yu-Ao Chen, Cheng-Zhi Peng, and et al. Experimental quasi-single-photon transmission from satellite to earth. *Optics Express*, 21(17):20032, 2013.
- [132] Giuseppe Vallone, Davide Bacco, Daniele Dequal, Simone Gaiarin, Vincenza Luceri, Giuseppe Bianco, and Paolo Villoresi. Experimental satellite quantum communications. June 2014.

- [133] Scott Bloom, Eric Korevaar, John Schuster, and Heinz Willebrand. Understanding the performance of free-space optics [invited]. *J. Opt. Netw.*, 2(6):178–200, Jun 2003.
- [134] C. Gobby, Z. L. Yuan, and A. J. Shields. Quantum key distribution over 122 km of standard telecom fiber. *Appl. Phys. Lett.*, 84(19):3762, 2004.
- [135] D Stucki, N Walenta, F Vannel, R T Thew, N Gisin, H Zbinden, S Gray, C R Towery, and S Ten. High rate, long-distance quantum key distribution over 250 km of ultra low loss fibres. *New Journal of Physics*, 11(7):075003, Jul 2009.
- [136] D. Lancho, J. Martinez, D. Elkouss, M. Soto, and V. Martin. Qkd in standard optical telecommunications networks. *Quantum Communication and Quantum Networking*, pages 142–149, 2010.
- [137] R. Ulrich, S. C. Rashleigh, and W. Eickhoff. Bending-induced birefringence in single-mode fibers. *Optics Letters*, 5(6):273, 1980.
- [138] E. Collett. *Polarized Light in Fiber Optics*. Press Monographs Series. PolaWave Group, 2003.
- [139] Ludwig Zehnder. Ein neuer interferenzrefraktor. *Zeitschrift für Instrumentenkunde*, 11:275–285, 1891.
- [140] Ludwig Mach. Ueber einen interferenzrefraktor. *Zeitschrift für Instrumentenkunde*, 12:89–93, 1892.
- [141] W. Heisenberg. Über den anschaulichen inhalt der quantentheoretischen kinematik und mechanik. *Zeitschrift für Physik*, 43(3-4):172–198, Mar 1927.
- [142] Z. Y. Ou, X. Y. Zou, L. J. Wang, and L. Mandel. Observation of nonlocal interference in separated photon channels. *Physical Review Letters*, 65(3):321–324, July 1990.
- [143] J Wabnig, D Bitauld, H W Li, A Laing, J L O’Brien, and A O Niskanen. Demonstration of free-space reference frame independent quantum key distribution. *New Journal of Physics*, 15(7):073001, Jul 2013.
- [144] Catherine Lee, Zheshen Zhang, Jacob C. Mower, Greg Steinbrecher, Hongchao Zhou, Ligong Wang, Robert Horansky, Varun B. Verma, Michael Allman, Adriana Lita, and et al. High-dimensional time-energy entanglement-based quantum key distribution using dispersive optics. *CLEO: 2014*, 2014.
- [145] Mohammad Mirhosseini, Omar S Magaña Loaiza, Malcolm N O’Sullivan, Brandon Rodenburg, Mehul Malik, Martin P J Lavery, Miles J Padgett, Daniel J Gauthier, and Robert W Boyd. High-dimensional quantum cryptography with twisted light. *New Journal of Physics*, 17(3):033033, Mar 2015.
- [146] Chao-Yang Lu, Xiao-Qi Zhou, Otfried Gühne, Wei-Bo Gao, Jin Zhang, Zhen-Sheng Yuan, Alexander Goebel, Tao Yang, and Jian-Wei Pan. Experimental entanglement of six photons in graph states. *Nat Phys*, 3(2):91–95, Jan 2007.
- [147] T. M. Graham, J. T. Barreiro, M. Mohseni, and P. G. Kwiat. Hyperentanglement-enabled direct characterization of quantum dynamics. *Physical Review Letters*, 110(6), Feb 2013.

- [148] P Grangier, G Roger, and A Aspect. Experimental evidence for a photon anticorrelation effect on a beam splitter: A new light on single-photon interferences. *Europhysics Letters (EPL)*, 1(4):173–179, Feb 1986.
- [149] J. Brendel, N. Gisin, W. Tittel, and H. Zbinden. Pulsed energy-time entangled twin-photon source for quantum communication. *Physical Review Letters*, 82(12):2594–2597, Mar 1999.
- [150] Hou Shun Poh, Jiaqing Lim, Ivan Marcikic, Antía Lamas-Linares, and Christian Kurtsiefer. Eliminating spectral distinguishability in ultrafast spontaneous parametric down-conversion. *Phys. Rev. A*, 80(4), Oct 2009.
- [151] Hou Shun Poh. Towards a high quality polarization-entangled multi-photon source. Master’s thesis, National University of Singapore, 2009.
- [152] Evan Jeffrey, Nicholas A Peters, and Paul G Kwiat. Towards a periodic deterministic source of arbitrary single-photon states. *New Journal of Physics*, 6:100–100, Jan 2004.
- [153] Hugues de Riedmatten, Valerio Scarani, Ivan Marcikic, Antonio Acín, Wolfgang Tittel, Hugo Zbinden, and Nicolas Gisin. Two independent photon pairs versus four-photon entangled states in parametric down conversion. *Journal of Modern Optics*, 51(11):1637–1649, Jul 2004.
- [154] Özgün Süzer and Theodore G. Goodson. Does pump beam intensity affect the efficiency of spontaneous parametric down conversion? *Optics Express*, 16(25):20166, 2008.
- [155] Harald Weinfurter and Marek Żukowski. Four-photon entanglement from down-conversion. *Phys. Rev. A*, 64(1), Jun 2001.
- [156] Manfred Eibl, Sascha Gaertner, Mohamed Bourennane, Christian Kurtsiefer, Marek Żukowski, and Harald Weinfurter. Experimental observation of four-photon entanglement from parametric down-conversion. *Physical Review Letters*, 90(20), May 2003.
- [157] A. Lamas-Linares, J. C. Howell, and D. Bouwmeester. Stimulated emission of polarization-entangled photons. *Nature*, 412(6850):887–890, Aug 2001.
- [158] Hugues de Riedmatten, Ivan Marcikic, Valerio Scarani, Wolfgang Tittel, Hugo Zbinden, and Nicolas Gisin. Tailoring photonic entanglement in high-dimensional Hilbert spaces. *Phys. Rev. A*, 69(5), May 2004.
- [159] Julio T. Barreiro, Tzu-Chieh Wei, and Paul G. Kwiat. Beating the channel capacity limit for linear photonic superdense coding. *Nat Phys*, 4(4):282–286, Mar 2008.
- [160] Paul G. Kwiat and Harald Weinfurter. Embedded bell-state analysis. *Phys. Rev. A*, 58(4):R2623–R2626, Oct 1998.
- [161] Carsten Schuck, Gerhard Huber, Christian Kurtsiefer, and Harald Weinfurter. Complete deterministic linear optics bell state analysis. *Physical Review Letters*, 96(19), May 2006.

- [162] Tzu-Chieh Wei, Julio T. Barreiro, and Paul G. Kwiat. Hyperentangled bell-state analysis. *Phys. Rev. A*, 75(6), Jun 2007.
- [163] M. Barbieri, G. Vallone, P. Mataloni, and F. De Martini. Complete and deterministic discrimination of polarization bell states assisted by momentum entanglement. *Phys. Rev. A*, 75(4), Apr 2007.
- [164] Benjamin P. Lanyon, Marco Barbieri, Marcelo P. Almeida, Thomas Jennewein, Timothy C. Ralph, Kevin J. Resch, Geoff J. Pryde, Jeremy L. O’Brien, Alexei Gilchrist, and Andrew G. White. Simplifying quantum logic using higher-dimensional Hilbert spaces. *Nat Phys*, 5(2):134–140, December 2008.
- [165] Charles H. Bennett, David P. DiVincenzo, Peter W. Shor, John A. Smolin, Barbara M. Terhal, and William K. Wootters. Remote state preparation. *Physical Review Letters*, 87(7), Jul 2001.
- [166] Marco Barbieri, Francesco De Martini, Paolo Mataloni, Giuseppe Vallone, and Adán Cabello. Enhancing the violation of the Einstein-podolsky-rosen local realism by quantum hyperentanglement. *Physical Review Letters*, 97(14), Oct 2006.
- [167] Alipasha Vaziri, Gregor Weihs, and Anton Zeilinger. Experimental two-photon, three-dimensional entanglement for quantum communication. *Physical Review Letters*, 89(24), Nov 2002.
- [168] A. Acín, T. Durt, N. Gisin, and J. I. Latorre. Quantum nonlocality in two three-level systems. *Phys. Rev. A*, 65(5), May 2002.
- [169] Li-Bin Fu, Jing-Ling Chen, and Xian-Geng Zhao. Maximal violation of the Clauser-horne-shimony-holt inequality for two qutrits. *Phys. Rev. A*, 68(2), Aug 2003.
- [170] Li-Bin Fu, Jing-Ling Chen, and Shi-Gang Chen. Maximal violation of Clauser-horne-shimony-holt inequality for four-level systems. *Phys. Rev. A*, 69(3), Mar 2004.
- [171] Li Masanes. Tight bell inequality for d-outcome measurements correlations. *Quantum Info. Comput.*, 3(4):345–358, July 2003.
- [172] Daniel Collins and Nicolas Gisin. A relevant two qubit bell inequality inequivalent to the chsh inequality. *J. Phys. A: Math. Gen.*, 37(5):1775–1787, Jan 2004.
- [173] Yeong-Cherng Liang. *Correlations, Bell Inequality Violation & Quantum Entanglement*. PhD thesis, University of Queensland, 2008.
- [174] John F. Clauser and Michael A. Horne. Experimental consequences of objective local theories. *Phys. Rev. D*, 10(2):526–535, Jul 1974.
- [175] Miguel Navascués, Stefano Pironio, and Antonio Acín. Bounding the set of quantum correlations. *Physical Review Letters*, 98(1), Jan 2007.
- [176] Jean-Daniel Bancal, Cai Yu, and Valerio Scarani. 11th intl. conference on quantum communication, measurement and computing. In *CGLMP4 Inequality as a Dimension Witness*, pages P1–47, Vienna, 2012.

- 
- [177] ADDETUNMISE C. DADA and ERIKA ANDERSSON. On bell inequality violations with high-dimensional systems. *International Journal of Quantum Information*, 09(07n08):1807–1823, Oct 2011.
- [178] Nicolas Brunner Lluís Masanes Sergi Pino Valerio Scarani, Nicolas Gisin and Antonio Acín. Secrecy extraction from no-signaling correlations. 74:042339, 2006.
- [179] Stefano Pironio Tamás Vértesi and Nicolas Brunner. Closing the detection loophole in bell experiments using qudits. 104:060401, 2010.
- [180] D. Kaszlikowski T. Durt and M. Żukowski. Violations of local realism with quantum systems described by n-dimensional hilbert spaces up to n=16. 64:024101, 2001.

